R-1069
CU-321
NEVIS-215
FERMILAB-THESIS-1976-18

Nevis Laboratories
Columbia University
Physics Department
Irvington-on-Hudson
New York

Hadrons and Leptons at High Transverse Momentum

IRWIN GAINES

Submitted in partial fulfillment of
the requirements for the degree
of Doctor of Philosophy in the Faculty
of Pure Science, Columbia University

1976

National Science Foundation
GP 06955

Hadrons and Leptons at High Transverse Momentum *

IRWIN GAINES †

Columbia University, New York, N.Y.

---

* Research supported in part by the National Science Foundation.

† Submitted in partial fulfillment of the requirements for the degree of Doctor of Philosophy in the Faculty of Pure Science, Columbia University.

ABSTRACT

A Columbia-Fermilab collaboration has studied the production of hadrons and leptons at high transverse momenta produced in 300 GeV proton nuclear collisions at the Fermi National Accelerator Laboratory, with apparatus consisting of a magnetic spectrometer, a lead glass calorimeter for electromagnetic showers, and a crude hadron calorimeter. Measurements were taken between 1.6 and 5.0 GeV of transverse momentum, and at angles of 65^{o} and 93^{o} in the center of mass system. Neutral hadrons were measured by observing the spectrum of electrons produced by gamma ray conversions in thin foils, while charged hadrons were observed directly. Results are presented here for both neutral and charged hadrons at both angles, and for the target nucleus dependence of the cross section at large transverse momentum. Details of electron identification and measurement, which allow detection of the conversion electrons spectrum, as well as the observation of a directly produced electron signal, are also given.

TABLE OF CONTENTS

	Page
I. Introduction	1
II. Apparatus	
A. Overview	6
B. Beam	8
C. Target	9
D. Collimator	11
E. Magnets	12
F. Trigger Counters and Hodoscopes	14
G. Lead Glass	16
H. Hadron and Muon Detectors	20
I. Electronics	21
J. On-Line Computer	26
III. Data Taking	
A. Triggering	27
B. On-Line Program	32
C. Running Procedure	34
IV. Analysis	
A. Event-by-Event Analysis	38
B. Run-by-Run Analysis	49
C. Absolute Normalization	57
V. Results	
A. Leptons	61
B. Hadrons	63
VI. Theory and Conclusions	69
Acknowledgments	77
Tables	79
References	97
Appendix	104
Figure Captions	110
Figures	111

I. INTRODUCTION

Each time that a new generation of particle accelerators has opened, allowing high energy physicists access to a new energy regime, a new range of phenomena has also been opened up for investigation. Thus, the openings of the Intersecting Storage Rings at CERN and the Fermi National Accelerator Laboratory in Batavia, Illinois carry with them the obligation to perform experiments that will not only extend knowledge of the more or less familiar effects studied at lower energies, but also be sensitive to new and perhaps unexpected manifestations of the fundamental interactions. In addition, new experimental techniques must be developed to cope with the new problems caused by higher energies.

One such experiment is the investigation of particle production at large transverse momenta in proton-proton collisions. Most simply, this experiment relies on the concept that large angle scatters carry information about the very short distance behavior of the interactions under study, and thus hopefully about the basic structure of the colliding particles.

Indeed, earlier experiments[1] reveal a striking dearth of particles at high $p_\perp$. The strong interactions seem to be characterized by a steep exponential fall-off in particle production with increasing transverse momentum. Thus, while total cross sections and low $p_\perp$ collisions will continue

to be dominated by the strong interactions, with increasing $p_\perp$, the cross sections will begin to be dominated by weak and electromagnetic processes,[2] which are not expected to undergo as steep a fall-off with $p_\perp$. In this way it becomes possible to study weak and electromagnetic interactions in proton-proton collisions, utilizing the primary beam at the new accelerators and taking full advantage of the maximum energies and intensities that can be reached.

Hadron production at large transverse momenta can test a wide variety of theoretical models.[2-6] In particular, such experiments may determine whether the basic process involved is one of fireball production, where the large $p_\perp$ final states are produced by the decay of a virtual high mass intermediate state, or of hard scattering, where the interactions of constituents of the proton are important. Alternatively, the observations at high $p_\perp$ may indicate the production of a relatively small number of new particles, the production mechanism differing qualitatively from typical strong processes.[7]

Looking at lepton production at high $p_\perp$ can tell us even more. First of all, there is an expected continuum of high mass lepton pairs due to virtual photon production (Fig. 1a):

$$p + p \rightarrow \text{"}\gamma\text{"} + \text{anything} \qquad (1)$$
$$\hookrightarrow e^+e^- \quad .$$

This process is obviously closely related to deeply inelastic electron scattering[8] (Fig. 1b):

$$e^- + p \rightarrow e^- + \text{anything} \qquad (2)$$

except that the virtual photon in the scattering experiment is spacelike rather than timelike. Parton type models, postulating pointlike constituents inside the proton, were very successful in fitting the SLAC data on reaction (2),[9] and these models also give predictions for reaction (1).[10] Measurements of lepton production at high $p_\perp$ would be an important test of these parton models.

Of course, reaction (1) is also closely related to electron positron annihilation (Fig. 1c):

$$e^+ + e^- \rightarrow \text{anything} \qquad (3)$$

where the virtual photon is again timelike. The data on reaction (3), measured at CEA and at SPEAR,[11] are another severe test of parton models. A model must successfully deal with all three reactions before it can be taken seriously, and each of the three experiments can put important constraints on the theory.

Furthermore, the single lepton spectrum at high $p_\perp$ is sensitive to the presence of heavy particles which have two or three body decays into leptons. Any heavy particle of mass M, produced with the typical hadronic steeply falling spectrum in $p_\perp$ and $p_{||}$, and with a two body decay into leptons, will give a sharp peak at $p_\perp = M/2$ in the lepton spectrum. (Such a natural peaking could be diminished if the massive particles are produced preferentially at large $p_\perp$. Such a pathological production process has never been observed.)

Three body decays will give similar although less sharp peaks.

For example, consider production of a W boson,[12] the hypothetical mediator of the weak interaction (Fig. 1d):

$$p + p \rightarrow W^{\pm} + \text{anything}$$
$$\hookrightarrow e^{\pm}\nu \quad .$$

Figure 2 shows the transverse momentum spectrum of electrons produced in this process for a 15 GeV W, assuming a branching ratio of 1/4 for

$$R = \frac{W \rightarrow e\nu}{W \rightarrow \text{all}}$$

compared with the continuum of electrons from virtual photon production. A clear peak at 7.5 GeV is visible. Similarly, a peak would be produced by Z^o, the mediator of the neutral weak current; B^o, the Lee-Wick heavy photon;[13] heavy leptons, charmed particles, or particles with other new quantum numbers. (The presence of some of these particles could also be indicated by an asymmetry between positive and negative leptons, or between electrons and muons.) Looking at high $p_\perp$ leptons will be sensitive to these particles if their masses are within the kinematic limit for production at FNAL (22 GeV when the accelerator runs at 300 GeV).

Earlier high $p_\perp$ experiments include a search for single muons at BNL[14] (this was designed as a W search, and so only measured upper limits on muon production), and a dimuon experiment at BNL[15] which observed a continuum of muon pairs out to dimuon masses of 6 GeV.

More recently, several experiments at the ISR[16] have observed high $p_\perp$ charged and neutral hadrons, at a level many orders of magnitude higher than would be expected from a continuation of the steep exponential seen at lower $p_\perp$, thus giving great impetus to the field of high transverse momentum physics. In addition, there was a search for high $p_\perp$ leptons and lepton pairs[17] which failed to see a signal.

I will report here on a Columbia University-Fermilab collaboration[18] which measured single leptons and hadrons produced at high $p_\perp$.[19] We observed both electrons and muons, and both charged and neutral hadrons. The measurements presented here were taken at the Fermilab with a 300 GeV incident beam, and at laboratory angles of 50 and 83 milliradians (mrad), corresponding to about 65^o and 93^o in the center of mass system. Further measurements have been taken at 200 and 400 GeV, and at 67 and 100 mrad, and will be published soon. In addition, a continuation of the present collaboration will begin measuring lepton and hadron pairs in early 1975.

II. APPARATUS

A. Overview

The spectrum of high transverse momentum hadrons is measured in two ways. Charged hadrons are observed directly, with the energy and production angle of the hadron measured by our spectrometer. Neutral hadrons (specifically π^o's) are observed only indirectly, by measuring the spectrum of electrons produced by conversions of gamma rays in thin foils. Careful measurement of these conversion electrons allows one to deduce the π^o spectrum. Thus, the bulk of the experimental effort, to measure both hadrons and directly produced leptons, is directed towards identification and measurement of electrons.

The experimental apparatus was designed with several specific goals in mind. First, the experiment must be able to run at high intensities, since we are trying to measure a very small cross section. Next, it should have a wide acceptance, allowing measurement of a broad range of transverse momentum simultaneously and avoiding relative normalization problems. Next, it must have very good energy resolution so as to be sensitive to peaks in the $p_\perp$ spectra. And finally, it must have excellent hadron rejection, both in the trigger and in off-line analysis, so that a trickle of leptons can be extracted from a vast flood of hadrons.

One basic idea of the experiment is that the production angle is measured in the horizontal plane, while momentum is

measured by magnetic analysis in the vertical plane. This can be seen in the schematic diagram of the apparatus (Fig. 3). The top view shows our detectors sitting at a wide angle with respect to the incoming proton beam. The side view shows the vertical bend in our analyzing magnet, which results in neutral and wrong sign particles passing under our apparatus, and low energy particles of the right sign passing above.

Moreover, in order to run at high intensity, we make no measurement at all before the magnet. Thus, the flux of particles we are concerned with consists only of charged particles, of one sign, in a momentum band determined by the magnet current. With this technique, we are able to measure processes which represent less than 1 part in 10^{11} of the total cross section without being swamped by background. (The success of this method of course depends on a very small rate of particles coming from sources other than the target, as is shown below.) In addition, our single bend non-focusing spectrometer has a wide enough aperture so as to accept a wide range of transverse momenta simultaneously.

For electrons, a more precise energy measurement is made in our array of lead glass, described fully in Sec. II.G. Comparison of the energy measured by the lead glass and by the magnetic spectrometer provides an important criterion for rejecting hadrons. The distribution of an electromagnetic shower in the lead glass provides further rejection, and the lead glass also provides us with vital triggering information.

B. Beam

The beam for our experiment is the slow extracted primary proton beam at the Fermi National Accelerator Laboratory, usually run at a momentum of 300 GeV/c. The spill is about 1 second in duration, with a filling fraction of roughly 50% (averaged over the 18.9 nanosecond (nsec) rf structure of the machine), and is repeated every 6-7 seconds. The beam was transported $\sim$ 1.6 km from the main ring to our target in the Proton Center Laboratory (see Fig. 4), where it was focused to a spot 0.4 x 3 mm^2, with less than 1% of the beam in halo outside this spot. The beam was then deposited in a tungsten and copper plug located 7 feet downstream from our target.

The intensity of the beam could be varied, more or less upon request, from less than 10^{10} to a few times 10^{12} protons per pulse. This intensity was measured by a secondary emission monitor (SEM) located just upstream of the target and recorded every pulse. The SEM is calibrated by exposing 5 mil copper foils to about 10^{14} protons and measuring Na^{24} production, based on the measured cross section for Na^{24} production at 30 GeV.

One point to be emphasized about the beam is the rf structure, where greater than 99% of the intensity is contained in 1.5 nsec bursts spaced 18.9 nsec apart. This means that there is nothing to gain by having the resolving time of fast coincidences any better than 15 nsec.

C. Target

The target, as shown in Fig. 3, is a 0.0088 in. wide piece of beryllium. Be, a low Z material, was chosen to give a large number of hadronic interaction lengths but a small number of electromagnetic radiation lengths. The extreme thinness of the target was vital to the experiment, to insure that particles leaving the target in the direction of our detectors pass through the minimum amount of matter. (Otherwise we would suffer doubly: the electrons we want to measure would have their energy degraded; and the copious gamma ray flux produced in π^o decay would give a large background of e^+e^- pairs from conversions in the target. We still must deal with both these effects, as described in Sec. IV below, but they are kept to a minimum by using a thin target.) The extremely good horizontal focus of our beam (better than 0.4 mm or 0.015 in.) allowed us to achieve targeting efficiencies of 60% with this thin target.

The other dimensions of the target were less critical. The length was chosen to give a high enough interaction rate and still give only a small illumination of the walls of our collimator, which were radial and pointed at the center of the target. We ran with a length of 4 in., about 30% of an interaction length and giving less than 2% illumination of the collimator walls.

For ease in positioning the target, it was extended vertically and clamped at top and bottom. Thus, the effective

target height was determined by the vertical spot size of the beam, about 3 mm. This height is important since we rely on a particle's having originated in the target to measure its momentum, and an excessive target height would degrade the momentum resolution. However, a height of 3 mm gives only a negligibly small 0.3% effect on the momentum resolution.

More importantly, a shift in the vertical position of the beam would lead to a systematic shift in the measured momentum. The position of the beam in both vertical and horizontal planes is monitored with split wire ionization chambers (SWICs), which give a visual indication of the position of the beam to better than 1/4 mm both vertically and horizontally (wire spacings were 1/2 mm). Any deviations were immediately corrected with steering magnets in the target hall. (As an indication of the size of this effect, a 5 mm vertical displacement would give a 1% systematic error in momentum.)

The targeting was monitored continuosly by a scintillation counter telescope which viewed the target through a 1 mrad x 1 mrad hole in the shielding wall at an angle of 116 mrad (or about 120^{o} in the center of mass system). The targeting efficiency could be checked on a pulse-by-pulse basis by comparing the target monitor rate with the SEM measuring incident beam intensity. An additional scintillation counter telescope, located at the entrance to the target hall and viewing the beam at 90^{o}, monitored halo.

Finally several other targets could be moved into the beam by remote control for various special purposes. These included thicker Be targets to check targeting efficiencies and gamma conversions in the target, and copper and tungsten targets for hadron running.

D. Collimator

The box containing the target assembly and the beam dump extends for the first 20 ft downstream from the target. This box is filled with helium, and possible air contamination of the helium is monitored regularly by comparing the outflow from the target box with a sample of pure He. The air contamination is typically less than 0.2%. (This is important in minimizing the amount of material in the secondary beam to keep the rate of gamma conversions low.)

The steel collimator which defines the aperture and provides shielding extends for the next 30 feet. The actual aperture of 9 mrad x 9 mrad is defined by the 12 ft long precision collimator, followed by 15 ft of semi-precision collimator with a slightly oversized aperture of 9 1/2 mrad x 9 1/2 mrad (see Table I for details of the experimental geometry). The collimators are surrounded by additional steel and concrete shielding to insure that our detectors view no sources other than the target.

The collimators are tapered, with the walls radial and pointing to the center of the target, so that for a point target, there is no illumination of the walls. (As described

above, there is a 2% illumination of the walls due to the size of the target.) Furthermore, the walls of the collimators are lined with 3/4 in. of Densalloy (a high Z material predominantly tungsten), for the first 3 ft, and 1/4 in. for the next 3 ft, to prevent the escape of any electromagnetic signal produced in the collimator walls.

Vacuum windows seal the ends of the collimators, and the quality of this vacuum is monitored by a gauge viewed on closed circuit TV in the experimental trailer. For the data taking at 83 mrad, this vacuum was extended through the first of the two analyzing magnets. During the 50 mrad running, however, this vacuum ended at the end of the collimators and the magnet aperture was filled with a He bag. This was again important in reducing the matter in the beam (see Table II).

There was a 16 in. air gap between the target box and the collimators. At this position in the secondary beam, we could insert, by remote control, various foils to measure gamma conversions in a known amount of matter in order to subtract this background. We could also insert 1/4 in. of lead to produce a copious electron signal for calibration purposes, or 2 in. of lead to produce an effectively pure hadron beam for hadron background studies.

E. Magnets

We had two analyzing magnets, conventional dipoles except that the field ran horizontally to provide a vertical bend.

The total length of the magnet steel was 20 ft, and they could be run at fields up to 13 kilogauss (kG), although they were usually run at lower fields. The apertures were 10 in. vertically and 8 1/2 in. horizontally (10 in. by 7 1/4 in. for the first magnet) larger than the 9 mrad aperture so no collimation was done by the magnet. (Of course, low energy particles would be bent into the upper and lower faces of the magnet.)

The field of the magnets was mapped by measuring the integral $B \cdot d\ell$ with a flip coil at 3 currents and 37 points in each magnet. The absolute normalization as a function of current applied was checked with a Hall probe. The field was uniform to 2% within 3 in. of the center of the magnet aperture.

The current applied to the two magnets, wired in series, was measured both by a shunt and by a transductor in the magnet power supply. The polarity was switched, by remote control, roughly once a day to measure particles of both signs.

The current in the magnets selects a range of transverse momenta. The acceptance of the detectors for two typical currents is shown in Fig. 5, expressed as a percentage of the total 81 microsteradian (μsr) aperture (or 1 millisteradian (msr) in the center of mass system). Note that for a single magnet current, we are sensitive to a wide range of $p_\perp$ simultaneously, that there is a substantial overlap between

the two currents, and that at the high current the apparatus has acceptance out past the kinematic limit.

F. Trigger Counters and Hodoscopes

The arrangement of the hodoscopes and trigger counters is shown in Fig. 6 (see also Table III). The trigger counters are large scintillation counters: T0, one counter at 120 ft, TM, two counters at 150 ft, and T1, two counters at 180 ft. The two TM's are or'ed, as are the two T1's, and then a triple coincidence T0*T1*TM provides the basic trigger. These counters are boosted so as to cope with high rates; singles rates can be as high as several megacycles. Typical intensities give a triple coincidence rate of a few hundred kilocycles with 30% accidental coincidences.

An additional plane of four T2 counters is placed between the first two rows of lead glass. By demanding a pulse height of $\sim$ 20 times minimum ionizing in one of these counters, we can insure that an electromagnetic shower has started in the first row of glass, and this can be used in the electron trigger.

The hodoscopes provide the trajectory measurements used to calculate the momentum and production angle, and are also used in the slow trigger. A trajectory is specified by measuring the vertical and horizontal positions at 120 ft and 180 ft. The planes H1 and H2 measure vertical position, and V1 and V2 measure horizontal position. The size of individual counters is given in Table III. The counters in

these four planes are all 3/4 in. wide, and are overlapped 1/4 in. with each neighboring counter (see Fig. 6), so that the basic unit becomes an element (counter 12 alone is element 24; counters 11 and 12 together are element 23; 12 and 13 together are 25; 13 alone is 26, etc.) of size 1/4 in. Thus we measure positions to $\pm$ 1/8 in., giving momentum resolutions of $\sim$ 4 % FWHM and angular resolution of $\pm$ 0.05 mrad.

There are two additional planes of larger counters which are used to resolve trajectory ambiguities when more than one element per plane fires. The U plane is a set of diagonal counters, at 45^{o} with respect to H1 and V1, and is used to resolve ambiguities in those two planes. The M plane measures vertical position at 150 ft, and resolves ambiguities in H1 and H2. (Details of the ambiguity resolution are described in Sec. IV.A.2.) The U and the M planes are also overlapped, giving resolutions of $\pm$ 0.7 in. for the U plane and $\pm$ 1/2 in. for the M plane.

The counters in each of these six planes are made of Pilot type Y (see Table III) scintillator, individually wrapped, and coupled through lucite light pipes to RCA 6655A photomultiplier tubes, typically run at 900-1200 volts. The signals from each phototube are amplified times 10 on the floor of the experimental area before passing through long ($\sim$ 175 ft) cables to the trailer, where they are discriminated.

Computer programs allow the more than 200 counters to be plateaued and timed simultaneously.

G. Lead Glass

The array of lead glass is the heart of the experiment. It provides high resolution (better than 4% full width at half max) energy measurement for electrons, gives important triggering information, and gives hadron rejection of better than 10^5 when used in conjunction with the magnetic spectrometer.

The lead glass acts as a total absorption electromagnetic shower detector. The high Z of the lead glass insures the rapid development of a cascade shower upon the entrance of an electron, positron, or gamma ray into the detector, with the consequent production of a large number of particles. Each charged particle in this shower will emit Cerenkov radiation, which is readily transmitted through the glass and collected in photomultiplier tubes. The total path length of these particles will be proportional to the energy of the incident particle, and thus with good light collection efficiency we can measure a signal which depends linearly on the energy of an electromagnetic particle over quite a wide range of incident energies.[20]

The lead glass itself is a type known as SF5, with properties as listed in Table IV. Our detector used 45 identical blocks, each 14.7 x 14.7 x 35 cm^3, in a modular arrangement. (Smaller blocks would give better spatial

resolution and light collection, but would be substantially more expensive because of the greater number of surfaces to be polished and of channels of electronics needed, and would also have more "cracks" between blocks.)

Each block was glued to an RCA 8055 photomultiplier tube with Kodak HE-10 assembly cement (index of refraction 1.58). The tubes were selected from a sample of 500 for uniformity of gain and good quantum efficiency. They were run at negative high voltage so that the anode signals could be DC coupled. The blocks were wrapped first with soft aluminum foil (thickness 1 mil) which extended the cathode high voltage around the glass block to prevent leakage currents across the photocathode; then with mylar (5 mils) for insulation; and finally with black polyethelene (6 mils) for light protection. The resistor chain in the phototube bases was non-linear, with extra voltage being supplied to the first few stages for improved linearity in gain and uniformity across the photocathode.

The light output from each block of lead glass is recorded separately: The anode current from each phototube is integrated over a 270 nsec gate for each event and the resulting charge digitized in an analog to digital converter. In addition, dynode signals from the blocks are amplified, summed, and used to provide an electron trigger, allowing us to select out at the trigger stage those events which deposit large amounts of energy in the lead glass.

The blocks are arranged as shown in Fig. 7, to provide three layers of 6, 6 and 15 radiation lengths along the beam direction. The detector covers a cross sectional area of 75 cm x 75 cm, but since particles entering less than 7.5 cm from an edge of the array must be excluded due to possible energy leakage out of the array, we have a fiducial area of 60 cm x 60 cm. (A 5 cm wide vertical strip at the center of the array is also excluded from the fiducial area, since there is a gap between the first two rows of glass there for insertion of the light distribution sheet for our light flasher calibration system.) Also, as described above, there is a layer of scintillation counters (T2) between the first and second rows of glass to provide triggering information.

In front of the array is a sheet of lead 2 radiation lengths (1/2 in.) thick, with scintillation counters in front (D) and behind (E). These counters are important for hadron rejection, since demanding a large pulse height in one of the E counters insures that the electromagnetic shower has already begun in the 2 radiation lengths of lead. (Hadron rejection is ultimately limited by the charge exchange process $\pi^{\pm} + N \rightarrow \pi^{o} + N$, where all the energy of the charged pion goes to one or more π^{o}'s. The π^{o} immediately decays into gamma rays which will start a cascade shower indistinguishable from an electron initiated shower. Thus charge exchange processes occurring near the front of the array cannot be

separated from electrons, and it is important that the first two radiation lengths be lead, which has a smaller number of hadronic interaction lengths, and thus fewer charge exchanges, per radiation length than does lead glass. The remaining small amount of charge exchange background is measured and subtracted out, as described in Sec. IV.A.6.) The pulse heights in the individual T2, D, and E counters are also digitized and recorded for each event.

The entire detector thus has 29 radiation lengths, more than sufficient to contain the complete electromagnetic shower, and less than 1.5 interaction lengths. The H2 and V2 hodoscopes are located immediately in front of the lead glass array, thus specifying the entry point of a particle into the array to $\pm$ 1/8 in.

The array is enclosed in a thermally insulated box, with walls made of Alply (aluminum clad polystyrene foam). All heat sources are outside the box; in particular, the resistor chain for the phototube bases are mounted outside this box and connected to the phototube sockets with extender cables. The response time of the inside of this box to changes in the outside temperature is greater than four hours. The temperature in the room surrounding the box could then be maintained with conventional thermostat controlled heaters and air conditioners without creating fluctuations in the inside temperature. This inside temperature was monitored continuously by measuring the voltage drawn from a constant current source across a

series of thermistors and across a length of high temperature coefficient wire.

Details of the performance of the lead glass detector are given in later sections: Calibration and stability are discussed in Appendix I; triggering details are given in Sec. III.A; calculation of energy and resolution are discussed in Sec. IV.A.5; and details of hadron rejection in Sec. IV.A.6.

H. Hadron and Muon Detectors

Behind the lead glass, there are three additional detectors to aid in identifying hadrons and muons (see Fig. 8). These are a crude hadron calorimeter (the $\pi\mu$ counters), a crude hadron telescope (the πe counters), and a muon hodoscope (μ picket counters).

The $\pi\mu$ counters consist of sheets of steel, total length 970 gm/cm^2 Fe equivalent, with four large 3 ft x 3 ft x 1/2 in. scintillation counters interspersed in the steel (see Fig. 8 for locations) to sample the hadronic shower.[21] The pulse height in each of these counters is recorded for each event. As a calorimeter, the $\pi\mu$ counters (together with the 1.5 interaction lengths of lead glass) give an energy resolution of only about 75% FWHM. Thus these counters are not used for energy measurement, but rather as an aid in particle identification (see Fig. 9), and the energy measurement for hadrons is taken from the hodoscopes.

The πe counters consist of twelve 3 ft x 11 1/2 in. x 1/8 in. scintillation counters, arranged as three separate telescopes of four counters each, each covering 1/3 of the total aperture. The counters are at the location of $\pi\mu 2$. The presence of a track (3 or 4 out of 4 counters firing) in one of the three telescopes is used as a hadron trigger, and the absence of a track as an electron trigger, since electromagnetic showers are fully quenched at this location while a hadronic shower would be nearing its peak.

The need for a multiple coincidence follows from the fact that a large flux of very soft photons (amounting to about 1% of the total energy) does emerge from the lead glass. These photons could set a single counter but cannot give coincidences.

The μ picket counters are a hodoscope of sixteen 30 in. x 2 in. x 1/4 in. scintillation counters located after all the steel, measuring horizontal position. These counters are used to generate a muon trigger, and give an additional coordinate for trajectory reconstruction of muon events.

I. Electronics

A schematic diagram of the triggering and data acquisition electronics is shown in Fig. 10. Special features which merit detailed discussion are the analog to digital converters, the DC logic system, the NEVAC data crate, and the interface.

1. ADC

The ADC's, which digitize the pulse heights in the lead glass, T2, D, E, $\pi\mu$, and other counters, were designed by F.W. Sippach and built at Nevis Labs. These digitizers integrate the current in an anode signal by charging a capacitor with the input current while a gate is open, and then generate an 80 MHz pulse train while the capacitor is discharging at a fixed rate. This pulse train is then counted by a 10 bit scaler, completing the digitization of the original analog signal. The standard gain was $\sim$ 500 picocoulombs per full scale of 1024 channels represented 70 GeV for the lead glass blocks. The input sensitivity could be lowered a factor of two with a switch on the front panel of each digitizer. Additional less standard features of the digitizers included:

1. Pedestal injection: Each time the digitizers are gated, a fixed amount of charge is injected at the input stage. This allows a precision calibration when the gains of the digitizers are adjusted using feature 2.

2. Adjustable gains: The discharge rate of the capacitor is controlled by an external voltage supply. Varying this voltage and measuring the gains with the pedestal injection yields a substantial expansion in the dynamic range of the digitizers. This was particularly important in muon calibration, when the gain was raised by a factor of 20 to measure muon straight-throughs : Muons which deposit a fixed

but small amount of energy in each block of lead glass, and constitute a monitor of the stability of the lead glass gains.

3. Base line correction: An electronic servo constantly adjusts the base line of the digitizers to remove noise and low frequency oscillations. Only the signal above this base line is digitized.

4. Isolation: The digitizer outputs were transformer coupled, as were input gates, and the racks of digitizers were physically isolated. The only ground was supplied by the DC coupled input signals, minimizing group loop problems.

2. DC Logic

The logic system is the centerpiece of a two stage triggering process which allows us to make complicated logical decisions at the triggering stage without extensive timing of fast logic pulses. The first, or fast trigger, is derived from coincidences of pulses from the trigger counters. It causes all other hodoscope and bit information (see Table V) to be gated into coincidence registers and stored in the DC logic. The only timing that is necessary is done here, at the entrance to the DC logic, where the various signals in Table V are all brought into time with the gate generated by the fast trigger. (The resolving time of this gate need only be as good as 15 nsec because of the rf structure of the accelerator.) The logical level of the fast trigger is only that required to bring its rate to less than 100 kilocycles.

The rest of the logic is done on DC levels in the registers. This allows generation of whatever logical combinations of the DC logic inputs that are desired. Among the modules available for use in the DC logic are ands, ors, sigma modules, which add up the number of counters that fired in each hodoscope plane, and master sigmas, which put global requirements on all the hodoscope planes. The exact logical functions used in our experiment are described below in Sec. III.A.

The DC logic ends with the logic bus (see Table VI) which can make arbitrary coincidences and anti-coincidences of up to 15 signals generated in the DC logic and present at the input of the logic bus. This logic bus then generates the low rate, or "slow" trigger (TGO), which causes the gate to the digitizers to be generated, the digital information to be strobed into data buffers, and the entire event to be read into the computer. The DC logic makes a decision in 130 nsec after the fast trigger, and then either generates a slow trigger or clears itself to be ready for the next fast trigger.

3. NEVAC Crate

The NEVAC crate is the funnel through which all data flow into the interface and computer. It contains a crate controller which connects to a standard CAMAC Branch Highway, but can operate at data rates of up to 1 megacycle, twice as fast as CAMAC standard, since it is built with MECL rather

than TTL integrated circuits. The modules in the NEVAC crate include: digitizer scalers, octal 10-bit scalers which store the digitized pulse heights; a hodoscope address encoder, which generates a unique 8-bit address for each of the hodoscopes that has fired and transmits the hodoscope information to the interface as a list of addresses; data buffers, which transmit miscellaneous bit information; a packing module which packs the 10-bit scalers into 16-bit words as they are read by the interface; and a pulse generator module, through which the computer can communicate electronically with various pieces of apparatus.

4. Interface

The interface, designed by H. Cunitz and, like the rest of the electronics, built at Nevis Labs, acts as a CAMAC Branch Driver to communicate with the experiment, and as a peripheral device to communicate with the computer. It also has a number of special features, including: a 16 word, 32-bit random access memory (RAM), in which a program of CAMAC commands can be stored; four trigger inputs, each of which causes the interface to begin execution of the program stored at a specific location in the RAM, initiating transfer of an event to the computer; a data formatter, which can stack and unstack data for transmission to the computer as 16-bit words; an interrupt structure, which notifies the computer upon completion of event transmission or when errors occur; and complete facility for off-line operation.

J. On-Line Computer

The experiment was on-line to a PDP-15 computer, dedicated to the experiment. The computer includes 32 K of 18-bit memory, two 9-track tape drives, a line printer, teletype, visual display scope, fixed head disk, and floating point hardware. This configuration allows for rapid data taking together with extensive monitoring of the performance of the various parts of the experiment and full analysis of a sample of events on-line. The computer also can interact with the experimenters to perform a wide variety of tasks on command.

III. DATA TAKING

A. Triggering

As described above, there are two levels of triggering in the experiment. The first, or fast trigger, causes hodoscopes and other data to be gated into coincidence registers in the DC logic system. This trigger is derived only from coincidences of pulses from the trigger counters. The second, or slow trigger, gates analog information into the digitizers and causes the event to be transferred to the computer. This slow trigger is derived from complicated logical functions of the data stored in the registers.

More specifically (see Fig. 10 for a schematic diagram of the logic for the experiment), there are three different signals which are or'ed together to create TGI, the fast trigger which gates the DC logic. These three are e, π, and random. The fast π trigger is a triple coincidence T0*T1*TM, prescaled by an appropriate factor (typically 4000 or 8000) so that about 10% of the data sample on tape will be pion triggers. Thus this trigger is simply a specific unbiased fraction of those events where a particle passes through the apparatus (or there is a random coincidence of trigger counters). The random trigger is a triple coincidence QED (the 116 mrad target monitor telescope), separately prescaled (typically by 1000) to give 5% of the data sample; i.e., a specific fraction of those rf buckets where a beam particle interacts in the target.

Finally, the fast "e" trigger, which gives us our actual data, is a double coincidence of T0*T1*TM unprescaled with T2, the trigger counter between the first two rows of lead glass. This T2 is actually four separate counters which together cover the whole aperture. The gains of the four counters are equalized by adjusting the voltages on their phototubes to give equal pulse heights for minimum ionizing particles. The four counters are then passively added, amplified, and discriminated. The discriminator threshold is set high enough to reduce the fast trigger rate by a factor of at least 10 so that DC logic deadtime will be low, and low enough so as to still be 100% efficient for electrons, which begin to shower in the first row of glass and give large pulse heights in T2. The ease with which we can satisfy both of these conditions is shown in Fig. 11, which shows the trigger threshold for a particular T2 counter together with the spectrum of pulse height in T2 for electrons, with a clear separation between the threshold and the start of the electron signal. This threshold, about 22 times minimum ionizing, cuts the T0*T1*TM rate down by a factor of 20-30.

(The individual T2 pulse heights are recorded for each event, and the percentage of time each T2 counter was above threshold is reported for each run by the on-line computer. Comparison of these pulse heights and percentages with standards provides a check that all four T2 counters are working properly at all times.)

Each fast trigger gates the information shown in Table V into the register logic. Once this information has been stored as DC levels in the DC logic, a wide variety of logical functions of the data can be derived by the logic, as described in Sec. II.I. In particular, we use the DC logic to produce the following signals:

1) Hodoscope 6/6: Each of the six hodoscope planes (H1, V1, U, M, H2, and V2) has a sigma module which counts the number of counters that fired in that plane. We then combine the outputs of the various sigmas to produce the 6/6 signal, which requires at least one counter in all six planes. (For certain special runs where normalization is not a concern and we merely want to insure the maximum number of reconstructable events on tape, this signal is set to require exactly 1 or 2 counters in each plane.)

2) Hodoscope 5/6: This signal, again produced by combing sigma outputs, requires at least one counter in exactly 5 of the 6 planes. It is not used in triggering, but as a monitor of hodoscope efficiencies.

3) $\bar{\pi}e$: This requires less than 3 of the 4 counters in each of the πe telescopes: i.e., it requires no track after the lead glass. It is used in the electron trigger as an additional hadron veto.

4) $\bar{e}\pi$: This requires a track (3 or 4 of 4) in one of the πe telescopes. It is used in the pion trigger.

5) μp: This requires at least one (or in some running

conditions exactly one) of the μ picket counters. It is used in the trigger for muon calibration.

The next step in producing the slow trigger is the logic bus (see Table VI). Fifteen different signals are supplied at the inputs of the logic bus. These are of two types; either the derived signals described just above (bits 2,3,7,10,14), or other signals which are produced conventionally in the fast logic and gated directly into registers (bits 4,5,6,8,9,11,12,13).

In particular, bits 11, 12 and 13 are three separate thresholds on energy deposit in the first two rows of lead glass. The dynode signals from these 20 blocks in the first two rows are passively added, amplified, and then discriminated at three separate levels, low, medium, and high, to produce the signals ϵ_{12}^{L}, ϵ_{12}^{M}, and ϵ_{12}^{H}. These are used to create three distinct electron triggers. The middle trigger is the prime data trigger, the high trigger gives a sample of events enriched at higher energies, and the low trigger serves as a constant check on the efficiency of the two higher thresholds, as well as giving an enriched sample of low energy events.

The low and middle levels are prescaled in the DC logic so that triggering rates will be more nearly equal over the entire range of $p_\perp$ available, despite the several order of magnitude difference in cross sections at the two ends of the $p_\perp$ spectrum. The efficiencies of these three levels

can be seen in Fig. 12 for a typical running condition, together with the acceptance. The low threshold is 100% efficient over the entire acceptance, as is the middle threshold for all but the lowest $p_\perp$. The thresholds are adjusted with changes in magnet current to preserve this relation between the thresholds and the acceptance.

These various bits can then be combined in coincidence or anti-coincidence in logic modules on the bus to produce triggers. As shown in Table VI, we normally run with five triggers: low, middle and high electrons, pions, and randoms. The random trigger is just the fast random trigger in coincidence with the beam gate. The pion trigger is a coincidence of the fast pion trigger, beam gate, hodoscope 6/6, and $\bar{e}\pi$ (although some running was done without $\bar{e}\pi$ in the pion trigger). The three electron triggers are coincidences of fast e, beam gate, hodoscope 6/6, $\bar{\pi}$e, and one of the three prescaled ϵ_{12} levels. (The logic bus also produces a large number of logical combinations which are not normally used as triggers but are counted in blind scalers and recorded as checks on the operation of various parts of the experiment.)

These five are then or'ed together to produce TGO, the slow trigger. This generates the gate for the digitizers, causing all analog information to be stored, and also strobes all digital information into data buffers. After a delay of about 20 μsec to cover digitization time, a trigger is sent to the interface which causes the event to be transferred to the computer.

In addition, there are forty 24-bit blind scalers which record the rates of beam and target monitors, fast and slow triggers, and various signals used as checks. At the end of each 1-sec long machine pulse, a separate trigger is sent to the interface which causes the blind scaler totals for that pulse to be sent to the computer, and then resets the scalers for the next pulse.

B. On-Line Program

As described above, the experiment is on-line to a dedicated PDP-15 computer. The on-line program sets up the interface in preparation for data taking, and then performs three major functions: During the beam spill it accepts events from the interface and stores them in certain areas of memory reserved as data buffers; at the end of the spill it writes the data buffers onto magnetic tape; and in between accelerator pulses, it analyzes a sample of the data as a check on the apparatus and to produce preliminary physics information.

During the beam spill, the program just fills up the data buffers with events, doing a minimum amount of book-keeping so as to keep deadtime low. Each event, consisting of about fifty 16-bit words, creates a deadtime of about 300 μsec while the event is read into the computer, assigned an event number, and the buffer is checked to make sure enough room is left for the next event. (The length of an event varies because of the varying number of hodoscope addresses generated for different events.) Seven 1500

word areas of core are reserved as data buffers, allowing about 200 events per pulse before needing to empty a buffer. For normal data taking, beam intensity and triggering thresholds are adjusted to keep the event rate below 200 per pulse so that no events need be written on tape during the beam spill, thus keeping dead times low. For calibration and test runs where absolute normalization to the number of interacting protons is unimportant, the buffers are emptied onto magnetic tape and refilled during the beam spill, allowing about 600 events per pulse to be recorded. (At this rate, a standard 2400 foot tape is filled in half an hour.)

At the end of the beam spill, the computer first reads the blind scalers, which are stored in a separate buffer and output on tape every 20 pulses. The data buffers are then written onto tape as 1500 word records. Also at this time, the program will accept commands from the experimenters, such as to end a run, to output certain data on the line printer or visual display scope, or to define a histogram to be accumulated.

During the 5-6 seconds between pulses, the program analyzes the data in the most recently filled buffer. (Thus, at typical data rates, somewhere between 1/4 and 3/4 of all events are analyzed on-line.) Each event is analyzed in much the same manner described below in Sec. IV.A: A geometric reconstruction is made of the event, the momentum from the

magnet-hodoscope system and the energy from the lead glass are calculated, and various cuts, which can be varied on request, are applied to separate out electrons from hadrons. Up to twenty histograms, of various quantities such as momentum, energy deposited in the lead glass, fraction of energy deposited in the lead glass, geometric quantities, etc., subject to various cuts, are updated for each event, and scatterplots of pairs of quantities can also be made. By studying different histograms, a great deal about the performance of the experiment can be learned on-line.

In addition, the program keeps track of the number of times each of the trigger counters and hodoscopes has fired, the number of times more than 1 GeV of energy is deposited in each block of lead glass, the percentage of events which can be reconstructed, etc. All these quantities are output on the line printer at the end of each run (about every hour), and comparisons with standard values can immediately pinpoint the location of most malfunctions in any part of the apparatus.

Finally, the on-line program also performs various special functions, such as taking light flasher calibration runs, and plateauing and timing all counters simultaneously.

C. Running Procedure

The most important aspect of our running procedure is dictated by the need to measure the spectrum of electrons produced by conversions of gamma rays coming from π^o decay. Measurement of these electrons allows us to calculate the π^o

production spectrum. (In addition, these electrons represent a background to the directly produced electron signal.) We measure these conversion electrons by inserting foils of known thickness into the secondary beam and then plotting the yield of electrons as a function of foil thickness (see Sec. IV.B.3).

We thus take a series of runs with different foils. We use foils of 12, 24, and 36 mils of brass (0.012, 0.024, and 0.036 inches), corresponding to 2%, 4% and 6% of a radiation length of matter. These runs are interspersed with "air" runs, where no additional material is placed in the beam, leaving only the 0.7% of a radiation length due to target thickness, vacuum windows, etc. (see Table II). In addition, runs are taken with 2 in. of lead placed in the secondary beam, to give us an effectively pure hadron beam to allow us to measure background due to misidentification of hadrons as electrons. A typical run lasts one hour and results in 50,000 events on tape.

A typical run cycle, at a given magnet current and polarity, consists of about 5 air runs, one 12-mil, two 24-mil, one 36-mil and two 2-in. Pb runs. Such a cycle could be completed with about 12 hours of steady beam. At this point, either the magnet polarity would be changed to measure particles of the opposite charge, or the magnet current would be changed to measure a different region of $p_\perp$, and a new run cycle would begin.

In addition, a variety of special runs would be taken, about once per day. These included electron calibration runs, where 1/4 in. of lead was inserted in the secondary beam to give a large yield of electrons to allow us to monitor the stability of the lead glass calibration; muon calibration runs, where the gains of the digitizers were changed by a factor of 20 and we ran with a muon trigger to measure the energy deposit by muon straight-throughs in the lead glass, as a further check of stability; threshold study runs where the lead glass thresholds were removed from the trigger so their efficiencies could be checked; and runs with a wider Be target, as a further check on γ conversions in the target and targeting efficiency.

Finally, at each angle and polarity, a series of special runs using only a pion trigger was made with a series of different targets. Electron data could only be taken with thin Be targets because of the problem of γ conversions, but hadron data were taken on Be, Cu, and W targets, allowing us to measure the A dependence of high $p_\perp$ production. Certain of these runs were made with a modified trigger to enhance the rate of high momentum hadrons.

Each run, a set of numbers would be produced by the on-line program, including rates in all the counters, blind scaler totals, triggering rates, etc. The most important rates were entered in a run log and checked on a run-by-run basis. Various other apparatus checks were performed once

per eight hour shift, including checking the air contamination of the He in the target box, checking the voltages on each counter, and taking a light flasher calibration run as a further check of lead glass stability.

IV. ANALYSIS

The analysis of the data consists of three major stages: event-by-event analysis, where the energy and production angle for each event are calculated and electron events are selected by a series of cuts; run-by-run analysis, where a comparison of the electron yields from different runs allows us to deduce the e and π^o spectra; and absolute normalization.

A. Event-by-Event Analysis

Each event recorded on tape contains the following information:

i) Digitized pulse heights for 64 channels of ADC's (including 45 blocks of lead glass, four T2 counters, three E counters, three D counters, four $\pi\mu$ counters, three sums of lead glass dynodes, and two miscellaneous);

ii) Address list, containing a list of all hodoscopes in the planes H1, V1, U, M, H2, V2 and μ picket that fired for the event;

iii) Logic bus word, containing the bits of the logic bus; and

iv) πe word, containing bits showing which πe and trigger counters fired for the event.

Each event is processed through the following series of steps (each described in more detail below):

1) Examination of the logic bus word determines what kind of an event this is (electron, pion, or random). For

the moment, I consider only events generated by one of the electron triggers; pion events are discussed later.

2) Geometrical reconstruction of the event using the hodoscope addresses. Events which, after resolving potential ambiguities, have a unique track are assigned coordinates at each hodoscope plane; other events are lost.

3) A trajectory is fitted to the coordinates and the momentum P and production angle θ for the event are calculated.

4) Fiducial cuts are applied to the event.

5) Energy deposit E in the lead glass is calculated.

6) Electron cuts are applied, based on the πe counters, the E and D counters, the comparison of E and P (i.e., demanding that the particle deposit all of its energy in the lead glass), and the distribution of the electromagnetic shower in the lead glass.

7) Events which pass these cuts and are thus identified as electrons are collected in bins of $p_\perp$ and θ.

In addition, certain types of events are counted and used for normalization purposes, as described in Sec. IV.B.1.

Considering the stages of the event-by-event analysis in more detail:

1) Logic bus word: As described above, the slow logic generates several independent triggers, which under normal running conditions include three electron triggers, a pion, and a random trigger. (See Table VI.) Electron triggers are selected out by requiring the presence of bits 4, 5, 10

and 14, and then subdivided based on bits 11, 12 and 13 (the low, middle, and high lead glass thresholds). These low, middle, and high events then go through the subsequent analysis separately, leaving us in the end with spectra based on three independent thresholds. Pion events are also selected and dealt with separately.

2) Geometric reconstruction: As described above (see Fig. 6), there are six planes of scintillation counter hodoscopes that record particle trajectories. The list of hodoscope addresses is divided up into lists of the counters that fired in each plane, and then further broken down into lists of elements (i.e., if two adjacent counters fired, it is assumed that a single particle passed through their region of overlap).

If there is only one element in each of the H1, V1, H2, and V2 planes, we can proceed to the trajectory fitting. However, if there is an extra element in any of these planes, we must first resolve this ambiguity. This is done by these following series of steps. (At any step we may lose the event, either because there is no valid trajectory that fits the criteria we are using to resolve ambiguities, or because we are left with a terminal ambiguity that cannot be resolved. Instead, if after any step we are left with only one element in each of H1, V1, H2 and V2, we assume we have found the correct track and proceed to trajectory fitting, skipping the rest of the reconstruction. See Fig. 13 for a schematic diagram of this process.

a. We use the target position to resolve ambiguities in V1 and V2, which measure positions in the horizontal plane where there is no bending. The validity of this procedure can be seen from Fig. 14, the horizontal coordinate at the target for unambiguous events which shows a very small number of tracks from outside the target region. We consider all pairs of elements in V1 and V2, and eliminate those which do not project back to the target.

b. We use the U plane, the diagonal hodoscope, to resolve ambiguities in H1 and V1. We consider all H1 V1 pairs. The pair then specifies a particular U element, and we eliminate those for which the appropriate U element did not fire.

c. We use the M plane to resolve ambiguities in H1 and H2. These planes all measure vertical positions after the bend. A line through each H1 H2 pair specifies a particular M element, and we eliminate pairs for which that element is not on.

d. Finally, we use the magnet aperture to further resolve H1 H2 ambiguities. If there are still two fully valid tracks remaining, we choose the one which comes through the magnet aperture rather than one which passes through the iron of the magnet.

This procedure yields a unique track for about 80% of all electron triggers under standard running conditions, and a somewhat lower percentage for high intensity runs where

there are more accidentals in the hodoscopes. The actual "reconstruction efficiency" is discussed below under absolute normalization.

Those events which required any or all of the above steps to resolve ambiguities are flagged, so that the sample of clean events with no reconstruction needed can be studied separately to check that the reconstruction procedure has not introduced any biases.

3) Trajectory fitting: Once we have a unique x and y coordinate at 120 and 180 ft (the location of the hodoscopes), we can project this trajectory back through the magnet and determine the momentum and production angle, using the assumption that the particle originated in the target. Crudely, this can be done as shown in Fig. 15, where we assume a single bend at the center of the magnets, whereupon the bend angle (and thus also the momentum) are easily evaluated in terms of the measured trajectory coordinates. (This is the method used in the on-line program.)

More exactly the trajectory is fit by an iterative procedure. An average magnetic field integral is used to calculate an initial trajectory. The actual field integral along that trajectory is then evaluated, using the field map, allowing a new trajectory to be computed.

The momentum resolution we obtain depends on the amount of bend in the magnet. Typically, for 500 amp running, the resolution is 2.5% FWHM ($\pm$ 1% rms) at 25 GeV/c and 5% FWHM

at 50 GeV/c. (This is an ideal resolution. The actual momentum resolution is slightly worse due to multiple scattering and hodoscope inefficiencies.)

The angular resolution is even better. We measure two independent angles, θ_x and θ_y, the production angles in the x and y directions, measured from the center of our collimators. Thus θ_x and θ_y both run from -4.5 mrad to +4.5 mrad. θ_x is known quite well (to $\pm$ 0.05 mrad) since there is no bend in the horizontal plane. θ_y is not known as well (only to $\pm$ 0.2 mrad) because of the vertical bend and because it is correlated with the momentum, but the angular resolution is not very sensitive to errors in θ_y since the production angle θ is given by

$$\theta \approx \sqrt{(\theta_x + \theta_{AP})^2 + \theta_y^2}$$

where θ_{AP} is the angle of the center of the collimator with respect to the beam line, either 50 or 83 mrad. Thus, the overall angular resolution is $\pm$ 0.05 mrad.

4) Fiducial cuts: A typical set of fiducial cuts is shown in Table VII. These cuts eliminate events near the edges of the collimator, near the edges of the lead glass (where energy resolution is degraded by leakage out of the array), and near the vertical strip in the center of the array.

5) Energy calculation: Naively, we can calculate the energy deposited in the lead glass array by simply adding up the energy in each of the 45 blocks. (An up-to-date

calibration constant is known for each block, as described in Appendix I, and so the energy in each block is just the pulse height above pedestal recorded for that event times the calibration constant.) However, dramatic improvements in energy resolution can be achieved by a slightly more sophisticated calculation.

First, since the cascade shower is of limited spatial extent, it is not necessary to add in all 45 blocks. In fact, due to the long (270 nsec) gate on the lead glass anode signals, it is important to exclude as many blocks as possible from the energy sum to avoid degrading the resolution with random pile-up in blocks not associated with the actual shower. But, since we know the entry position of the particle into the array to $\pm$ 1/8 in. from the hodoscopes, we can restrict the sum to these blocks within a specific distance of this entry point. In fact, we can choose a different distance for each of the three rows of the array to compensate for the spreading of the shower as it develops. The distances chosen are to include all front row blocks within 2 in. of the entry point, all second row blocks within 2 1/4 in., and all third row blocks within 2 1/2 in.

In addition, there are three corrections that further improve the resolution. First is a transit correction, to correct for different attenuation of light for particles entering at different horizontal positions, and thus at different distances from the phototubes on the blocks in the first two rows. (See Fig. 16, a front view of the lead

glass array, for an illustration of this and other corrections.) The magnitude of this effect is 1% increase in light for point B with respect to point A (see Fig. 16), and a 6% increase for point C with respect to A.

Next is a crack correction, to correct for energy leakage in the small (less than 1/4 in.) cracks between adjacent blocks of glass due to wrapping and the supports for the blocks. The size of this correction is a 2% decrease in light for point D relative to point E.

Finally, different entry points will have different numbers of blocks included in the sum, and thus different amounts of random pile-up. An additional correction is made for this effect, adding 1.4% when only one rather than two horizontal rows are included in the sum (point F compared to point G), and adding 0.4% when only one vertical column of third row blocks are included in the sum (point H vs. point I). The correction is in this direction (adding energy when too few blocks are included in the sum) because the calibration constants are based on adding two rows and two columns, or a total of 8 out of the 45 blocks.

The result of all these corrections is a uniformity in energy as a function of entry position of better than 0.5%. The energy resolution is then limited only by the statistics of shower development and light collection. The energy resolution cannot be observed directly since a monochromatic electron beam is not available, but can be measured in

quadrature with the momentum resolution of the magnet. Figure 17 shows the energy deposited in the glass, normalized to momentum measured by the magnet-hodoscope system, for different momentum ranges with different momentum resolutions. This indicates that the energy resolution of the lead glass is better than 3.5% FWHM, and that the linearity as a function of energy is better than 1/2% from 20 to 40 GeV.

6) Hadron rejection: Once we have calculated the momentum, angle, and energy deposit in the lead glass for each event, we are faced with the problem of separating out the electrons. The size of this task is indicated by Fig. 18, which plots the energy deposited in the glass divided by the momentum (E/P), i.e., the fraction of a particle's energy it leaves in the lead glass, for pion triggers. Electrons, which leave all of their energy in the glass, are expected to appear as a peak near 1.0 on this plot, but any small peak is obscured in the tail of the hadrons, which usually leave only a fraction of their energy in the glass and thus appear to the left of 1.0 on the E/P plot.

The first tool for hadron rejection is the ϵ_{12} thresholds in the electron trigger, described above in Sec. III.A. The result of these thresholds, which demand a large energy deposit in the first two rows of lead glass, is shown in Fig. 19, where there is a suggestion of an electron peak near 1.0 on the E/P plot. In order to further separate electrons from hadrons, we must use the information we have on the longitudinal distribution of the electromagnetic

shower in the glass.

The first piece of information available to us is the pulse height in the E counters, which are located just in front of the lead glass and behind two radiation lengths of lead. By demanding a large pulse height (about 7 times minimum ionizing) in the E counters, we insure that the shower have started in these first two radiation lengths. Figure 20 shows the effect on pions and on electrons of a cut on E counter pulse height at various levels. Putting the cut in channel 100 yields a hadron rejection of 70%, while cutting less than 5% of the electrons. (We first put a cut on the D counter pulse height to insure that only a single minimum ionizing particle enters the two radiation lengths of lead.)

Next, we can use the energy distribution in the three rows of lead glass. Figure 21 shows the percentage of energy deposited in the first, second, and third rows of glass for electrons and for pions, and shows how a cut on these quantities gives additional rejection. (Actually, these cuts are a function of energy, since the rate of shower development depends on energy. Figure 22 shows the variations in energy deposit in the three rows of glass as a function of energy.)

The result of these cuts is the E/P distribution shown in Fig. 23, where a clear electron peak is visible. The combination of these cuts together with the requirement that the particle deposit all its energy in the lead glass gives

a hadron rejection of better than 1 in 10^4 (i.e., less than 1 hadron in 10^4 appears between 0.95 and 1.05 on the E/P plot and passes all the electron cuts).

Moreover, we can achieve even better hadron rejection by doing a background subtraction. Placing 2 in. of lead in the secondary beam creates an effectively pure hadron beam, and Fig. 24 presents the E/P distributions, before and after electron cuts, for this hadron beam, together with the cut distribution for a mixed electron-hadron beam repeated from Fig. 23. This shows that there is no artificial electron peak produced by the cuts, and that the shape of the cut E/P distributions agree very well away from the electron peak. We thus feel justified in assuming that the background under the electron peak is measured by the 2 in. Pb data, and that we can subtract this background. The subtraction leaves us with a hadron rejection of better than 1 part in 10^5.

Of course, the hadron measurement is independent of this background subtraction, since the π^o spectrum is derived solely from the excess electron yield in runs where the foils are inserted into the secondary beam.

7) Binning the data: Now that we have established an electron signal, we can simply count the number of events in each bin of $p_\perp$ and θ that pass all electron cuts and lie between 0.95 and 1.05 on the E/P plot. Later, in the run-by-run analysis, we will compare these electron yields from various runs to determine the source of the electrons.

Steps 1, 2, 3 and 5 in this event-by-event analysis are performed by a first pass through the raw data tapes, and a data summary tape (DST) is produced. This DST contains the various calculated quantities for all those events which reconstruct and for which $E/P > 0.6$. Later passes through the DST's apply the various cuts and compute the electron yields for each run. In this way, the data can be processed repeatedly with differing electron cuts, fiducial cuts, and selections of reconstructed events to insure that the final results do not change dramatically with small variations in the cuts.

Finally, a word about the analysis of pion events. These are reconstructed and have momentum and angle computed in the same way as electron events. The rest of the analysis for pions simply involves putting a cut on the summed $\pi\mu$ pulse heights to insure that the event is a real high energy hadron and not a muon, accidental, or low energy particle, and binning the events as a function of $p_\perp$.

B. Run-by-Run Analysis

The output of the event-by-event analysis is, for each run, an electron yield as a function of $p_\perp$ and θ. The next task is to determine the source of the observed electron signal. In particular, we must separate out directly produced electrons, conversion electrons (used to derive the π^o spectrum) and background (Dalitz pairs and hadron feedthrough).

As described above, this is accomplished by taking the data in a series of runs with foils of various thicknesses inserted into the secondary beam. This allows us to measure the number of electrons due to gamma conversions in the small amount of matter in our secondary beam, and to directly measure the hadron feedthrough (misidentification of a hadron as an electron) with the 2 in. Pb runs. Thus we can make quite accurate separation of the various sources of electrons.

The run-by-run analysis consists of the following steps:

1. Normalization of each run to an equivalent number of interactions in the target.
2. Correction of the electron yield for bremsstrahlung energy losses in passing through the foils.
3. Fitting the electron yield as a function of foil thickness (including hadron background subtraction), giving a measurement of the number of directly produced electrons and of conversion electrons as a function of $p_\perp$ and θ.

Considering these steps in more detail:

1. Normalization: The most straightforward normalization of a series of runs, all taken at the same angle, magnet current, and polarity, is to use the apparatus itself as a target monitor. We start with the original sample of events, with the same reconstruction and fiducial cuts. An additional fiducial cut is placed on ε_{12}, the energy deposited in the first two rows of lead glass, at a slightly higher level than that imposed by the trigger, so as to be insensitive to any

slight varistions in the trigger thresholds. (The value of this cut depends on the magnet current, which selects where our momentum acceptance begins. A typical value was 30 GeV for the conditions of Fig. 12, which shows the trigger thresholds.)

We then take the number of events remaining in the region between 0.60 and 0.89 in the E/P plot (see Fig. 19), i.e., those events leaving between 60% and 89% of their energy in the lead glass. This region is free from electromagnetic events, and thus provides a normalization independent of the amount of electromagnetic signal produced by the various foils. Furthermore, the number of events in this region is typically 10 times the number of electron events, and so the statistics of this normalization has no effect on the final answer. This normalization proved to be quite reliable, as the variations in normalized electron yields for identical runs were well described by statistical errors on the number of electrons, and its reliability is also verified by the linearity of the plots of electron yield as a function of foil thickness.

2. Bremsstrahlung correction: There is a small but unavoidable energy loss as electrons pass through matter, even with the thin (2-6% of a radiation length) foils that we use. Moreover, since the spectrum of electrons is falling steeply with momentum, we must correct for this effect, or we would be comparing different parts of the electron spectrum for different foil thicknesses (due to differing energy losses

as a function of thickness), and the steeply falling spectrum would lead to distortions.

This correction is evaluated by integrating the formula for the probability of electrons of energy E_1 emerging for an incident electron of energy E:

$$W(E,E_1) = \frac{1}{E} \frac{\mathrm{Log}(E/E_1)^{(4/3\ t-1)}}{\Gamma(4/3\ t)}$$

and is checked by extensive Monte Carlo calculations for particles with a given initial energy spectrum passing through thin foils. It is possible to parametrize the results by the formulae:

$$N(E^e_{out}) = N(E^e_{in})e^{-\beta t} \qquad (4)$$

for the electron yield after t radiation lengths and

$$N(E^e_{out}) = \frac{\alpha}{\beta-\alpha}\, e^{-\beta t}\, (e^{(\beta-\alpha)t}-1)\, N(E^\gamma_{in}) \qquad (5)$$

for the yield from gamma rays where $N(E^e_{in})$ is the initial number of electrons, $N(E^\gamma_{in})$ is the initial number of gamma rays, and $N(E^e_{out})$ is the number of electrons emerging from the foil, $\alpha = 7/9$, the standard relation between radiation and conversion lengths, and β is the parameter to be determined. These formulae describe the Monte Carlo results well, and are not very sensitive to the exact foil thickness or the exact shape of the input spectrum or momentum, with $\beta = 3.4$.

The electron signal has three separate components, each of which is corrected differently. The first is electrons produced at the target (either directly produced electrons or

Dalitz pairs from π^o decays), which are corrected according to Eq. (4). The next is electrons produced from gamma conversions, which are corrected according to Eq. (5). The last is hadron background, which are not really electrons and so are not corrected at all. Knowing the relative sizes of these three components (determined from the foil thickness plot described just below), we can evaluate the size of the correction needed for each foil. The corrections come out to be 2.1% for "air" (no foils in the beam), 7.3% for the 2% radiation length foil, 12.1% for the 4% foil, and 17.0% for the 6% foil. The size of the corrections can be seen in Fig. 25, where the corrected and uncorrected electron yields are plotted as a function of foil thickness. The linearity of this plot for the corrected points gives us confidence in the validity of the corrections.

3. Foil thickness plot: Finally, we can plot the electron yield as a function of foil thickness and deduce the spectrum of conversion and of direct electrons. Figure 25 shows such a plot for a typical set of data. (This figure is summed over $p_\perp$.) For each angle, magnet current, and polarity, a set of plots is made, with one plot for each bin of $p_\perp$ and θ. Then, we can read off the number of conversion electrons from the slope and the number of direct electrons from the intercept in each of these plots, obtaining the electron spectra as functions of $p_\perp$ and θ.

The slope of this plot is, by definition, the number of conversion electrons produced by 1% of a radiation length of matter. The spectrum of conversion electrons, obtained by measuring this slope as a function of $p_\perp$, allows us to deduce the π^o production spectrum. (See Sec. V.B below.) In addition, knowledge of this slope permits us to subtract two crucial backgrounds from the directly produced electron signal.

As shown in Fig. 25, the electron yield with no foils placed in the secondary beam has three major components in addition to the directly produced electrons: conversion electrons, electrons from π^o Dalitz decays $\pi^o \rightarrow e^+e^-\gamma$, and misidentification of hadrons as electrons. The hadron background is measured and subtracted as described above (Sec. IV.A.6), by using the 2 in. Pb runs. Conversion electrons are subtracted by extrapolating the foil thickness plot back to zero matter in the secondary beam, based on the known amount of material in the beam (0.7% of a radiation length at 83 mrad; see Table II). In other words, the measured slope tells us how many conversion electrons are produced by a given amount of matter, and knowing how much material is in the beam permits us to do a precise subtraction of this background.

Finally, the known branching ratio for π^o Dalitz decays allows us to subtract this background in the same manner. These Dalitz electrons produced by internal conversions come from the same source, the π^o's, as do the electrons from

external conversions discussed above, and the branching ratio tells us the Dalitz decays produce a number of electrons equivalent to 0.85% of a radiation length of matter. (This includes a small (less than 2%) correction, evaluated by Monte Carlo, to take account of the off mass shell Dalitz decays.) Thus, this background can also be subtracted precisely.

(An important point is that other sources of electrons and gammas, such as

$$\eta^o \to \gamma\gamma \text{ and } \eta^o \to e^+e^-\gamma$$

are automatically subtracted by this procedure as long as they have the same branching ratio of internal to external conversions as do π^o Dalitz decays: This is because the slope upon which this subtraction is based includes external conversions of γ's from such a source as well as from π^o's. Thus, these sources cause only a second order correction to the direct lepton signal due to a difference in branching ratio. For example, even if η^o's are produced as copiously as π^o's, this gives only a 10% correction to the directly produced electron signal (see Table VIII). Of course, such sources are more important in using the conversion electron spectrum to deduce the π^o spectrum, as described in Sec. V.B below.)

The result of these subtractions is the clear existence of the directly produced electron signal shown in Fig. 25. The significance of this result is discussed in Sec. V.A

below. Note that by comparing the size of the direct signal with the slope of the foil thickness plot, we obtain an immediate comparison of the size of the direct electron signal to π^o production, with no need for any normalization, acceptance, or efficiency calculations.

A large number of checks was made to verify the existence of this signal and the magnitude of the conversion electron spectrum. These included:

1. Filling the target box with air instead of helium. This produced an additional yield of electrons of just the amount expected from gamma conversions in the 18 ft of air.

2. Tracing electron events backwards through the magnet (using energy deposit in the lead glass as a measure of the particle's momentum) to check for possible sources of electrons other than the target. This method easily detected a foil inserted only a small distance into the aperture. Under normal running conditions, no sources were found.

3. Moving the target to increase the illumination of the collimator walls. This produced no increase in the signal.

4. Varying the intensity of the incident proton beam by a factor of 10. This produced no change in the results.

5. Reanalyzing the data with different fiducial cuts, electron cuts, and reconstruction methods. None of these affected the results.

C. Absolute Normalization

The following factors were evaluated in order to convert the observed yield of conversion and directly produced electrons into absolute cross sections for π^o and electron production:

1. Acceptance of the apparatus as a function of $p_\perp$ and θ.

2. Triggering efficiency, as a function of momentum, for the different elements of the trigger, including:

   a. T0*TM*T1 efficiency,

   b. Hodoscope efficiency,

   c. ϵ_{12} (lead glass electron threshold) efficiency.

3. Reconstruction efficiency.

4. Cut efficiency.

5. Number of protons interacting in the target.

6. Correction from the observed cross section using a beryllium target to a cross section per nucleon.

Considering these in more detail:

1. Acceptance--The geometric acceptance of the apparatus is quite straightforward. The apparatus subtends a specific angle in the lab and a specific range of momentum, depending on the magnet current (with low momentum particles being swept above the detector and high momentum particles passing below). Certain regions are excluded by the fiducial cuts. A small complication is the necessity of taking the energy resolution of the apparatus into account (since we are

measuring a steeply falling spectrum, the effect of a finite energy resolution is to shift the spectrum towards higher momentum, and this must be corrected for). The acceptance is evaluated by a simple Monte Carlo program, and is shown in Fig. 5 as a function of transverse momentum for two different magnet currents.

2. Trigger efficiency--This is evaluated by taking special runs with various elements removed from the trigger, and determining whether there is any excess of events (over standard triggering conditions) at the end of the analysis. Only ε_{12}, the lead glass electron thresholds, produce a measurable effect; their efficiencies as a function of momentum are given in Fig. 12. The rest of the trigger is $\sim$ 99% efficient, in the sense that there are fewer than 1% excess electron events after analysis of runs with looser triggers.

3. Reconstruction efficiency--This is measured by using runs with no hodoscope requirements in the trigger and determining how many electron-like events in the lead glass are lost because of failure to determine an angle or a momentum in the hodoscopes. (Such a failure can be produced either by extra counters firing, producing an ambiguity that cannot be resolved with our limited amount of redundancy, or by missing counters due to hodoscope inefficiencies.) Examination of the total energy deposit in the lead glass for all electron-like showers show that only $\sim$ 10% of the

events are lost in the reconstruction process, so that the efficiency is 90 $\pm$ 5%.

4. Cut efficiency--This is evaluated by using normalized 2 in. Pb runs to subtract hadrons and produce a relatively pure sample of electron events, which can then be studied to determine the effect of the cuts. (Fiducial cuts are taken into account in the acceptance, so we are concerned here with the electron cuts which separate out electrons from hadrons.) The electron cuts, consisting of E counter and longitudinal shower distribution cuts, are measured to be 75% efficient for electrons, independent of momentum (that is, we lose only 25% of the electrons because of the cuts, while losing a much larger percentage of hadrons, as described in Sec. IV.A.6 above).

5. Number of interacting protons--This is a combination of several known factors: the incident proton beam intensity (measured by SEM's); the targeting efficiency (measured by target sweeps and comparison with a wider target which intercepts the entire beam); and the number of scattering centers in the target (computed from the known length and density of the target). Finally, a correction must be put in for the experimental livetime (typically 85-90%) since we are only interested in protons that interacted while our apparatus was prepared to take data. This is evaluated by scaling various monitors both ungated and gated by the live-time.

6. A dependence--In order to derive a cross section per nucleon from our measured cross section on Be, we must measure the A dependence for high $p_\perp$ events. Figure 26 shows our measurements of this A dependence, using data on beryllium, copper, and tungsten, for charged hadron production as a function of $p_\perp$, compared with measurements made by the Chicago-Princeton group.[22] The A dependence varies with $p_\perp$, and in particular, in our region of 2-4 GeV of $p_\perp$, the cross section varies like $A^{1.1}$ and not at all like $A^{2/3}$ (as the total inelastic cross sections do). Assuming that this A dependence continues down to hydrogen, we normalize our data by dividing by A rather than by $A^{2/3}$.

The combination of these factors results in an overall normalization uncertainty of up to 30%.

V. RESULTS

Although the main results of this work are the observations of π^o and charged hadrons at $\sqrt{s}$ = 23.7 and at 65^o and 93^o in the center of mass system, we first review the other results of the same data on lepton production.

A. Leptons

The major result for leptons is the clear existence of a directly produced lepton signal, as seen in Fig. 25. π^o Dalitz decays have already been subtracted. Table VIII lists other possible sources of the electrons we see; none of these can explain the signal.

In addition, the ratio of electrons to hadrons, which we measure as about 1×10^{-4} at 93 mrad, can be determined directly from the foil thickness plot, by making a direct comparison of the number of directly produced electrons and the number of conversion electrons, which arise from hadron decays. No normalizations are needed to calculate this ratio, and thus we can study the behavior of this lepton signal as a function of charge (electrons vs. positrons), $p_\perp$, and angle in a way free of possible systematic errors.

Figure 27 shows a comparison between the size of the signals for electrons and positrons. No difference is observed, and so the rest of the results are averaged over charge.

Figure 28 shows the size of the direct lepton signal as a function of transverse momentum at two angles, 50 mrad

(about 60° in the center of mass system) and 83 mrad (about 90°). The ratio to hadrons is quite constant with $p_{\perp}$, but there is a systematic difference in the ratio at the two angles (see also Table IX).

Finally, putting in the various factors necessary to get an absolute normalization, we obtain the invariant cross section for direct lepton production

$$p + p \rightarrow e^{\pm} + \text{anything}$$

given in Table X and Fig. 29. Again, the spectra are quite smooth and featureless, with no peaks that would indicate the existence of new particles. Superimposed on the statistical errors given in the tables is an overall systematic uncertainty of $\pm$ 30% due to normalization uncertainties.

These results can be compared with three other recent experiments which have also observed direct lepton production. (See Table XI for a summary of the various experiments.[23-28]) Our group, the Columbia-FNAL collaboration, has also measured direct muon production at 83 mrad at the Fermilab; a Chicago-Princeton group has measured direct muon production at 77 mrad at the Fermilab; and the CCRS group has measured direct electron production at the ISR. All these experiments find a lepton to hadron ratio of about 1×10^{-4}.

The interpretation of the lepton results depends crucially on where the other half of the lepton pair is. The leptons we observe are presumably coming from the decay of some parent state into lepton pairs, but in only observing

one lepton we cannot tell if it gets its high transverse momentum from a high mass parent produced at low $p_\perp$ or a low mass parent produced with high $p_\perp$. In the first case, we could try to predict the lepton spectrum from the production of high mass virtual photons; however, the best current estimates (based on parton models[29]) for virtual photon production give a cross section for leptons an order of magnitude below the observed cross section. In the second case, we could predict the lepton spectrum from the known leptonic decay modes of the vector mesons ρ, ω, and ϕ. However, to explain the observed signal one needs vector meson production at large transverse momentum at a rate four times higher than pion production (see Table XII). The complete explanation of the lepton results must await further experiments which observe lepton pairs. (A more complete discussion and interpretation of the lepton results is given in the Ph.D. thesis of H. Paar.)

B. Hadrons

We obtain results on hadrons at both angles in two ways: on neutral hadron production (π^o) by the observed spectrum of conversion electrons; and on charged hadrons by direct observation.

Figure 30 shows the invariant cross section for production of conversion electrons (for real photons)

$$p + p \rightarrow \gamma + \text{anything}$$
$$\hookrightarrow e^+e^-$$

in 1% of a radiation length. If we assume that all these

photons come from π^o decays, we can compute the spectrum for π^o production, either by a Sternheimer differentiation[30] of the electron cross section, or by fitting the electron spectrum iteratively with a Monte Carlo program of π^o decays. This gives the π^o invariant cross sections

$$p + p \rightarrow \pi^o + \text{anything}$$

shown in Fig. 31 (see also Table XIII).

Two important qualifications of this π^o cross section must be made. First, the conversion electron spectrum is insensitive to structure in the π^o spectrum since we are only observing a fraction of the energy of the π^o in an effectively four-body decay ($\pi^o \rightarrow e^+e^-e^+e^-$). (Figure 32 illustrates the spectrum of conversion electrons that would arise from a π^o spectrum with a sharp peak; there is very little evidence of a peak in the electron spectrum.) Thus our π^o spectrum is averaged over any structure which may exist in the actual spectrum.

Second, recent observations of η^o production at high $p_\perp$[31] show that the ratio of η^o to π^o production at high $p_\perp$ is about 1:2. This measurement, together with the 35% branching ratio for $\eta^o \rightarrow \gamma\gamma$, means that about 15% of the conversion electrons come from η^o instead of π^o, and thus we have overestimated the π^o cross section by 15%.

We also make a direct determination of the charged hadron spectrum, using the hadron calorimeter to identify hadrons (that is, to reject electrons and muons) and taking the momentum measurement from the magnet-hodoscope system. We do not discriminate among the various hadrons ($\pi^\pm$, $k^\pm$, p,

$\bar{p}$ ...) and so our cross sections are for all charged hadrons (for negative particles, this cross section is expected to be about 80% π^-).[32] These data were taken with the prescaled pion trigger during electron runs, and also during special hadron runs, including runs with different targets to measure the A dependence of the cross section, and with a modified hodoscope trigger to enhance the sensitivity to high $p_\perp$ particles. The invariant cross sections for charged hadron production are given in Fig. 33 and Table XIV.

From these data we can make a comparison of charged and neutral hadron production at high transverse momentum. Figure 35 shows the ratio of negative hadrons to neutral hadrons as a function of $p_\perp$ at 83 mrad. The constancy of this ratio, while the numerator and denominator are both falling by three orders of magnitude, is impressive. One might expect that $\pi^o = 1/2(\pi^+ + \pi^-)$, and since the π^-/π^+ ratio at large $p_\perp$ is measured to be close to 1,[32] this would mean that $\pi^o \approx \pi^-$. The negative hadrons used in Fig. 35 are all negative hadrons, expected to be about 80% π^o with smaller K^- and $\bar{p}$ contributions; while the neutral hadron data include all neutrals which decay into gamma rays, expected to be about 85% π^o with the remainder η^o. Our data show a constant negative to neutral ratio of 1.33, with possible systematic errors of 30% due to normalization uncertainties. The data strongly suggest that charged and neutral hadrons are produced at high $p_\perp$ by the same process.

Angular dependences for both neutral and charged hadrons can be seen in Figs. 31 and 33. Such measurements of angular

dependence can be important in choosing among competing theories for high $p_\perp$ processes, especially in terms of scaling variables. Certain models predict that the cross sections will depend only on s and $x_\perp$ (= $2p_\perp/\sqrt{s}$), and thus predict no angular variations at constant s and $p_\perp$, while others would have the cross sections scale as functions of, for example, x_r (= $2p^*/\sqrt{s}$), and would thus predict variations as a function of angle. Our data show no strong angular dependences (although there is an indication in the neutral data of a different slope vs. $p_\perp$ at the two angles), and thus would tend to favor the first class of models, in agreement with the British-Scandinavia experiment,[33] but in possible conflict with the FNAL-Northern Illinois experiment[34] which found variations in cross section with angle.

For hadrons, there are also the observations of the A dependence of the high $p_\perp$ cross section, given in Fig. 26. These were measured for charged hadrons, since neutral hadrons are measured by detecting electrons and thus require a low Z target. Data were taken for charged hadrons on beryllium, copper, and tungsten targets. The results, in good agreement with the Chicago-Princeton results,[22] show the cross section varying like $A^{1.1}$, showing that the various nucleons are somehow acting coherently to produce high $p_\perp$ hadrons.

Finally, considering the lepton and hadron data together, one is struck by the remarkable constancy of the lepton/hadron ratio, which seems independent of s, $p_\perp$, charge, lepton number, and target nucleus. This implies that the leptons are being produced hadronically, either in the same manner as the

hadrons or perhaps by decay of particular hadronic states, but the exact mechanism for lepton production remains a mystery.

In summary, the major results of this experiment for high transverse momentum hadron production are the following:

1. Verification of the copious yield of hadrons at high $p_\perp$;

2. Direct comparison of charged and neutral hadron production, measured with the same apparatus, showing no significant differences between the two (see Fig. 35);

3. Measurement of both charged and neutral hadrons at different angles, showing no strong angular dependence;

4. Measurement of the A dependence of high $p_\perp$ hadron production, showing that this part of the cross section varies like A to the first power rather than like $A^{2/3}$.

A comparison with other experiments on both neutral and charged hadron production is shown in Fig. 34. The solid line a is our π^o cross section measured at 83 mrad (90^o in the center of mass system), and the points c are our data for negative hadron production, also at 83 mrad (both measured at 300 GeV on beryllium). The dotted line b is a fit to the π^o data of the CERN-Columbia-Rockefeller collaboration,[35] modified to fit smoothly at moderate $p_\perp$:

$$E\frac{d^3\sigma}{dp^3} = \frac{15\ \text{mb}}{(p_\perp^2+1)^4} e^{-13x_\perp}, \quad x_\perp = \frac{2p_\perp}{\sqrt{s}}$$

and the points d are the average of the π^+ and π^- cross

sections measured by the Chicago-Princeton group at Fermilab.[32] The agreement among these experiments, and between the charged and neutral data, is excellent, both in slope as a function of $p_\perp$ and in absolute normalization.

A chart of the various high transverse momentum hadron experiments is given in Table XV, showing the energies, angles, $p_\perp$ ranges, and major results of each.[22,32-40] The significance of these results is discussed in Sec. VI below.

VI. THEORY AND CONCLUSIONS

A successful model for high transverse momentum phenomena must be able to account for each of the following classes of experimental observations:

1. Copious yield of hadrons--why is there such an abundant production of hadrons at high $p_\perp$, when the strong interactions otherwise seem to be characterized by rapid exponential damping with increasing $p_\perp$;

2. Single particle inclusive cross sections, as a function of s, $p_\perp$, and θ, and in particular, the existence of scaling in certain variables;

3. Particle composition at high $p_\perp$, including the ratios for various hadrons as well as direct lepton production;

4. Correlations, or what else happens when a particle is produced at high $p_\perp$; and

5. Nuclear effects--why the high $p_\perp$ cross section depends on A rather than $A^{2/3}$.

Summarizing the experimental information in each of these categories:

1) Copious yield: All experiments (see Table XV) agree in finding a yield of hadrons far above that expected from the formula

$$E \frac{d^3\sigma}{dp^3} = 1.2 \times 10^{-25} e^{-6p_\perp} \left(\frac{cm^2}{GeV^2}\right)$$

which fits the data at lower $p_\perp$. The difference between the data and the low $p_\perp$ fit is five orders of magnitude at a

transverse momentum of 5 GeV. The agreement among the various experiments is excellent at the level of the various uncertainties (typically 50%).

2) Single particle inclusive cross sections: The various experiments measure cross sections over a wide range of s, $p_\perp$ and θ. The most striking experimental results include the clear energy dependence of the cross section for fixed $p_\perp$, shown for example in the Chicago-Princeton, CCR and Saclay-Strasbourg data (contrary to the case at low $p_\perp$, where the cross section at fixed $p_\perp$ is virtually independent of s, the high $p_\perp$ experiments show a rise at fixed $p_\perp$, with increasing s), and the lack of any strong angular dependence, shown in the British-Scandinavia and Columbia-Fermilab data. Also important is scaling behavior: If we define the scaling variable $x_\perp = 2p_\perp/\sqrt{s}$ then at large $x_\perp$, the cross sections can be fit by a scaling function

$$E \frac{d^3\sigma}{dp^3} \propto \frac{1}{p_\perp^n} f(x_\perp) \quad .$$

For example, the Chicago-Princeton data for $x_\perp > 0.4$ are fit by

$$E \frac{d^3\sigma}{dp^3} \propto \frac{1}{s^{5.5}} e^{-36.0\, x_\perp} \quad .$$

3) Particle composition: Data from the British-Scandinavia and Chicago-Princeton experiments show a sharp increase in heavy particle (K^+, K^-, p, $\bar{p}$) production between $p_\perp = 0.2$ GeV (where the charged particles are 90% pions and

positive and negative particles are produced equally), and $p_\perp$ = 1.5 GeV (where there are fewer than 65% pions and positive particles are more abundant than negative). The heavy particle fraction remains roughly constant between 1.5 and 3.5 GeV, but the C-P data show the K^-/π^- and $\bar{p}/\pi^-$ ratios dropping at higher $p_\perp$. Some s dependence is also present, especially in the p/π^+ ratio, which falls with increasing s. (Some of these effects may depend on the target, since there are some differences between beryllium and tungsten data, and may be clarified by future Fermilab experiments with hydrogen targets.)

Moreover, there is the question of the directly produced lepton signal, observed in several experiments (see Table XI). The leptons appear to arise from the same source as the hadrons, since lepton/hadron ratios seem independent of s, $p_\perp$, and target.

4) Correlations: Most data on correlations taken up to now deal with the charged particle multiplicities in various directions associated with the production of a high $p_\perp$ π^o at 90^o. The Pisa-Stony Brook and ACHM experiments show that the total charged multiplicity increases with $p_\perp$ (although less rapidly at lower s). Considering the partial multiplicities in different regions, they find a decrease in the multiplicity in the forward and backward directions, and an increase in a broad region (extending over 100^o in both θ and ϕ) opposite the high $p_\perp$ π^o, while there is very little $p_\perp$ dependence of the multiplicity in the region around the high $p_\perp$ π^o. The ACHM group also looks at correlations

of pairs of particles associated with the high $p_\perp$ π^o, but finds no $p_\perp$ dependence in these correlations.

More recent measurements by both groups have been made with the high $p_\perp$ particle at an angle other than 90^o, showing similar behavior. In particular, the large $p_\perp$ is balanced over the entire range in rapidity (i.e., the increase in multiplicity at $\phi = 180^o$ with respect to the high $p_\perp$ π^o is distributed over all θ). And in the only measurements with information on the momentum of the additional particles, the CCR group has found strong positive correlations between two high $p_\perp$ π^o's on opposite sides.

5) Nuclear effects: The Columbia-Fermilab and Chicago-Princeton data agree on A^N dependence, with N = 1.0-1.1.

There are two basic types of theoretical models which attempt to explain these facts, arising from two different answers to the question of where the particles get their large transverse momenta. These are fireball and hard scattering models.[41]

Fireball models assume that the large longitudinal momentum present in a high energy collision is first transferred into the creation of a high mass virtual hadronic state, or fireball. High $p_\perp$ particles are then produced by the decays of this fireball. In this case, high $p_\perp$ physics is studying the primordial state of hadronic matter (or alternatively, the mass spectrum of a new set of hadronic resonances).

Hard scattering models postulate the existence of point-like constituents (often "partons" or quarks) within the colliding particles. The high $p_\perp$ particles are produced by the form factor free interactions of these point-like objects (which can thus produce wide angle scatters). In these models, high $p_\perp$ physics is studying the constituents of the hadrons.

Both classes of models are consistent with the general experimental features, without necessarily being able to account for all specific details. The two classes of models do differ fundamentally in their predictions of correlations: Fireball models tend to predict an isotropic distribution of particles, subject only to energy and momentum conservation (since the distributions are determined solely by the evolution and decay of the fireball); while hard scattering models lead to very few particles outside the plane of the high $p_\perp$ scatter (since the process is a two-body coplanar scattering process), and to predict two jetlike cones of particles on opposite sides, resulting from the "decay" of the two scattered "partons" into physical hadrons.

Of course, the experimental question is considerably muddied by the difficulty in distinguishing those particles which are actual participants in the high $p_\perp$ process from all the rest of the hadrons produced in the same collision. Present data, while perhaps favoring scattering models, cannot rule out sophisticated fireball models. (For example,

the CCR data on $\pi^o\pi^o$ correlations are reasonably consistent with both a particular parton model and with the uncorrelated jet model,[42] which takes only energy and momentum conservation into account.) Both further theoretical examinations of the difference between kinematical and dynamical effects on correlations, and further experimental measurements are needed to settle the question of which type of model is more realistic.

Some of the theoretical problems are illustrated by considering a few specific parton models, which have been worked out in more detail than fireball models. The most naive models, reasoning (by analogy with models which so successfully fit the data on deep inelastic lepton scattering) from dimensional analysis and the absence of any scale in an inclusive reaction, predict that inclusive cross sections should vary as:

$$E\frac{d^3\sigma}{dp^3} \propto \frac{1}{p_\perp^n} f(x_\perp) \quad \text{with } n = 4 \quad .$$

Since the data demand $n = 8$ in the $x_\perp$ region covered by the ISR and $n = 11$ at the higher $x_\perp$ of the Chicago-Princeton experiment, the models must somehow introduce a scale or form factor of some sort to account for this discrepancy.

One solution to this problem is the constituent interchange model,[43] which makes the basic process not quark-quark scattering, but quark-pion scattering, which, due to the pion form factor, gives $n = 8$. Consideration of additional

types of elementary scattering processes leads to a sum of terms which can be fit to the C-P data giving n = 11. (This model can also account for exclusive and small $p_\perp$ reactions.)

Other solutions involve other ways of introducing a scale. These include quasi-exclusive parton models,[44] where an assumed resonant structure near y = 1 in G(y), the distribution of hadrons within the scattered parton, introduces an effective form factor and yields a combination of n = 4 and n = 8 terms; and covariant parton models,[4] where a scale can be introduced in the dynamics of the process of the recombination of partons to form hadrons. Specific parton models can also account for particle ratios, by identifying partons with valence quarks within the hadrons, and for the general type of positive correlations so far observed, based on jetlike structures.

In summary, the hard-scattering parton-type models are able to account for many of the qualitative features of high $p_\perp$ hadron physics. However, the simple models which are so successful in describing deep inelastic lepton scattering are not sufficient; various complications must be introduced. Moreover, the data cannot yet rule out fireball models. Further experiments, including high $x_\perp$ experiments using pion beams and hydrogen targets at Fermilab, additional correlation experiments which measure momentum distributions as well as multiplicities and trigger on high $p_\perp$ particles

away from 90^{o}, and measurement of dilepton production, which could provide a direct link to deep inelastic processes, are needed before we can hope to fully understand what is happening at high transverse momenta. Nevertheless, the field has made enormous progress since the copious hadron yield was first discovered at the ISR less than three years ago.

Finally, the newly discovered resonances at 3.1 and 3.7 GeV must be considered. Could they in fact be the first of a family of massive "fireballs" responsible for high $p_{\perp}$ hadron and lepton production? Possibly they could be, but this would require a rather complex and artificial model for the production of these new particles, since the lack of any resonant structure in the high $p_{\perp}$ data and the complexity of, for instance, the particle ratios, would tend to rule out any simple model for producing all high $p_{\perp}$ particles from the decays of these new resonances. But the data cannot yet exclude the possibility that all hadrons and leptons with $p_{\perp} \geq 2$ GeV arise from decays of so far undiscovered particles.[7]

So, many of the basic experimental and theoretical questions of high transverse momentum physics remain unanswered. The solutions, which will hopefully emerge with the completion of the new generation of experiments now planned or underway, should tell us a great deal about the basic structure and interactions of the hadrons.

ACKNOWLEDGMENTS

Like any contemporary high energy physics experiment, this research required the efforts of a large number of people. To list their contributions individually would require a document comparable in length to the rest of this thesis, and so I am forced to thank them for their contributions to the success of this experiment in groups.

First, there is the staff of Nevis Labs: engineers who designed the apparatus, technicians who built it, and the other physicists, both experimenters and theorists, who were always available for helpful discussions.

Next, the staff of the Fermi National Accelerator Laboratory, where we ran our experiment. Without the many people who built the accelerator and keep it running, our apparatus would have had nothing to measure. This is especially true of the members of the Proton Lab, who were most immediately involved in servicing our requests and listening to our complaints.

Next, there are my collaborators, from Columbia and from Fermilab: Jeff Appel, Maurice Bourquin, Bruce Brown, Jean-Marc Gaillard, Dave Hom, Hans Paar, Jean-Paul Repellin, Dave Saxon, Dave Snyder, Jeff Weiss, Taiji Yamanouchi, and John Yoh. Each brought his own viewpoint and style to the experiment, and I was fortunate in being able to work closely with them during the course of the experiment.

Finally, there is my sponsor, Leon Lederman. He not only taught me the mechanics of doing research, but also showed me its excitement. His constant infusion of new ideas guaranteed that our experimental trailer was always a stimulating place to work.

And special thanks to Ann Therrien, who typed this thesis.

Table I

Experimental Geometry

Apparatus	Distance From Target	Aperture (Inches)	Aperture (mrad)
Target Box	0 - 20 ft		
Precision Collimator	23 ft 5 in. - 35 ft 2 in.	2.529 in. X 2.529 in. 3.818 in. X 3.818 in.	9.05 mr X 9.05 mrad
Semi-Precision Collimator	36 ft 5 in. - 51 ft 2 in.	4.151 in. X 4.151 in. 5.833 in. X 5.833 in.	9.50 mr X 9.50 mrad
Magnet 1	52 ft - 62 ft	10 in. X 7-1/4 in.	9.74 mrad
Magnet 2	62 ft 5 in. - 72 ft 5 in.	10 in. X 8-1/2 in.	9.78 mrad
Hodoscopes (H1,V1,U)	120 ft	20-1/2 in. X 20-1/2 in.	14.2 mrad
Hodoscopes (M)	150 ft	24 in. X 24 in.	13.3 mrad
Hodoscopes (H2,V2)	180 ft	27-1/2 in. X 27-1/2 in.	12.7 mrad
Lead Glass	180 ft	30 in. X 30 in.	
Hadron Detector	190 ft	36 in. X 36 in.	

Table II

Material In Beam Line (83 m rad)

Material	Length	Rad. Length of Material	Rad. Lengths
Target: Be (1/2 X .0088 in. viewed at 83 m rad)	0.052 in.	35.7 cm	0.37%
Target Box: He	18 ft	521 k cm	0.11%
0.2% air contamination	18 ft	30.87 k cm	0.004%
Window - Exit Target Box: Kapton	0.005 in.	35 cm	0.036%
Air Gap: Air	16 in.	30.87 k cm	0.13%
Window: Collimator Entrance: Kapton	0.005 in.	35 cm	0.036%
"Vacuum" in Collimator: 4 mm Air	35 ft	30.87 X 760/4 k cm	0.018%
Window: Collimator Exit: Kapton	0.005 in.	35 cm	0.036%
		Total	0.74%

Table III

Trigger Counters And Hodoscopes

Trigger Counter	Distance From Target	Size Of Individual Counters	Number Of Counters	Total Aperture
TØ	120 ft	22 in. X 15 in. X 1/8 in.	1	22 in. X 15 in.
TM	150 ft	24 in. X 18-1/2 in. X 1/8 in.	2	24 in. X 24 in.
T1	180 ft	30 in. X 10 in. X 1/4 in.	2	30 in. X 20 in.
T2	180 ft	30 in. X 7 in. X 1/8 in.	4	30 in. X 28 in.
D	180 ft	10 in. X 24 in. X 1/4 in.	3	28 in. X 24 in.
E	180 ft	8-1/2 in. X 20 in. X 1/4 in.	3	24-1/2 in. X 20 in.

Hodoscope	Distance From Target	Material	Size Of Individual Counter	Number Of Counters	Total Aperture
H1	120 ft	Pilot Y	3/4 in. X 20-1/2 in. X 1/8 in.	40	20-1/2 in. X 20-1/2 in.
V1	120 ft	Pilot Y	20-1/2 in. X 3/4 in. X 1/8 in.	40	20-1/2 in. X 20-1/2 in.
U	120 ft	Pilot Y	various X 4.2 in. X 1/8 in.	10	20-1/2 in. X 20-1/2 in.
M	150 ft	Nuclear Enterprise 110	3 in. X 24 in. X 1/8 in.	12	24 in. X 24 in.
H2	180 ft	Pilot Y	3/4 in. X 27-1/2 in. X 1/8 in.	54	27-1/2 in. X 27-1/2 in.

Table III (cont'd)

Hodoscope	Distance From Target	Material	Size Of Individual Counter	Number Of Counters	Total Aperture
V2	180 ft	Pilot Y	27-1/2 in. X 3/4 in. X 1/8 in.	54	27-1/2 in. X 27-1/2 in.
Mu Picket	200 ft	NE 110	2 in. X 30 in. X 1/4 in.	16	32 in. X 30 in.

Dimensions are vertical X horizontal X thickness.

Table IV

Properties Of Lead Glass

Type: SF5

Composition (by weight): 55% PbO
38% SiO_2
5% K_2O
1% Na_2O

Radiation Length 2.54 cm
Refraction Index 1.67270
Specific Gravity 4.08
Thermal Expansion Coefficient 85×10^{-7} (-30° to $+ 70^{\circ}$ C.)
Internal Transmission of 25 mm thickness.

λ (Angstroms)	Transmission	λ	Trans.
3400	2%	4000	95%
3500	27%	4200	97.5%
3600	57%	4400	98%
3700	75%	5000	99%
3800	85%	7000	99.3%
3900	92%		

Table V

Information Gated Into Register Logic
By A Fast Trigger

Hodoscopes

40 bits	H1	Counters
40 bits	V1	Counters
10 bits	U	Counters
12 bits	M	Counters
54 bits	H2	Counters
54 bits	V2	Counters
16 bits	Mu Picket	Counters

Each bit that is on generates an address to be transmitted to the computer.

12 bits	πe	Counters
2 bits	TM	Counters
2 bits	T1	Counters
1 bit	fast " e " trigger	
1 bit	fast π trigger	
1 bit	fast random trigger	
1 bit	beam gate	
3 bits	Pb glass electron thresholds:	
	ϵ_{12}^{L}	
	ϵ_{12}^{M}	
	ϵ_{12}^{H}	

These data are recorded as bits.

Table VI

Logic Bus

Bit	Triggers					Monitors							
	E_L	E_M	E_H	Super π	Rand	E	E6/6	E5/6		π	π6/6	μ	μ6/6
2 $\bar{e}$ π				X									
3 5/6 Hodoscopes								X					
4 T0.T1.TM.T2 (Fast "e")	X	X	X			X	X	X	X				
5 Beam Gate	X	X	X	X	X	X	X	X	X	X	X	X	X
6 Target Monitor * Rand Pre-Scaler (Fast Rand)					X								
7 μ P												X	X
8 T0.T1.Tm * π Pre-Scaler (Fast "π")				X						X	X	X	X
9 ϵ_{12}M Un-Prescaled													
10 6/6 Hodoscopes	X	X	X	X			X		X		X		X
11 ϵ_{12} L * Pre-Scaler	X												
12 ϵ_{12} M * Pre-Scaler		X											
13 ϵ_{12} H			X										
14 $\bar{\pi}$ e	X	X	X						X				

Table VII

Typical Fiducial Cuts

$-4.2 \text{ mrad} < \theta_x < 4.2 \text{ mrad}$ $-4.2 \text{ mrad} < \theta_y < 4.2 \text{ mrad}$	Collimator edge
$5 < H2 < 101$ $6 < V2 < 96$	Edges of Pb glass
$V2 < 52$ or $V2 > 59$	Eliminates central crack of Pb glass array
$-4.2 \text{ in.} < YMAG < 5.6 \text{ in.}$	Vertical position at magnet aperture

(H2 and V2 are given in units of 1/4 in. elements)

Cut	Percentage of electron events typically cut	
θx	1.5%	
θy	2%	
H2	0.5%	
V2	0	(Aperture of trigger counters is smaller than this cut)
V2 center	0.5%	
Y MAG	0.5%	

Table VIII

Possible Backgrounds to Directly Produced Electron Signal

(Normalized to π^0 yield)

$1.9 < P_\perp < 4$ GeV/c

Signal (After subtraction of Dalitz pairs)	$\sim 1 \times 10^{-4}$	
Dalitz pairs $\pi^0 \rightarrow \gamma e^+e^-$	1.6×10^{-4}	
$\eta^0 \rightarrow \gamma e^+e^-$	1.5×10^{-5}	a
$\mu^- \rightarrow e^- \nu \bar{\nu}$	10^{-8}	b
$\pi^- \rightarrow e^- \bar{\nu}$	10^{-7}	b
$K^- \rightarrow \pi^0 e^- \bar{\nu}$	3×10^{-6}	b,c
$K_L^0 \rightarrow \pi^+ e^- \bar{\nu}$	2×10^{-6}	b,c
Hyperons	3×10^{-6}	b,d

Notes: a) Assuming equal production of η^0 and π^0.

b) Only decays upstream of the 2 in. of Pb (7 m decay path) need be considered, as decays downstream of the Pb are automatically subtracted from the signal as hadron feedthrough.

c) Assuming K/π production ratio as measured in ref. 32.

d) Assuming equal production of hyperons and π^0.

Table IX

Direct Lepton/Hadron Ratio

$P_\perp$	Normalized to $\pi^o \times 10^{-4}$		Normalized to Dalitz Pairs	
	50 mrad	83 mrad	50 mrad	83 mrad
1.6 - 1.8				
1.8 - 2.0	1.62		$.62 \pm .14$	
2.0 - 2.2	1.70	1.02	$.77 \pm .13$	$.46 \pm .06$
2.2 - 2.4	0.92	0.90	$.47 \pm .13$	$.46 \pm .06$
2.4 - 2.6	2.42	0.95	$1.40 \pm .22$	$.55 \pm .08$
2.6 - 2.8	0.92	0.73	$.58 \pm .20$	$.46 \pm .09$
2.8 - 3.0	2.29	0.83	$1.58 \pm .28$	$.57 \pm .11$
3.0 - 3.2	1.32	1.06	$1.00 \pm .29$	$.80 \pm .13$
3.2 - 3.4	2.33	1.10	$1.93 \pm .52$	$.91 \pm .19$
3.4 - 3.6	0.45	0.71	$.40 \pm .36$	$.64 \pm .21$
3.6 - 3.8		0.45		$.43 \pm .30$
3.8 - 4.0				

Table X

Invariant Cross Section For Direct

Electron Production

$$E\frac{d^3\sigma}{dp^3}\ \left(\frac{cm^2}{GeV^2}\right) \qquad P + N \rightarrow e_{Direct} + \text{anything}$$

$P_\perp$	50 mrad	83 mrad
1.8 - 2.0	$(2.00 \pm 0.45) \times 10^{-33}$	
2.0 - 2.2	$(6.18 \pm 1.04) \times 10^{-34}$	$(2.14 \pm 0.28) \times 10^{-34}$
2.2 - 2.4	$(1.47 \pm 0.41) \times 10^{-34}$	$(7.99 \pm 1.04) \times 10^{-35}$
2.4 - 2.6	$(1.42 \pm 0.22) \times 10^{-34}$	$(4.40 \pm 0.64) \times 10^{-35}$
2.6 - 2.8	$(3.42 \pm 1.18) \times 10^{-35}$	$(1.57 \pm 0.31) \times 10^{-35}$
2.8 - 3.0	$(3.37 \pm 0.60) \times 10^{-35}$	$(8.33 \pm 1.61) \times 10^{-36}$
3.0 - 3.2	$(8.46 \pm 2.45) \times 10^{-36}$	$(5.17 \pm 0.84) \times 10^{-36}$
3.2 - 3.4	$(5.39 \pm 1.45) \times 10^{-36}$	$(2.52 \pm 0.53) \times 10^{-36}$
3.4 - 3.6	$(7.02 \pm 6.32) \times 10^{-37}$	$(8.53 \pm 2.80) \times 10^{-37}$
3.6 - 3.8		$(2.61 \pm 1.82) \times 10^{-37}$

Errors are statistical only

Table XI

High $P_\perp$ Lepton Experiments

Experiment	Ref.	At	Lab Energy/$\sqrt{s}$ C-M Energy	θ C-M Angle	$P_\perp$ (GeV) Transverse Momentum	Lepton/ Hadron	Particle
Columbia - Fermilab	23	FNAL	300 GeV / 23.8	65^o 93^o	1.8 - 4.0	1.6×10^{-4} 1.0×10^{-4}	e
Columbia - Fermilab	23	FNAL	300 GeV / 23.8	93^o	2.0 - 4.0	1×10^{-4}	μ
Chicago - Princeton	24	FNAL	300 GeV / 23.8	90^o	1.5 - 5.4	0.8×10^{-4}	μ
Cern - Columbia - Rockefeller - Saclay	25	ISR	/ 52.7	90^o	1.6 - 4.7	1.2×10^{-4}	e
Chicago - Harvard - Penn. Wisconsin	26	FNAL	30 - 300 GeV	(85 mrad in lab)	.85 - 2.1	0.09×10^{-4} - 1.4×10^{-4}	μ
B.N.L. - Yale Fermilab - Wisconsin	27	BNL	28 Gev	Forward	P = 11.6 25 GeV	1.3×10^{-4} - 7.0×10^{-6}	μ
	28	Serpukhov	70 GeV / 12	90^o	1.8 - 2.8 GeV	2.5×10^{-5}	μ

Table XII

Possible Sources Of Direct Leptons

$\langle p_\perp \rangle \sim 3$ GeV/c	Normalized to π^o Production
Signal	$\sim 1 \times 10^{-4}$
Vector Meson Decay[a]	
$\rho^o \rightarrow \ell^+\ell^-$	5×10^{-6}
$\phi^o \rightarrow \ell^+\ell^-$	3×10^{-5}
$\omega^o \rightarrow \ell^+\ell^-$	7×10^{-6}
Parton Antiparton Annihilation	
$q\bar{q} \rightarrow \ell^+\ell^-$	$\sim 5 \times 10^{-6}$

a) Assuming $N_\rho = N_\phi = N_\omega = N_{\pi^o}$

Table XIII

Invariant Cross Section For Conversion

Electrons And π^o Production

$P_\perp$	$E\frac{d^3\sigma}{dp^3}\left(\frac{cm^2}{GeV^2}\right)$ for $p+N \rightarrow \gamma+\text{anything}$ $\hookrightarrow e^+e^-$ (1% rad. length)		$E\frac{d^3\sigma}{dp^3}\left(\frac{cm^2}{GeV^2}\right)$ for $p+N \rightarrow \pi^o+\text{anything}$	
	50 mrad	83 mrad	50 mrad	83 mrad
1.6 - 1.8				
1.8 - 2.0				
2.0 - 2.2	$9.43 \pm .28 \times 10^{-34}$	$5.46 \pm .096 \times 10^{-34}$	3.63×10^{-30}	2.10×10^{-30}
2.2 - 2.4	$3.65 \pm .12 \times 10^{-34}$	$2.04 \pm .034 \times 10^{-34}$	1.59×10^{-30}	8.91×10^{-31}
2.4 - 2.6	$1.20 \pm .059 \times 10^{-34}$	$9.46 \pm .17 \times 10^{-35}$	5.86×10^{-31}	4.64×10^{-31}
2.6 - 2.8	$6.91 \pm .31 \times 10^{-35}$	$4.03 \pm .085 \times 10^{-35}$	3.70×10^{-31}	2.15×10^{-31}
2.8 - 3.0	$2.51 \pm .13 \times 10^{-35}$	$1.73 \pm .044 \times 10^{-35}$	1.47×10^{-31}	1.01×10^{-31}
3.0 - 3.2	$9.97 \pm .58 \times 10^{-36}$	$7.66 \pm .24 \times 10^{-36}$	6.38×10^{-32}	4.90×10^{-32}

Table XIII (cont'd)

Invariant Cross Section For Conversion

Electrons And π^o Production

$P_\perp$	50 mrad	83 mrad	50 mrad	83 mrad
3.2 - 3.4	$3.28 \pm .30 \times 10^{-36}$	$3.24 \pm .14 \times 10^{-36}$	2.32×10^{-32}	2.29×10^{-32}
3.4 - 3.6	$2.06 \pm .17 \times 10^{-36}$	$1.58 \pm .079 \times 10^{-36}$	1.58×10^{-32}	1.21×10^{-32}
3.6 - 3.8	$8.13 \pm 1.00 \times 10^{-37}$	$7.14 \pm .50 \times 10^{-37}$	6.68×10^{-33}	5.87×10^{-33}
3.8 - 4.0	$1.63 \pm .49 \times 10^{-37}$	$3.83 \pm .36 \times 10^{-37}$	1.45×10^{-33}	3.41×10^{-33}
4.0 - 4.2	$6.08 \pm 3.81 \times 10^{-38}$	$5.84 \pm 1.82 \times 10^{-38}$	5.84×10^{-34}	5.61×10^{-34}
4.2 - 4.4		$8.19 \pm 1.47 \times 10^{-38}$		8.42×10^{-34}

Table XIV

Invariant Cross Section For
Charged Hadron Production

$$E\frac{d^3\sigma}{dp^3}\left(\frac{cm^2}{GeV^2}\right) \qquad P + N \rightarrow h^- + \text{anything}$$

$P_\perp$	50 mrad	83 mrad
1.8 - 2.0		$5.09 \pm .047 \times 10^{-30}$
2.0 - 2.2		$2.53 \pm .025 \times 10^{-30}$
2.2 - 2.4		$1.31 \pm .016 \times 10^{-30}$
2.4 - 2.6		$5.84 \pm .10 \times 10^{-31}$
2.6 - 2.8		$3.04 \pm .072 \times 10^{-31}$
2.8 - 3.0	$1.10 \pm .065 \times 10^{-31}$	$1.21 \pm .010 \times 10^{-31}$
3.0 - 3.2	$5.15 \pm .39 \times 10^{-32}$	$6.56 \pm .059 \times 10^{-32}$
3.2 - 3.4	$2.66 \pm .18 \times 10^{-32}$	$3.27 \pm .038 \times 10^{-32}$
3.4 - 3.6	$1.25 \pm .11 \times 10^{-32}$	$1.62 \pm .024 \times 10^{-32}$
3.6 - 3.8	$5.54 \pm .63 \times 10^{-33}$	$8.18 \pm .17 \times 10^{-33}$
3.8 - 4.0	$3.39 \pm .46 \times 10^{-33}$	$4.46 \pm .12 \times 10^{-33}$
4.0 - 4.2	$1.51 \pm .29 \times 10^{-33}$	$2.14 \pm .08 \times 10^{-33}$
4.2 - 4.4	$9.7 \pm 2.8 \times 10^{-34}$	$1.26 \pm .06 \times 10^{-33}$
4.4 - 4.6	$4.5 \pm 1.8 \times 10^{-34}$	$5.88 \pm .41 \times 10^{-34}$
4.6 - 4.8		$3.17 \pm .29 \times 10^{-34}$
4.8 - 5.0		$1.28 \pm .18 \times 10^{-34}$

Table XV

High $P_\perp$ Hadron Experiments

Experiment	Ref.	At	Reaction	C-M Energy (GeV)	$P_\perp$ (GeV)	C-M θ	Major Results
Cern - Columbia Rockefeller (CCR)	35, 36	ISR	π^o + anything $\pi^o\pi^o$ + anything	23.5 - 62.4	2.6 - 9.0	$90^o \pm 30$	Single particle inclusive correlations
Saclay Strasbourg	37	ISR	$X^{\pm}$ $\pi^{\pm}$ + anything γ	23.2 - 52.7	1.0 - 5.0	90^o	Single particle inclusive
British - Scandinavia	33	ISR	$X^{\pm}$ $\pi^{\pm}$ + anything $k^{\pm}$ $p,\bar{p}$	44, 53	1.3 - 5.0	59^o, 90^o	Single particle inclusive angular dependence particle ratios
Chicago - Princeton	22 32	FNAL	$\pi^{\pm}$ $k^{\pm}$ $p,\bar{p}$ + anything	19.4, 23.8	0.8 - 7.6	90^o	Single particle inclusive particle ratios nuclear effects
Fermilab - Northern Illinois	34	FNAL	γ + anything	9.8 - 27.4	0.3 - 4.3	40^o 110^o	Single particle inclusive angular dependence

Table XV (cont'd)

High $P_\perp$ Hadron Experiments

Experiment	Ref.	At	Reaction	C-M Energy (GeV)	$P_\perp$ (GeV)	C-M θ	Major Results
Columbia Fermilab	38	FNAL	π^o $X^\pm$ + anything	23.8	1.6 - 5.0	65^o, 93^o	Single particle inclusive angular dependence nuclear effects
Pisa Stonybrook	39	ISR	π^o + anything	23 - 62	0 - 4.5	90^o 17.5^o	Correlations
Aachen - Cern Heidelberg - Munich (ACHM)	40	ISR	π^o + anything	44 53	0 - 4	90^o 60^o	Single particle inclusive correlations

References

[1] G. Cocconi, Nuovo Cimento 57A, 837 (1968).
K. Imaeda, Nuovo Cimento 48A, 482 (1967).

[2] S.M. Berman, J.D. Bjorken, J.B. Kogut, Phys. Rev. D4, 3388 (1971).

[3] Constituent interchange models: R. Blackenbecler, S.J. Brodsky, J.F. Gunion, Phys. Lett. 39B, 649 (1972); Phys. Rev. D6, 2652 (1972); Phys. Lett. 42B, 461 (1973); Phys. Rev. D8, 287 (1973).

[4] Covariant parton models: P.V. Landshoff, J.C. Polkinghorne, Phys. Lett. 45B, 361 (1973); Phys. Rev. D8, 4159 (1974).

[5] Parton models: D. Cline, F. Halzen, H. Waldrop, Nucl. Phys. B55, 157 (1973); S.D. Ellis, M.B. Kislinger, Preprint NAL-PUB-73/40 THY(1973) to be published in Phys. Rev. D9, 2027 (1974).

[6] Statistical Models: S. Pokorski, L. VanHove, CERN Preprint TH 1772 (1973); Nucl. Phys. B60, 379 (1973); R. Hagedorn, I. Montvay, Nucl. Phys. B59, 45 (1973); S. Frautschi, Phys. Rev. D3, 2821 (1971); P. Carruthers, Minh Duong-Van, Phys. Rev. Lett. 31, 133 (1973).

[7] L.M. Lederman, Informal Conference on Theoretical Physics, Rutherford Labs (1975).

[8] E.D. Bloom, D.H. Coward, H. DeStaebler, J. Drees, G. Miller, L.W. Mo, R.E. Taylor, M. Breidenbach, J.I. Friedman, G.C. Hartmann, H.W. Kendall, Phys. Rev. Lett. 23, 930 (1969);

[8] M. Breidenbach, J.I. Friedman, H.W. Kendall, E.D. Bloom, D.H. Coward, H. DeStaebler, J. Drees, L.W. Mo, R.E. Taylor, Phys. Rev. Lett. 23, 935 (1969).

[9] J.D. Bjorken, Phys. Rev. 179, 1547 (1969).
J.D. Bjorken, E.A. Paschos, Phys. Rev. 185, 1975 (1969).

[10] S.D. Drell, T-M. Yan, Phys. Rev. Lett. 25, 316 (1970); H.P. Paar, E.A. Paschos, Phys. Rev. D10, 1502 (1974); S.D. Ellis, M.B. Kislinger, Phys. Rev. D9, 2027 (1974); G.R. Farrar, Nucl. Phys. B 77, 429 (1974).

[11] A. Litke, G. Hanson, A. Hofmann, J. Koch, L. Law, M.E. Low, J. Leong, R. Little, R. Madaras, H. Newman, J.M. Paterson, R. Pordes, K. Strauch, G. Tarnopolsky, Richard Wilson, Phys. Rev. Lett. 30, 1189 (1973). G. Tarnopolsky, J. Eshelman, M.E. Low, J. Leong, H. Newman, R. Little, K. Strauch, R. Wilson, Phys. Rev. Lett. 32, 432 (1974). B. Richter, Plenary Session Report on e^+e^- Annihilation into Hadrons, London International Conference on High Energy Physics (1974).

[12] The rate of W production can be related to the rate of virtual γ production by CVC arguments: Y. Yamaguchi, Nuovo Cimento XLIII A, 193 (1966). L.M. Lederman, B.G. Pope, Phys. Rev. Lett. 27, 765 (1971). L.M. Lederman, D.H. Saxon, Nucl. Phys. B63, 313 (1973).

[13] T.D. Lee, G.C. Wick, Phys. Rev. D2, 1033 (1970).

[14] Single muon production: R. Burns, G. Danby, E. Hyman, L.M. Lederman, W. Lee, J. Rettberg, J. Sunderland, Phys. Rev. Lett. 15, 830 (1965). R.C. Lamb, R.A. Lundy, T.B. Novey,

[14] D.D. Yovanovitch, M.L. Good, R. Hartung, M.W. Peters, A. Subramanian, Phys. Rev. Lett. 15, 800 (1965).

[15] Dimuon production: J.H. Christenson, G.S. Hicks, L.M. Lederman, P.J. Limon, B.G. Pope, E. Zavattini, Phys. Rev. Lett. 25, 1523 (1970). B.G. Pope, Ph.D. Thesis, Nevis Report 185, Columbia University (1970). J.H. Christenson, G.S. Hicks, L.M. Lederman, P.J. Limon, B.G. Pope, E. Zavattini, Phys. Rev. D8, 2016 (1973).

[16] CCR Group: F.W. Busser, L. Camilleri, L. DiLella, G. Gladding, A. Placci, B.G. Pope, A.M. Smith, J.K. Yoh, E. Zavattini, B.J. Blumenfeld, L.M. Lederman, R.L. Cool, L. Litt, S.L. Segler, Phys. Lett. 46B, 471 (1973).
British-Scandanavian Group: B. Alper, H. Boggild, G. Jarlskog, G. Lynch, J.M. Weiss, P. Booth, L.J. Correll, J.N. Jackson, M. Prentice, G. von Dardel, L. Jonsson, G. Domgaard, K.H. Hansen, E. Lohse, F. Bulos, L. Leistam, A. Klovning, E. Lillethun, B. Duff, F. Heymann, D. Quarrie, Phys. Lett. 44B, 521 (1973).
Saclay-Strasbourg Group: M. Banner, J.L. Hamel, J.P. Pansart, A.V. Stirling, J. Teiger, H. Zaccone, J. Zsembery, G. Bossompierre, M. Croissiaux, J. Gresser, R. Morand, M. Riedinger, M. Schneegans, Phys. Lett. 44B, 537 (1973).

[17] F.W. Busser, L. Camilleri, L. DiLella, G. Gladding, A. Placci, B.G. Pope, A.M. Smith, J.K. Yoh, E. Zavattini, B.J. Blumenfeld, L.M. Lederman, R.L. Cool, L. Litt, S.L. Segler, Phys. Lett. 48B, 371 and 377 (1974).

[18] The experimenters were J.A. Appel, M.H. Bourquin, I. Gaines, D.C. Hom, L.M. Lederman, H.P. Paar, J-P. Repellin, D.H. Saxon, H.D. Snyder, J.M. Weiss, J.K. Yoh of Columbia University and B.C. Brown, J-M. Gaillard, T. Yamanouchi of Fermilab.

[19] A summary of these results has been previously published: J.A. Appel, M.H. Bourquin, I. Gaines, D.C. Hom, L.M. Lederman, H.P. Paar, J-P. Repellin, D.H. Saxon, H.D. Snyder, J.M. Weiss, J.K. Yoh, B.C. Brown, J-M. Gaillard, T. Yamanouchi, Phys. Rev. Lett. 33, 719 and 722 (1974). Other details not discussed in this thesis, in particular a detailed discussion of possible sources of the observed single lepton signal, can be found in H.P. Paar, Ph.D. Thesis, Nevis Report 208 (1975), Columbia University.

[20] Earlier tests of lead glass are discussed in B.J. Blumenfeld, L.M. Lederman, R.L. Cool, S.L. Segler, Nucl. Instr. & Meth. 97, 427 (1971). A more complete description of the lead glass detector used in this experiment is given in J.A. Appel, M.H. Bourquin, I. Gaines, D.C. Hom, L.M. Lederman, H.P. Paar, J-P. Repellin, D.H. Saxon, H.D. Snyder, J.M. Weiss, J.K. Yoh, B.C. Brown, C.N. Brown, J-M. Gaillard, J.R. Sauer, T. Yamanouchi, Nucl. Instr. & Meth. 127, 495 (1975).

[21] Earlier tests of this detector are discussed in M.H. Bourquin, D.H. Saxon, Nucl. Instr. & Meth. 108, 461 (1973).

[22] J.W. Cronin, H.J. Frisch, M.J. Shochet, J.P. Boymond, P.A. Piroue, R.L. Sumner, Phys. Rev. D11, 3105 (1975).

[23] J.A. Appel, M.H. Bourquin, I. Gaines, D.C. Hom, L.M. Lederman, H.P. Paar, J-P. Repellin, D.H. Saxon, H.D. Snyder, J.M. Weiss, J.K. Yoh, B.C. Brown, J-M. Gaillard, T. Yamanouchi, Phys. Rev. Lett. 33, 722 (1974) and Bull. Amer. Phys. Soc. 19, 446 (1974).

[24] J.P. Boymond, R. Mermod, P.A. Piroue, R.L. Sumner, J.W. Cronin, H.J. Frisch, M.J. Shochet, Phys. Rev. Lett. 33, 112 (1974).

[25] F.W. Busser, L. Camilleri, L. DiLella, B.G. Pope, A.M. Smith, B.J. Blumenfeld, S.N. White, A.F. Rothenberg, S.L. Segler, M.J. Tannenbaum, M. Banner, J.B. Cheze, J.L. Hamel, H. Kasha, J.P. Pansart, G. Smadja, J. Teiger, H. Zaccone, A. Zylberstejn, Phys. Lett. 53B, 212 (1974).

[26] D. Bintinger, J. Curry, J. Pilcher, C. Rubbia, L. Sulak, W. Ford, A.K. Mann, D. Cline, R. Imlay, P. Wanderer, Phys. Rev. Lett. 35, 72 (1975).

[27] L.B. Leipuner, R.C. Larsen, L.W. Smith, R.K. Adair, H. Kasha, C.M. Ankenbrandt, R.J. Stefanski, P.J. Wanderer, Phys. Rev. Lett. 34, 103 (1975).

[28] V. Lebedev, Proceedings of Batavia International Conference on High Energy Physics (1972), Vol. 2, p. 329.
S. Nurushev, Proceedings of London International Conference on High Energy Physics (1974), p. V-53.

[29] e.g., Paar and Paschos, Ref. 10; Farrar, Ref. 10.

[30] R.M. Sternheimer, Phys. Rev. 99, 277 (1955).

[31] F.W. Busser, L. Camilleri, L. DiLella, B.G. Pope, A.M. Smith, B.J. Blumenfeld, S.N. White, A.F. Rothenberg, S.L. Segler, M.J. Tannenbaum, M. Banner, J.B. Cheze, J.L. Hamel, H. Kasha, J.P. Pansart, G. Smadja, J. Teiger, H. Zaccone, A. Zylberstejn, Phys. Lett. 55B, 232 (1975).

[32] J.W. Cronin, H.J. Frisch, M.J. Shochet, J.P. Boymond, P.A. Piroue, R.L. Sumner, Phys. Rev. Lett. 31, 1426 (1973).

[33] British-Scandinavian Group, Phys. Lett. 44B, 521 (1973) and Nucl. Phys. B87, 19 (1975).

[34] D.C. Carey, M. Goldberg, J.R. Johnson, D.J. Ritchie, A. Roberts, R. Shafer, D. Theriot, E. von Goeler, J.K. Walker, M. Wong, F.E. Taylor, Phys. Rev. Lett. 32, 24 (1974). D.C. Carey, J.R. Johnson, R. Kammerud, M. Peters, D.J. Ritchie, A. Roberts, J.R. Sauer, R. Shafer, D. Theriot, J.K. Walker, F.E. Taylor, Phys. Rev. Lett. 33, 327 (1974).

[35] CCR Group, Phys. Lett. 46B, 471 (1973).

[36] F.W. Busser, L. Camilleri, L. DiLella, B.G. Pope, A.M. Smith, J.K. Yoh, B.J. Blumenfeld, L.M. Lederman, R.L. Cool, L. Litt, S.L. Segler, Phys. Lett. 51B, 306; 311 (1974).

[37] Saclay-Strasbourg Group, Phys. Lett. 44B, 537 (1973).

[38] Columbia-Fermilab Group, Phys. Rev. Lett. 33, 719 (1974) and this thesis.

[39] G. Finocchiaro, P. Grannis, D. Green, H. Jostlein, R. Kephart, R. Thun, S.R. Amendolia, G. Bellettini, P.L. Braccini, C. Bradoschia, R. Castaldi, C. Cerri, T. DelPrete, L. Foa, P. Giromini, P. Laurelli, A. Menzione, L. Ristori. G. Sanguinetti, M. Voldata, Phys. Rev. Lett. 50B, 396 (1974).

[40] Cited in M. Jacob, "Large Transverse Momentum Phenomena" ISR discussion meeting between experimentalists and theorists #10, 1974.

[41] S.D. Ellis, R. Thun, "Large Transverse Momentum Phenomena: An Experimental and Theoretical Review", Invited talk at the IXth Rencontre de Moriond (1974), Ref. TH 1874-CERN.

[42] A. Bassetto, M. Toller, L. Sertorio, Nucl. Phys. B34, 1 (1971).

[43] R. Blankenbecler, S.J. Brodsky, J.F. Gunion, Phys. Lett. 39B, 649 (1972).

[44] S.D. Ellis, Phys. Lett. 49B, 189 (1974).

APPENDIX

Calibration and Stability of the Lead Glass Array

The question of calibration of the lead glass array is complicated by the fact that it is not sufficient to measure the relative gain of each block of glass (plus one additional overall normalization). Instead, the blocks must be calibrated in their actual positions in the array, so that the calibration will reflect the energy distribution and light collection as generated by an actual electromagnetic shower.

Thus, the basic calibration method consists of exposing the entire array to a monochromatic or momentum analyzed electron beam, and recording the pulse heights in all the blocks of glass that participate in the shower. The array is then moved to expose different sections of it to the calibrating beam. This procedure was first tried in a test beam at Brookhaven National Laboratory, using 5 to 14 GeV electrons identified by a Cerenkov counter; while the actual calibration was performed in the experimental pit at Fermilab using a special calibration channel at 20 m rad. Our magnets and hodoscopes were moved to 20 mrad to provide momentum determination (with improved momentum resolution because of the smaller aperture at 20 mrad), and 1/4 in. of lead was inserted in the secondary beam to provide a copious yield of electrons.

The calibration constants for the individual blocks of glass are then derived as follows: Assume the shower is contained in N blocks of glass, and that for each of M individual showers of total energy E^i, we record the pulse height h_j^i in each block of glass. (i is a superscript indexing the event number, i = 1, ... M. j and k are subscripts indexing the block number, j,k = 1, ... N.) Each block has a calibration constant a_j, so that the energy in block j is $E_j = a_j h_j$. For each event i, the total energy E^i is

$$E^i = \sum_{j=1}^{N} a_j h_j^i \quad \text{or} \quad 1 = \sum_j a_j \frac{h_j^i}{E^i} = \sum_j a_j \tilde{h}_j^i$$

where $\tilde{h}_j^i = h_j^i / E^i$

multiplying by $\tilde{h}_k^i$,

$$\tilde{h}_k^i = \sum_j a_j \tilde{h}_j^i \tilde{h}_k^i \quad .$$

Summing over all events i, we have:

$$\sum_{i=1}^{M} \tilde{h}_k^i = \sum_{i=1}^{M} \sum_{j=1}^{N} a_j \tilde{h}_j^i \tilde{h}_k^i = \sum_{j=1}^{N} \alpha_j \left(\sum_{i=1}^{M} \tilde{h}_j^i \tilde{h}_k^i \right) \text{ for } k=1,\ldots N \; .$$

This represents N simultaneous equations (one for each value of k) for the N unknown a_j. In other words, defining the matrices

$$H_k \equiv \left(\sum_{i=1}^{M} \tilde{h}_k^i \right) \quad X_{jk} = \left(\sum_{i=1}^{M} \tilde{h}_j^i \tilde{h}_k^i \right) \quad A_j = (a_j)$$

the above equation becomes $H_k = A_j X_{jk}$, and we can solve for A as $\boxed{A_j = X_{jk}^{-1} H_k}$.

This method relies on the shower being distributed differently among the N blocks for different events (else the linear equations are not independent), and allows us to obtain relative calibration constants for each block using the constraint that the total energy in the shower is constant for the different events.

This solution for the calibration constants can be derived using an alternative method which makes the effects of the individual resolutions of the blocks of glass somewhat clearer. Because of the finite resolution of the detector, the measured energies for each shower will be distributed around the actual energies, and the widths of these distributions will be minimized when the proper relative calibrations are used for each block. (Incorrect relative calibrations will produce an added width to the distribution as energy moves from one block to another in different events; thus this method also relies on the fluctuations in shower distribution from block to block being large compared to the resolution of each block.)

With the same notation as above, we can express the resolution as:

$$\Delta E^i = 1 - \sum_j a_j \tilde{h}_j^i$$

$$(\Delta E^i)^2 = (1 - \sum_j a_j \tilde{h}_j^i)^2$$

$$\sigma^2 = \sum_{i=1}^{M} (\Delta E^i)^2 = \sum_{i=1}^{M} (1 - \sum_{j=1}^{N} a_j \tilde{h}_j^i)^2$$

and the problem is then to minimize σ^2 subject to the constraint that the average fluctuation is 0:

$$\sum_i \Delta E^i = 0 = \sum_i (1 - \sum_j a_j \tilde{h}_j^i)$$

i.e., treating the problem with a Lagrange multiplier, minimize:

$$\mathcal{L} = \sum_{i=1}^{M} (1 - \sum_{j=1}^{N} a_j \tilde{h}_j^i)^2 + \lambda \sum_{i=1}^{M} (1 - \sum_{j=1}^{N} a_j \tilde{h}_j^i) \quad .$$

Differentiating with respect to each a_k, we obtain:

$$\frac{\partial \mathcal{L}}{\partial a_k} = 0 = \sum_i [-(2+\lambda)\tilde{h}_k^i + \sum_j 2a_j \tilde{h}_j^i \tilde{h}_k^i]$$

or

$$(1 + \frac{\lambda}{2}) \sum_i \tilde{h}_k^i = \sum_j a_j \sum_i \tilde{h}_j^i \tilde{h}_k^i$$

yielding the same equations as above for the solutions for a_j.

An additional method of calibration utilizes muon straight-throughs, which deposit a fixed amount of energy in each block of glass due to Cerenkov radiation, with the amount of light simply proportional to the path length of the muon in the glass. Exposing the array to muons at the same time that the electron calibration is done establishes an "equivalent electron energy" for the fixed amount of light generated by the muon straight-through. These are measured as 132 MeV for the first two rows of glass (path length 14.6 cm transverse to the beam) and 550 MeV for the back row (path length 35.0 cm longitudinal to the beam). The lack

of proportionality to path length is due to the differing light collection efficiency for the very directional Cerenkov radiation for the muon straight-through, which deposits its energy uniformly through the length of the block, compared to an electromagnetic shower, and illustrates why the array must be calibrated with the blocks in their actual positions.

The validity of this method is verified by the experimental observation that the equivalent electron energy for a muon straight-through is constant for all blocks with the same orientation with respect to the beam. Once these constants have been measured, the entire array can be rapidly and conveniently calibrated at any time by measuring the pulse heights due to straight-throughs.

Finally, once the calibration is established, the stability of the system is measured in three separate ways. First, we use a light flasher system, consisting of a hydrogen thyratron flasher driven by a high voltage pulser and a system of lucite light pipes and sheets which distribute a fixed portion of the light to each block of glass. The flasher is also viewed by four calibration photomultiplier tubes, each of which has a crystal of sodium iodide doped with Americium glued to its face to provide an absolute normalization. Light flasher data are taken roughly once per eight hour shift, providing a record of any short term fluctuations in gain of the lead glass system.

Secondly, muon straight-through data are taken regularly, roughly once per day, using a special muon trigger and changing the gains of the ADC's by a factor of 20. Thirdly, special runs with 1/4 in. of lead inserted in the secondary beam to provide a copious electron yield are also taken regularly, and measurement of the average E/P (energy measured by the lead glass divided by momentum measured by the magnet hodoscope system) for a large sample of electrons at each point in the array provides an additional measurement of the stability of the system. (These runs are also used to measure corrections to the calibration as a function of the position of the shower in the array, as described above.)

The agreement among these three methods is excellent. (This was checked by taking special runs with the high voltages of the phototubes on the glass blocks lowered by 50 volts, and measuring the change in gain by each of the three methods.) The overall changes in gain during the course of the experiment were of the order of 1% per month, or a total variation of less than 10% during the course of the experiment. Measured corrections for these variations resulted in a calibration accurate to better than 1/2% at any point in time.

FIGURE CAPTIONS

Fig. 1 Diagram of reaction.

Fig. 2 Single lepton transverse momentum distribution for two-body decay of W boson $W^{\pm} \rightarrow e^{\pm}\nu$.

Fig. 3 Experimental apparatus.

Fig. 4 Beam line.

Fig. 5 Experimental Acceptance of two different magnet currents. (100% = 81 μsr.)

Fig. 6 Hodoscopes and trigger counters.

Fig. 7 Lead glass array.

Fig. 8 Hadron detectors.

Fig. 9 Pulse height in hadron calorimeter, showing π/μ discrimination.

Fig. 10 Electronics logic diagram.

Fig. 11 T2 counter trigger thresholds.

Fig. 12 Lead glass dynode (ϵ_{12}) triggering thresholds. (x=accept.)

Fig. 13 Schematic diagram of reconstruction.

Fig. 14 Target reconstruction of unambiguous events.

Fig. 15 Crude trajectory fitting and momentum resolution.

Fig. 16 Corrections to energy deposit in lead glass.

Fig. 17 Energy resolution in lead glass.

Fig. 18 Fraction of energy (E/p) deposited in lead glass for all particles passing through apparatus.

Fig. 19 E/p distribution for all electron triggers.

Fig. 20 E counter pulse height, π vs. electron.

Fig. 21 Longitudinal shower distribution, π vs. electron.

Fig. 22 Longitudinal shower distribution for electrons as a function of energy.

Fig. 23 E/p distribution after electron cuts.

Fig. 24 E/p distribution of hadron background, uncut and cut.

Fig. 25 Electron yield as a function of foil thickness.

Fig. 26 A dependence of cross section as a function of transverse momentum.

Fig. 27 Direct lepton yield, e^+ vs. e^-.

Fig. 28 Direct lepton/π^o ratio as a function of $p_\perp$ at two angles.

Fig. 29 Invariant cross section for direct electron production.

Fig. 30 Invariant cross section for conversion electrons produced in 1% of a radiation length of matter.

Fig. 31 Invariant cross section for π^o production.

Fig. 32 Spectrum of conversion electrons derived from π^o spectrum with a bump.

Fig. 33 Invariant cross section for charged hadron production.

Fig. 34 Comparison with other experiments, all at 90^o in center of mass:

a) π^o, this experiment,

b) fit to π^o, CCR experiment at ISR[35],

c) negative hadrons, this experiment,

d) $\pi^+ + \pi^-/2$, Chicago-Princeton experiment at FNAL.[32]

Fig. 35 Ratio of negative to neutral hadron production.

a)
This experiment:
Lepton Pair
Production

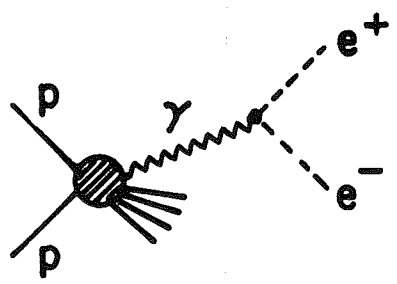

Timelike γ

b)
Deep Inelastic
Scattering

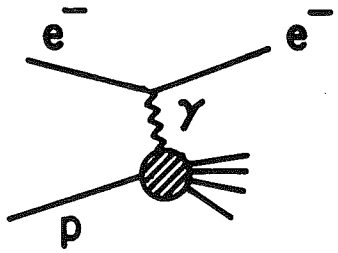

Spacelike γ

c)
Electron Positron
Annihilation

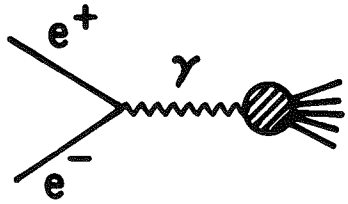

Timelike γ

d)
This experiment:
Single lepton
Production

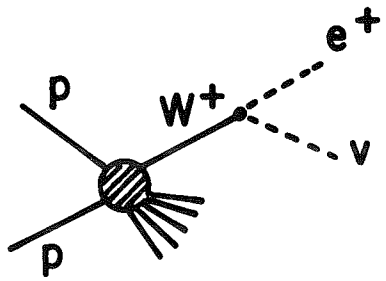

FIG. 1

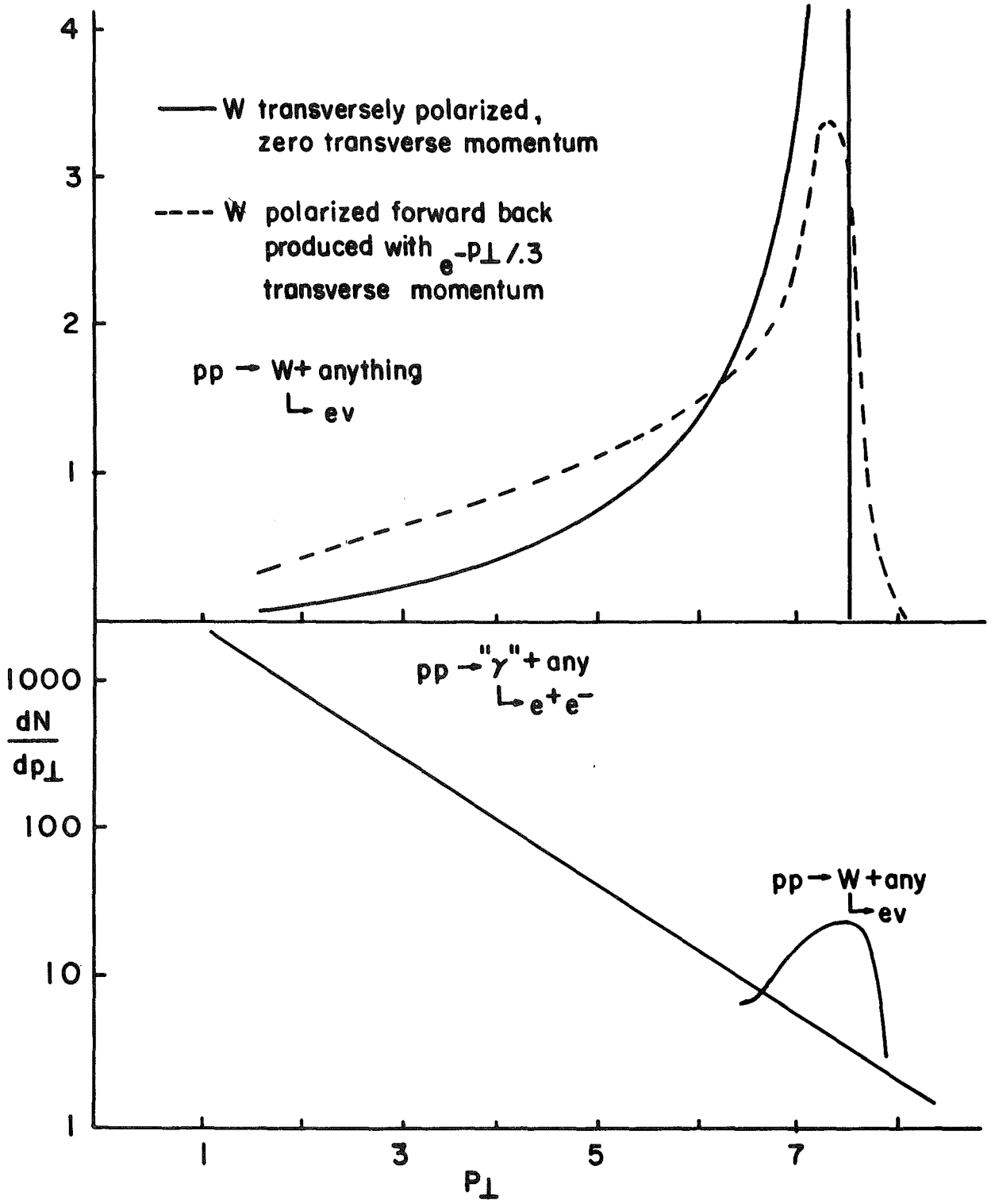

Single Electron Transverse Momentum Spectrum from W decay
W mass = 15 GeV

FIG. 2

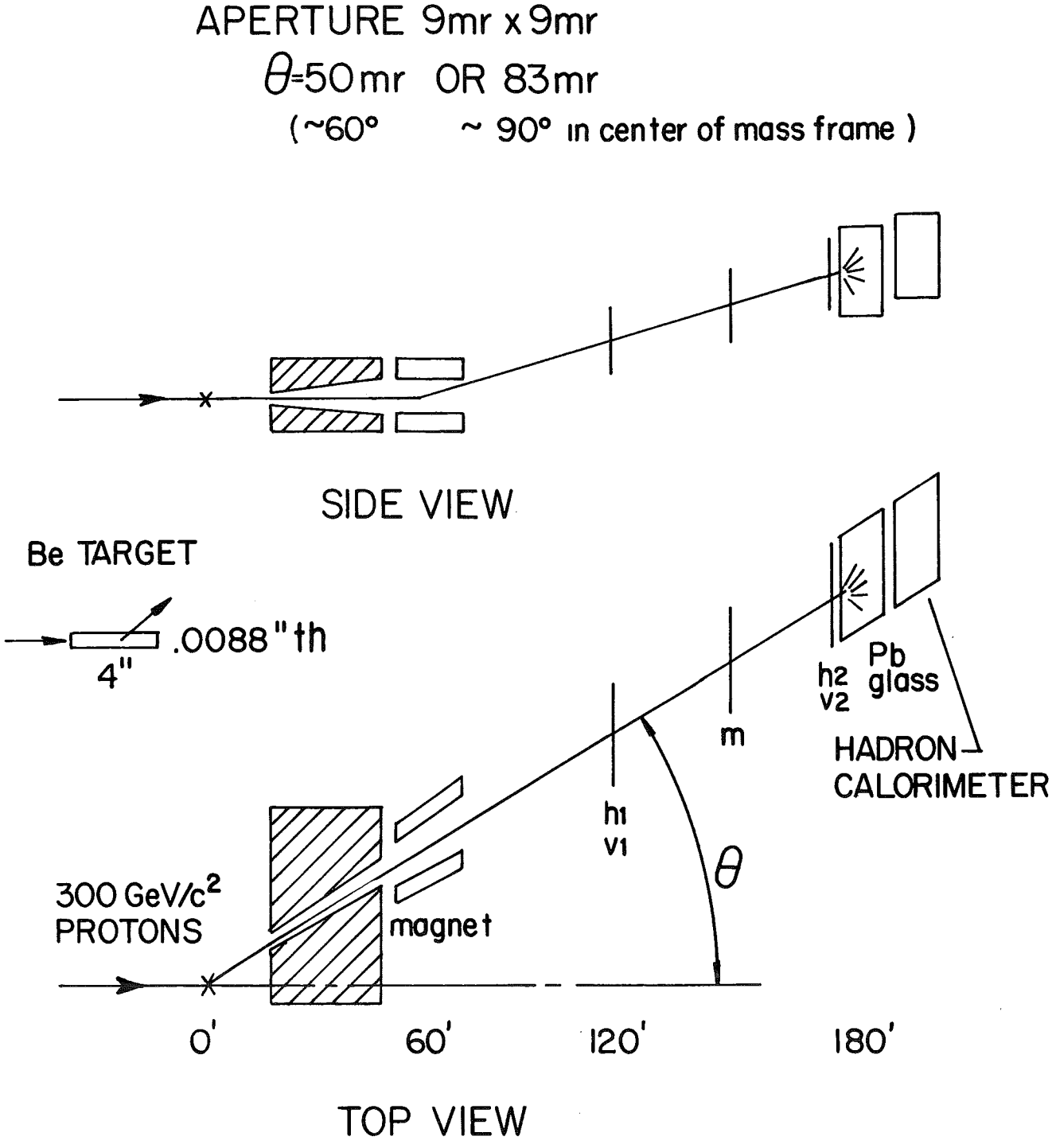
APERTURE 9mr x 9mr
θ=50mr OR 83mr
(~60° ~ 90° in center of mass frame)
SIDE VIEW
Be TARGET
.0088" th
4"
h2
v2
Pb
glass
HADRON
CALORIMETER
m
h1
v1
θ
300 GeV/c²
PROTONS
magnet
0'
60'
120'
180'
TOP VIEW

FIG. 3

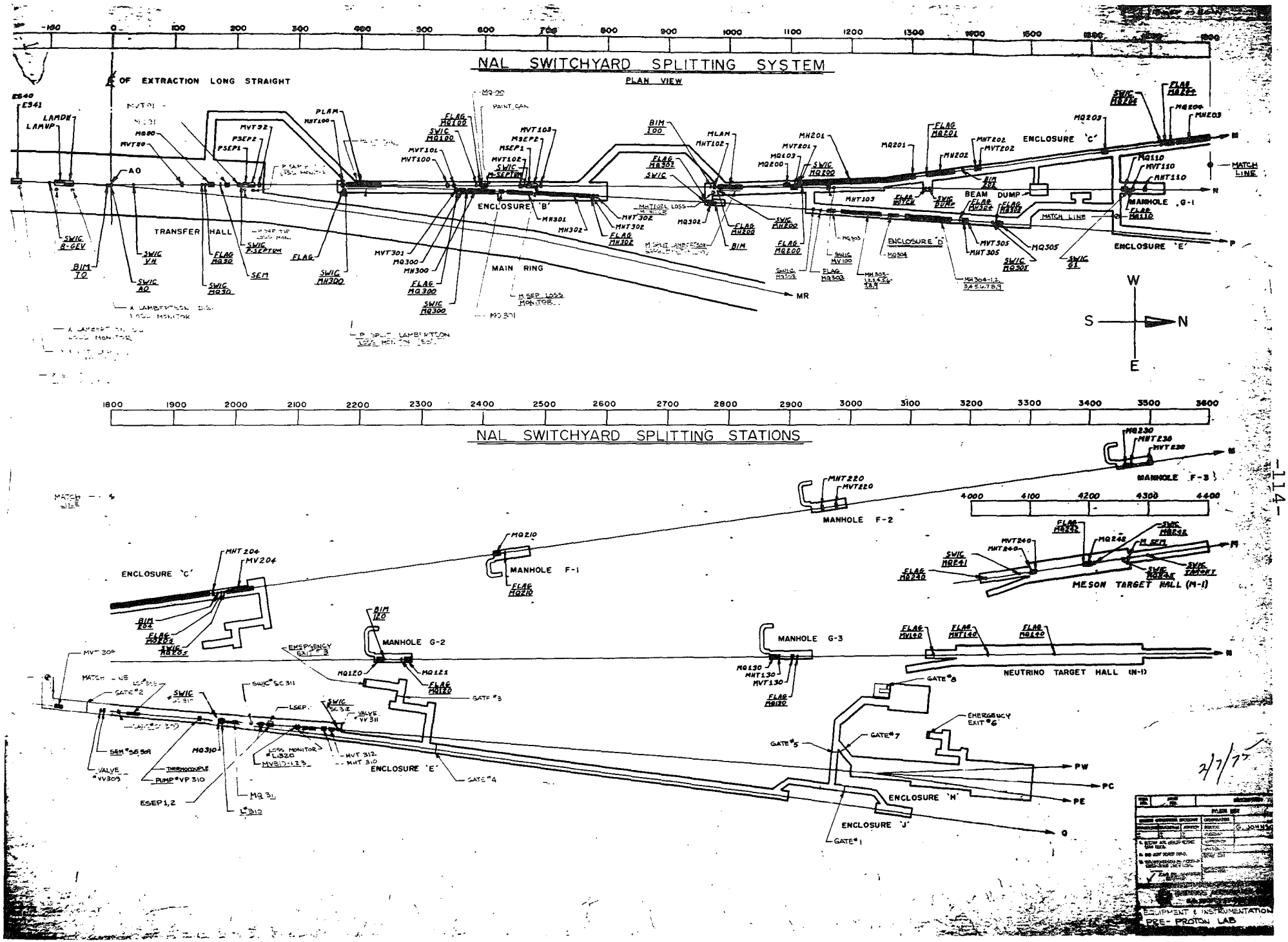
NAL SWITCHYARD SPLITTING SYSTEM
PLAN VIEW
℄ OF EXTRACTION LONG STRAIGHT
TRANSFER HALL
ENCLOSURE 'B'
ENCLOSURE 'C'
ENCLOSURE 'D'
ENCLOSURE 'E'
MAIN RING
MR
BEAM DUMP
MANHOLE G-1
MATCH LINE
W
S
N
E
NAL SWITCHYARD SPLITTING STATIONS
MANHOLE F-1
MANHOLE F-2
MANHOLE F-3
MANHOLE G-2
MANHOLE G-3
MESON TARGET HALL (M-1)
NEUTRINO TARGET HALL (N-1)
ENCLOSURE 'H'
ENCLOSURE 'J'
PW
PC
PE
EMERGENCY EXIT #3
EMERGENCY EXIT #6
GATE #1
GATE #2
GATE #3
GATE #4
GATE #5
GATE #7
GATE #8
EQUIPMENT & INSTRUMENTATION
PRE-PROTON LAB

FIG. 4

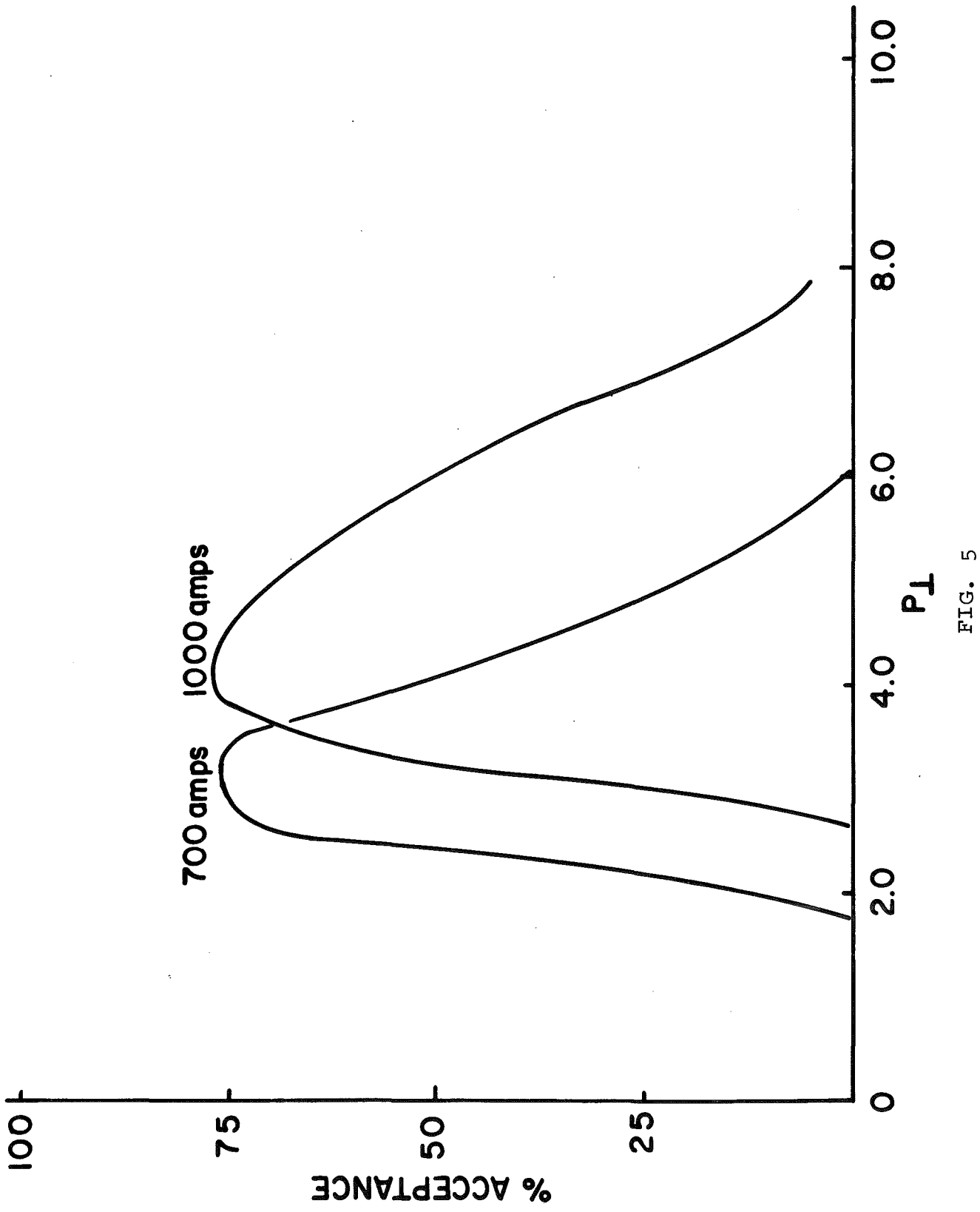

FIG. 5

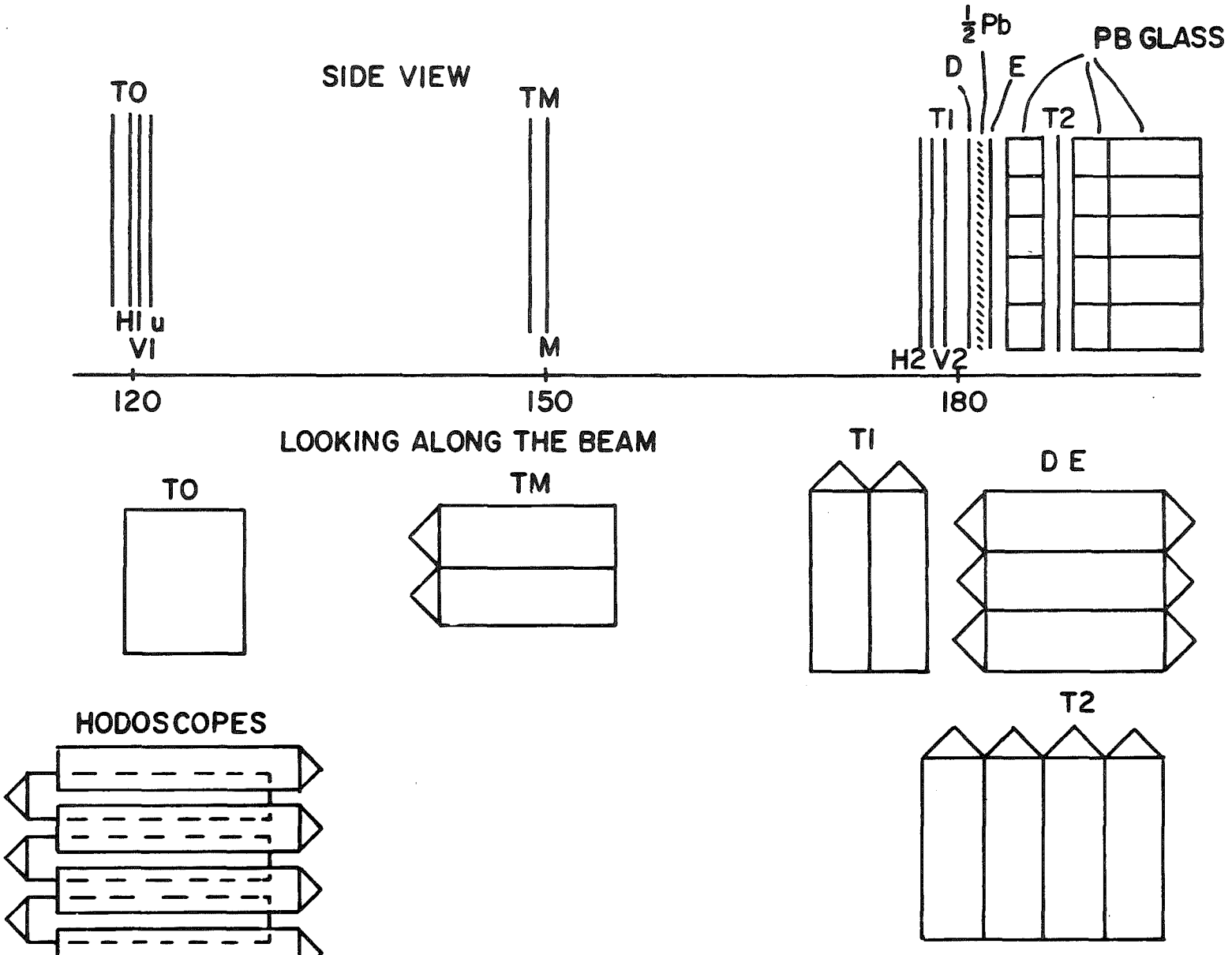

HODOSCOPES AND TRIGGER COUNTERS

FIG. 6

LEAD GLASS CALORIMETER

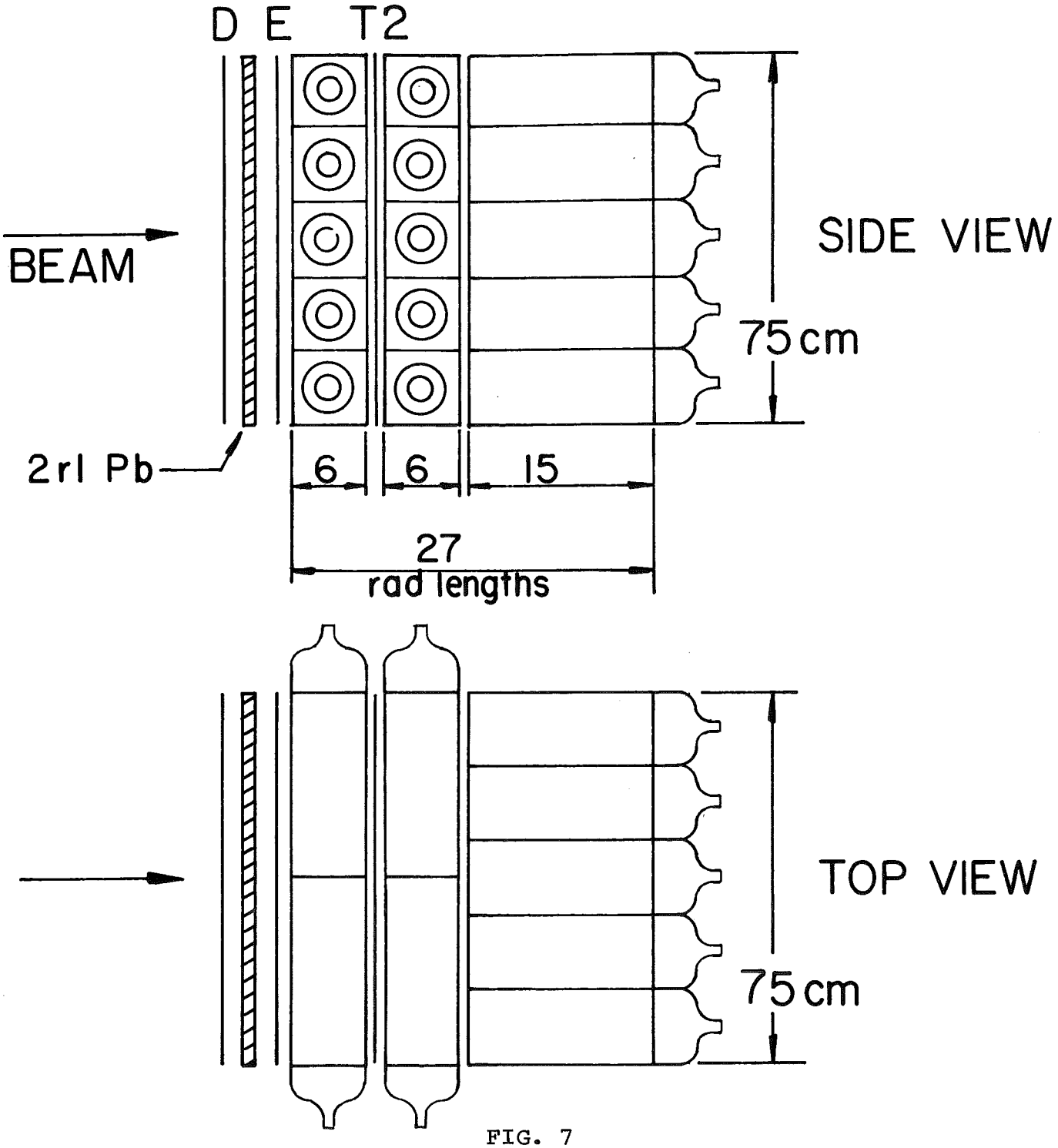

FIG. 7

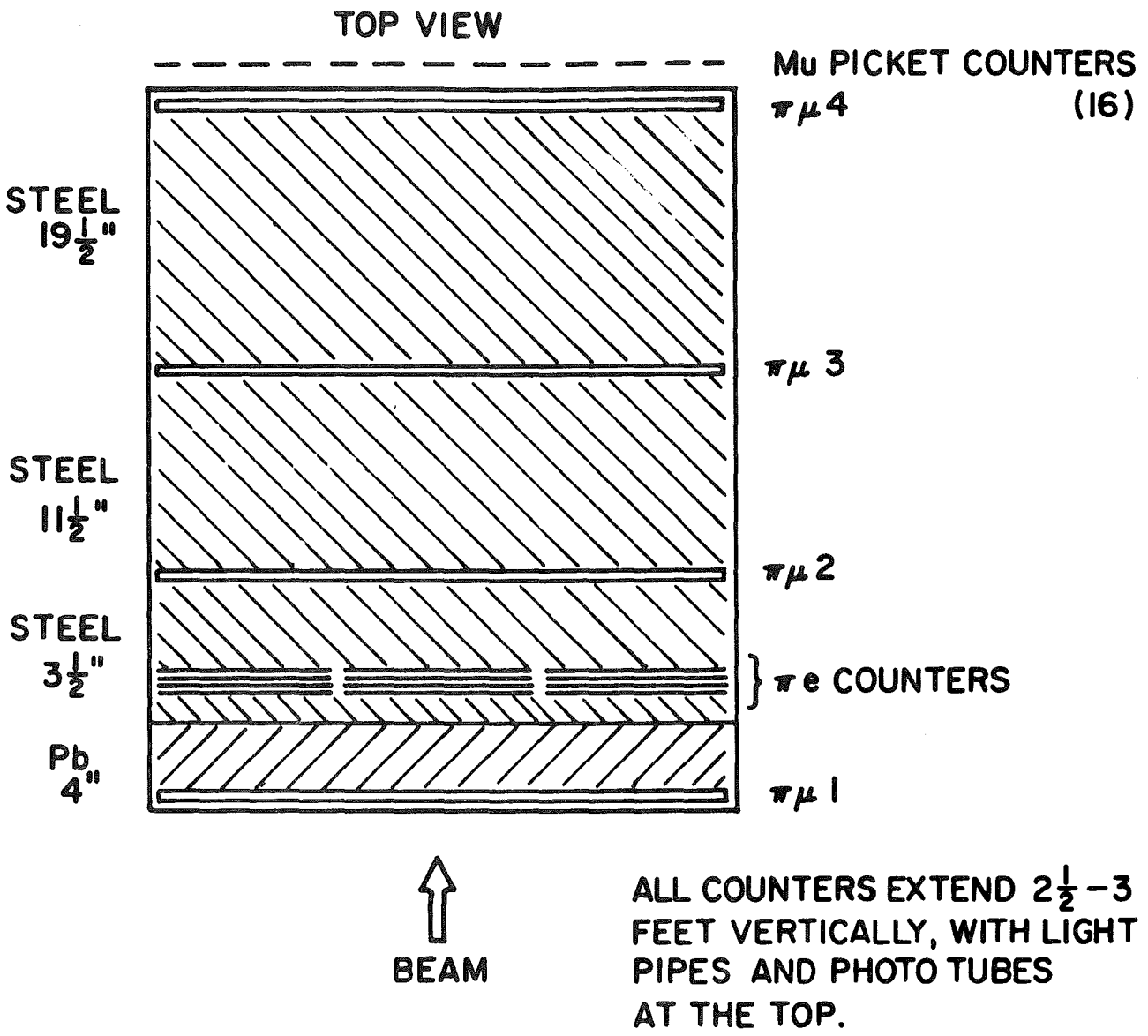

HADRON DETECTORS

FIG. 8

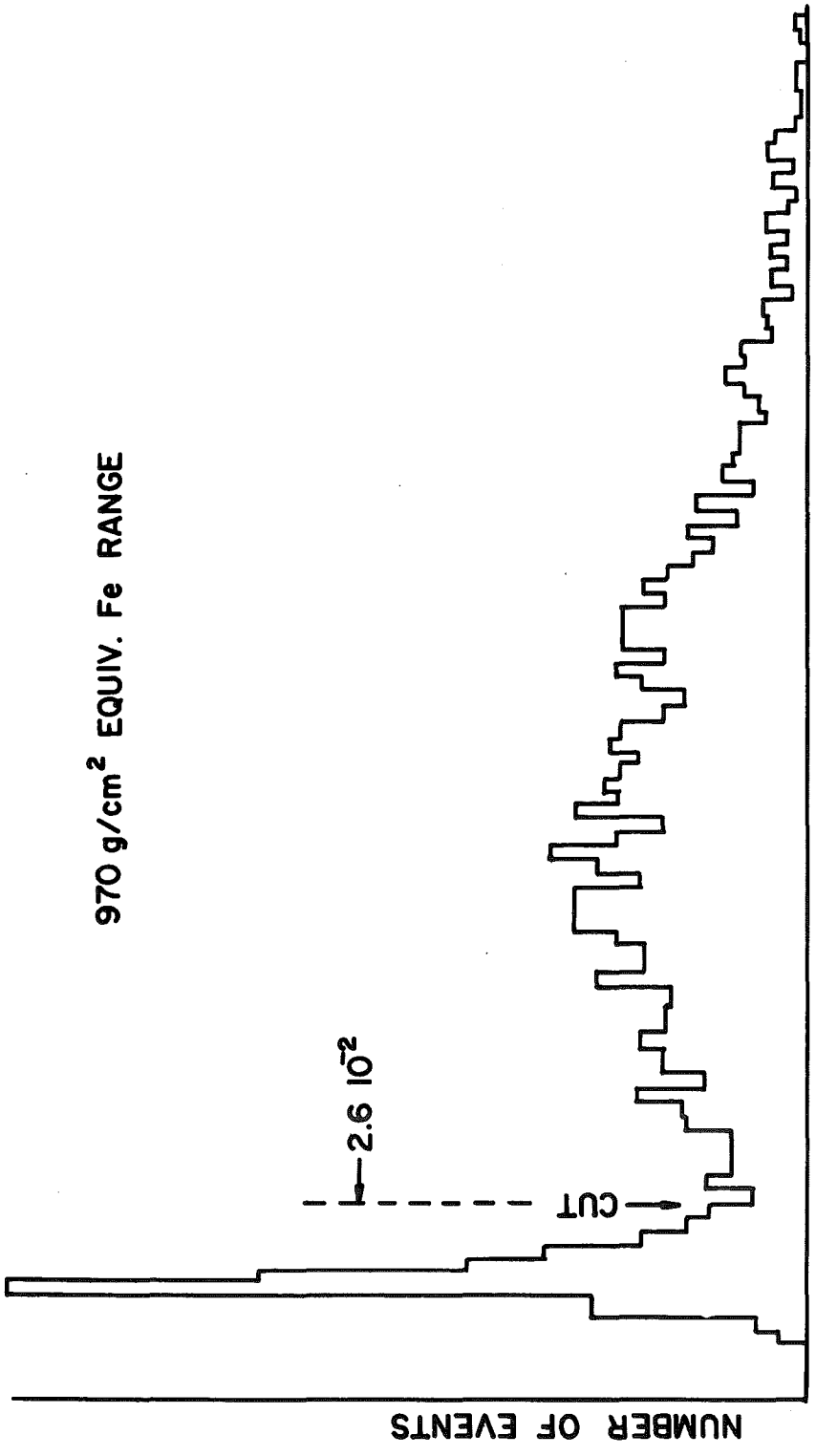
970 g/cm² EQUIV. Fe RANGE
2.6 10⁻²
CUT
NUMBER OF EVENTS
NUMBER OF EQUIVALENT SINGLE IONISING PARTICLES

FIG. 9

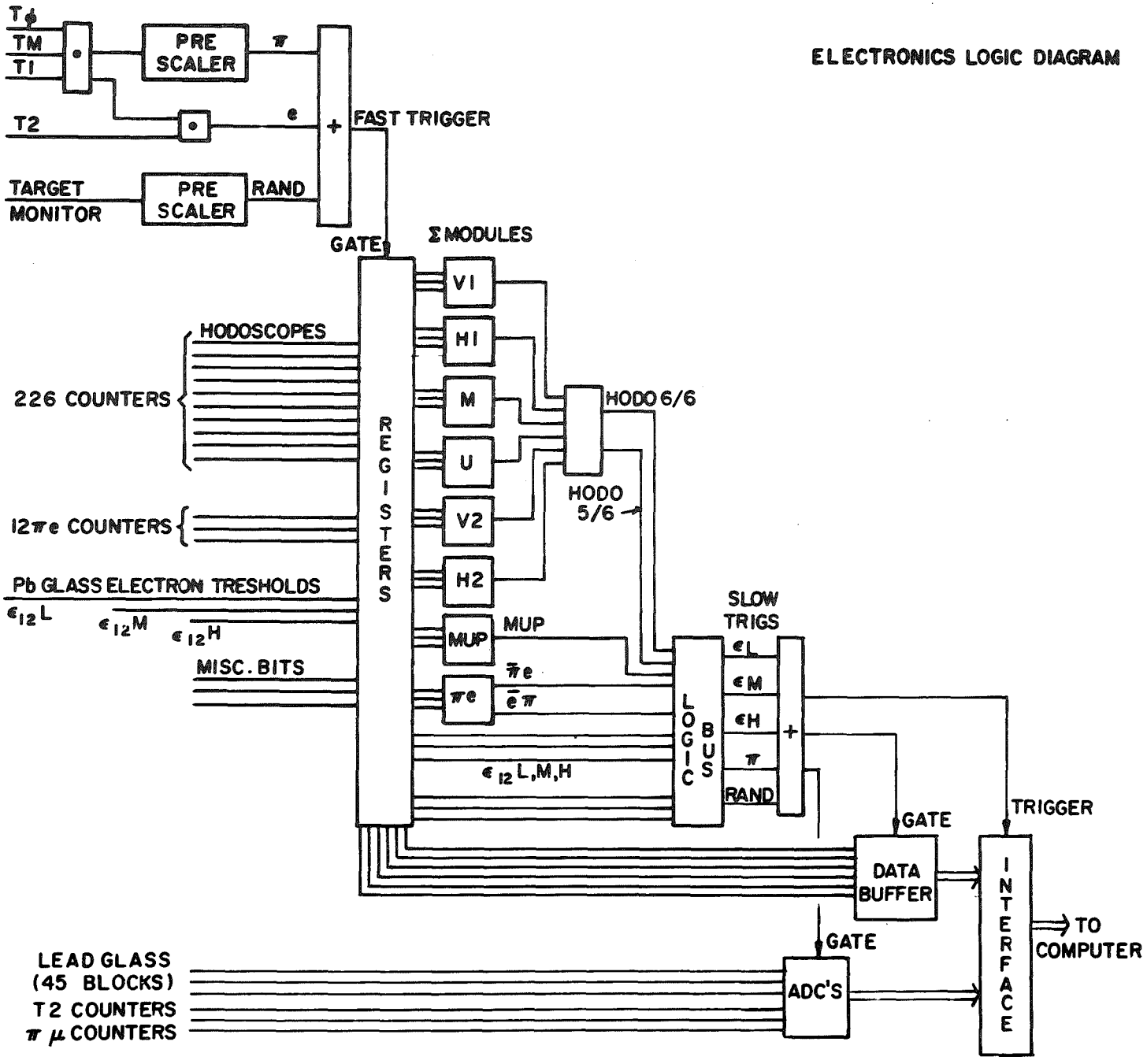
ELECTRONICS LOGIC DIAGRAM
Tϕ
TM
TI
PRE SCALER
π
T2
e
FAST TRIGGER
TARGET MONITOR
PRE SCALER
RAND
GATE
ΣMODULES
V1
H1
M
U
V2
H2
MUP
πe
HODOSCOPES
226 COUNTERS
12πe COUNTERS
Pb GLASS ELECTRON TRESHOLDS
ϵ12L
ϵ12M
ϵ12H
MISC. BITS
REGISTERS
HODO 6/6
HODO 5/6
MUP
SLOW TRIGS
ϵL
ϵM
ϵH
π
RAND
LOGIC BUS
ϵ12L,M,H
GATE
TRIGGER
DATA BUFFER
INTERFACE
TO COMPUTER
GATE
LEAD GLASS (45 BLOCKS)
T2 COUNTERS
π μ COUNTERS
ADC'S

FIG. 10

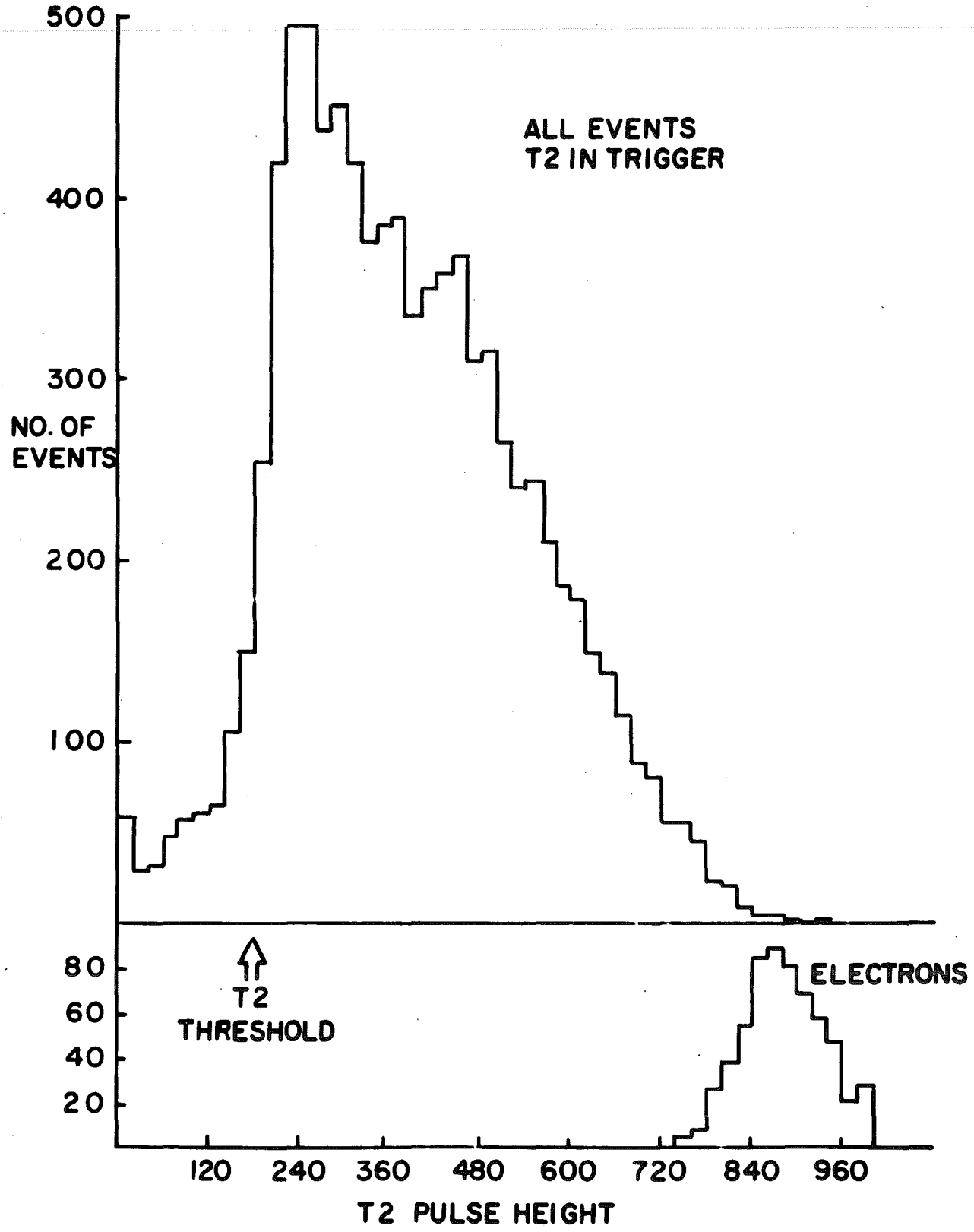
500
400
300
NO. OF EVENTS
200
100
ALL EVENTS
T2 IN TRIGGER
80
60
40
20
T2
THRESHOLD
ELECTRONS
120
240
360
480
600
720
840
960
T2 PULSE HEIGHT

FIG. 11

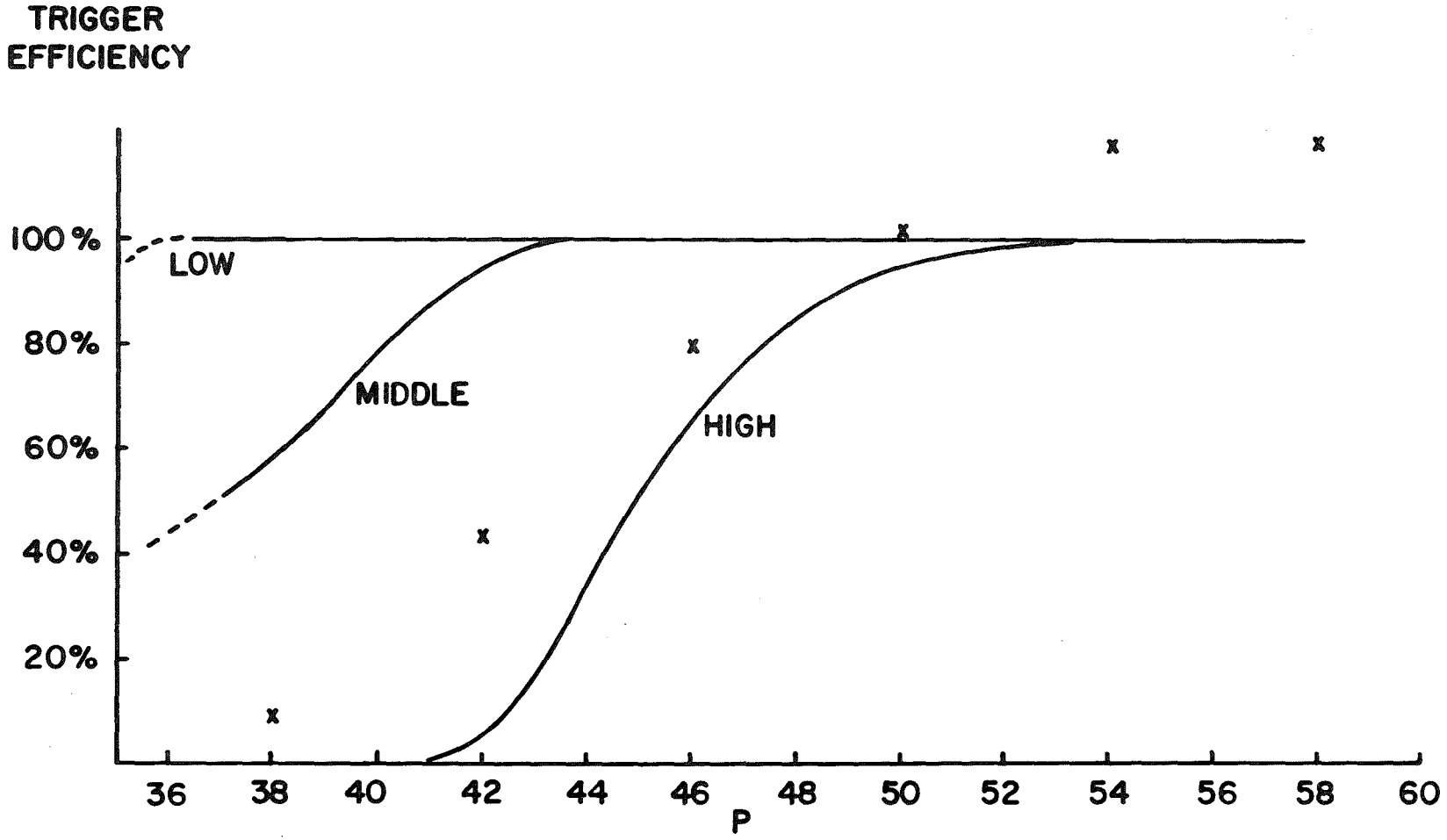
TRIGGER
EFFICIENCY
100%
80%
60%
40%
20%
LOW
MIDDLE
HIGH
36
38
40
42
44
46
48
50
52
54
56
58
60
P

FIG. 12

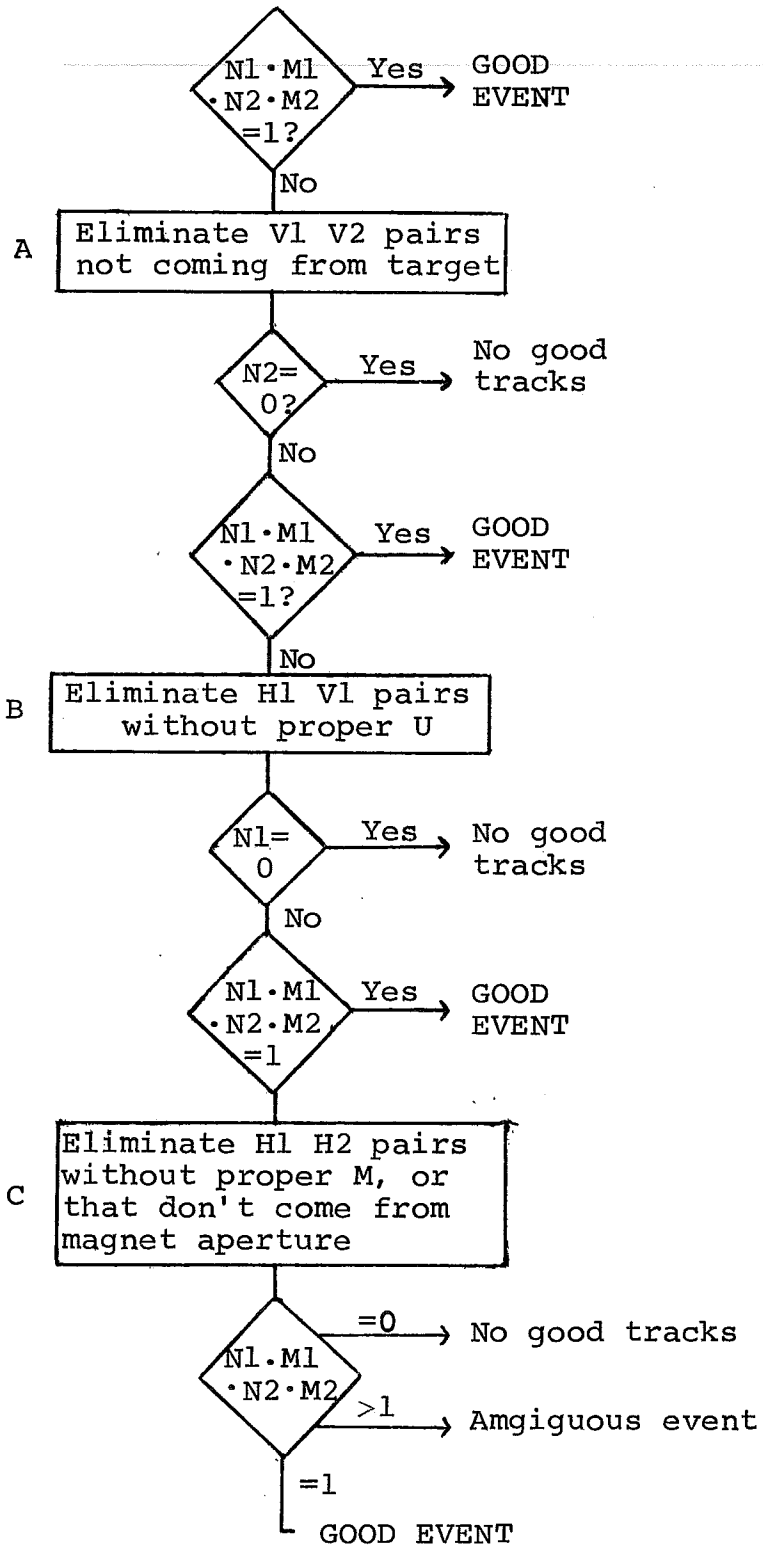

Let N1, M1, N2, M2 = the number of elements in planes V1, H1, V2, H2. The event is good (i.e. has a unique trajectory) when there is exactly one element in each plane, or when the product

$$N1 \cdot M1 \cdot N2 \cdot M2 = 1$$

All events are either good events, ambiguous, or have no good tracks.
For a typical run:

~ 80 % are good
~ 10 % are ambiguous
~ 10 % have no track

Fig. 13

HIST OF QUAN 63 BETWEEN -250 AND 250 WITH CUTS = 00022005
5780 OF 42110 EVENTS PASSED CUTS
UNDERFLOW = 48 OVERFLOW = 52 IN HIST = 5680
MEAN = -3.36321 +- 29.7206%
EACH 0 + 40 EVENTS

BIN	COUNTS	TOTAL	I----+----I----+----I----+----I----+----I
1	1	1	I
2	1	2	I
3	2	4	I
4	5	9	I
5	5	14	I
6	3	17	I
7	3	20	I
8	2	22	I
9	8	30	I
10	3	33	I
11	5	38	I
12	5	43	I
13	6	49	I
14	9	58	I
15	8	66	I
16	2	68	I
17	11	79	I
18	4	83	I
19	17	100	I
20	7	107	I
21	11	118	I
22	84	202	I00
23	203	405	I00000
24	1470	1875	I0000000000000000000000000000000000
25	1579	3454	I00000000000000000000000000000000000000
26	1247	4701	I000000000000000000000000000000
27	548	5249	I0000000000000
28	187	5436	I0000
29	100	5536	I00
30	29	5565	I
31	15	5580	I
32	12	5592	I
33	5	5597	I
34	16	5613	I
35	11	5624	I
36	6	5630	I
37	3	5633	I
38	7	5640	I
39	6	5646	I
40	3	5649	I
41	3	5652	I
42	4	5656	I
43	2	5658	I
44	2	5660	I
45	2	5662	I
46	1	5663	I
47	5	5668	I
48	6	5674	I
49	3	5677	I
50	3	5680	I

Fig. 14

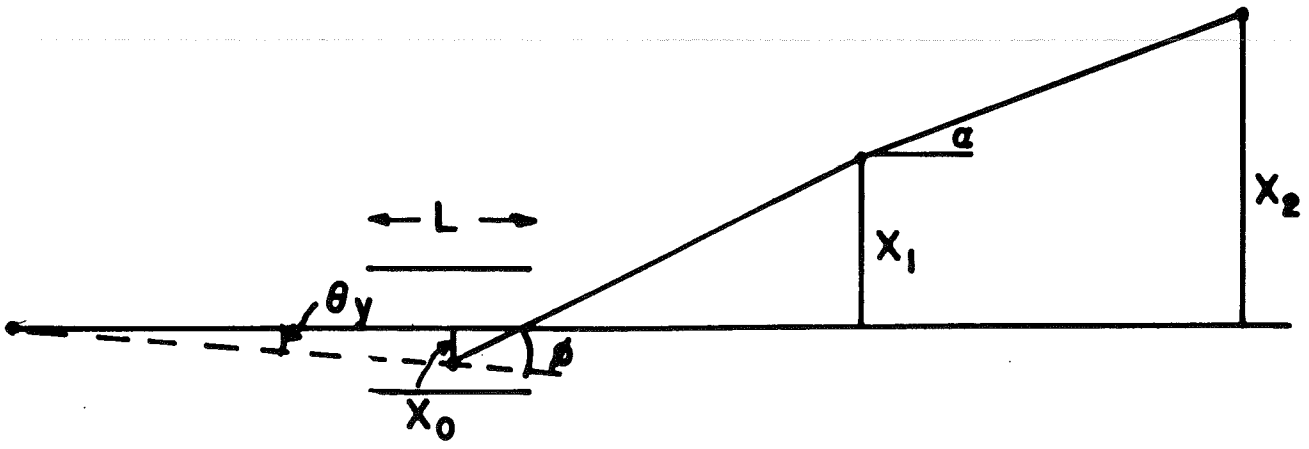

Target	Magnet Z_o	H1 Z_1	H2 Z_2
0 ft	60 ft	120 ft	180 ft

From hodoscopes H1 and H2 we know the heights X_1 and X_2 for each event. Then

$$p(\text{GeV/c}) = \frac{3\ B(\text{kg})\ L(\text{cm})}{10^4\ \phi(\text{rad})}$$

$$\phi = \alpha - \theta_y \quad \text{with } \alpha = X_2 - X_1 / Z_2 - Z_1$$

$$\text{and } \theta_y = X_o / Z_o$$

assuming a single bend at the center of the magnet.

But,

$$\frac{X_2-X_1}{Z_2-Z_1} = \frac{X_2-X_o}{Z_2-Z_o} \quad \text{so } X_o = X_2 - \frac{(X_2-X_1)(Z_2-Z_o)}{Z_2-Z_1}$$

$$\phi = \frac{X_2-X_1}{Z_2-Z_1} - \frac{X_2}{Z_o} + \frac{(X_2-X_1)(Z_2-Z_o)}{Z_o(Z_2-Z_1)} = \frac{(X_2-X_1)Z_o+(X_2-X_1)(Z_2-Z_o)-X_2(Z_2-Z_1)}{(Z_2-Z_1)Z_o}$$

or $$\phi = \frac{X_2Z_1-X_1Z_2}{(Z_2-Z_1)Z_o}$$

Fig. 15a

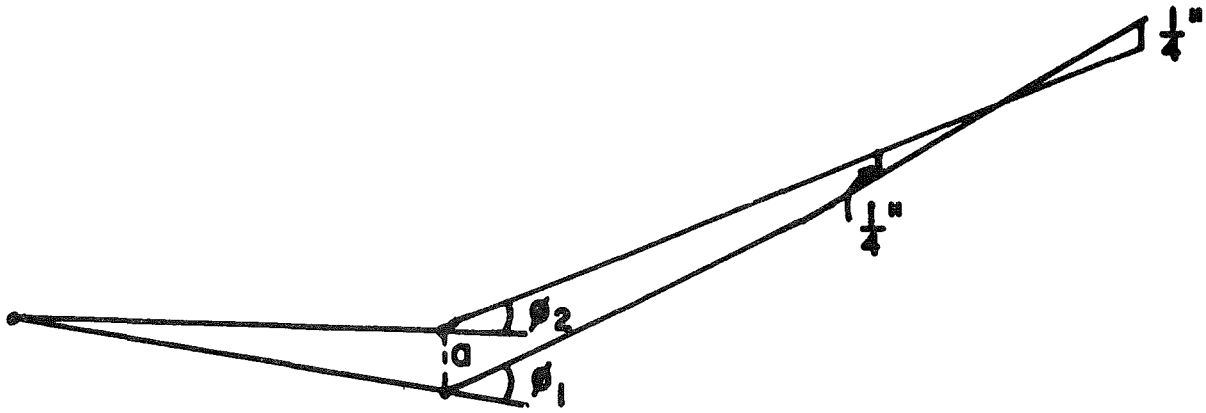

Target Magnet H1 H2

0 ft 60 ft 120 ft 150 ft 180 ft

Momentum resolution for a given pair of elements in H1 and H2 is determined by the difference in the bend angle ϕ for the two rays shown.

Since the size of each element is 1/4 in., the distance a is

$$\frac{a}{150-60} = \frac{1/4}{150-120} \qquad a = \frac{90}{30}\,1/4 = 3/4 \text{ in.}$$

$$\phi_1-\phi_2 = (\alpha_1-\theta_{y_1})-(\alpha_2-\theta_{y_2})$$

$$= \alpha_1-\alpha_2 + \theta_{y_2}-\theta_{y_1}$$

$$= \begin{matrix}\text{total}\\ \text{displacement}\\ \text{of}\\ \text{1 in. in}\\ \text{120 ft}\end{matrix} \quad \begin{matrix}\text{total}\\ \text{displacement}\\ \text{of}\\ \text{3/4 in. in}\\ \text{60 ft}\end{matrix}$$

$$= 2/3 \text{ mrad} + 1 \text{ mrad}$$

$\Delta\phi$ = 5/3 mrad at the base, or $\Delta\phi$ = 5/6 mrad FWHM

compared to a typical bend angle at 500 A of

ϕ = 40 mrad for 25 GeV, so Δp = 2.5%

and ϕ = 20 mrad for 50 GeV, so Δp = 5. %

Fig. 15b

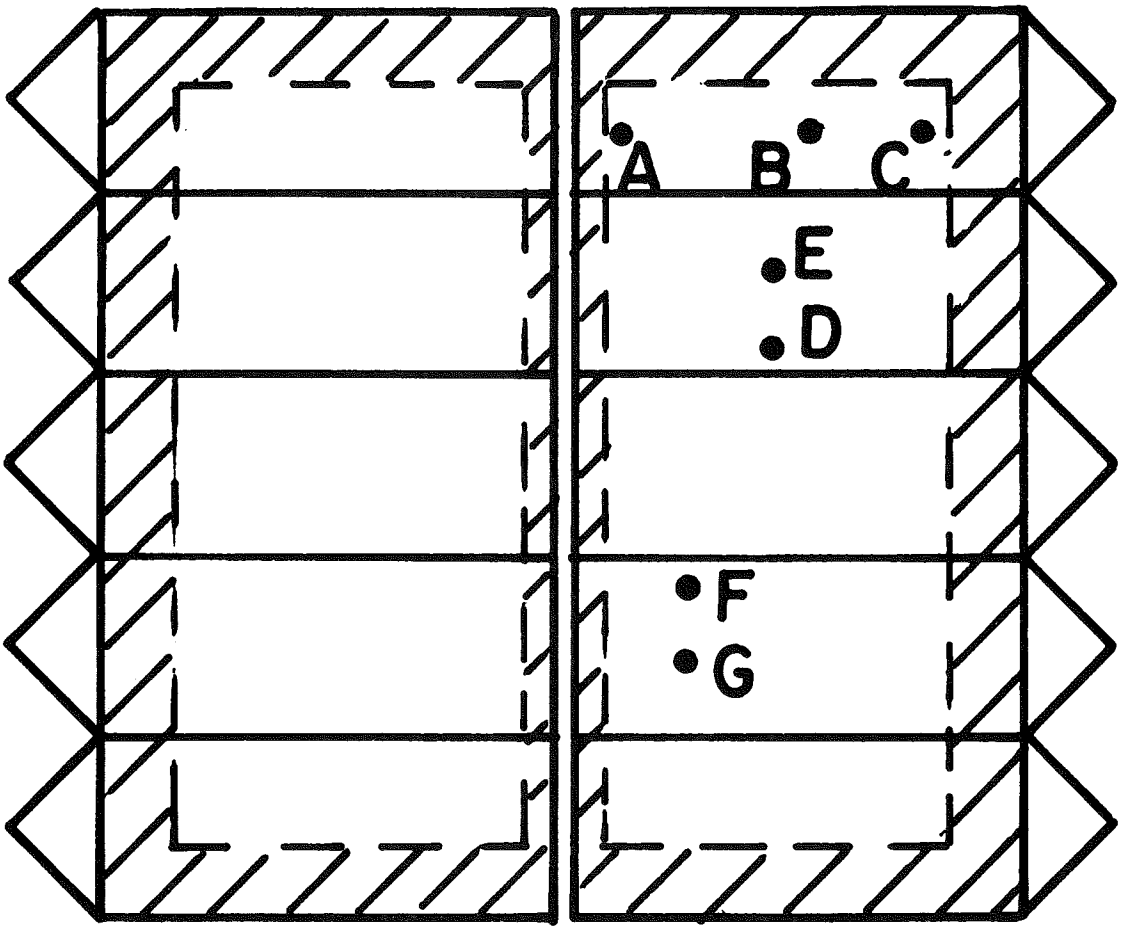

Fiducial Cuts = shaded area

Cone Size r = 2 in. in front layer
2 1/4 in. in second layer
2 1/2 in. in third layer

Transit Correction	B vs. A	(6 in.)	-1%
	C vs. A	(10 in.)	-6%
Crack Correction	D vs. E		+2%
	(within 1/2 in. of crack)		
Cone Correction	G vs. F		+1.4%
	(only 1 horizontal row instead of 2)		
	H vs. I		+0.4%
	(only 1 vertical row instead of 2)		

FIG. 16

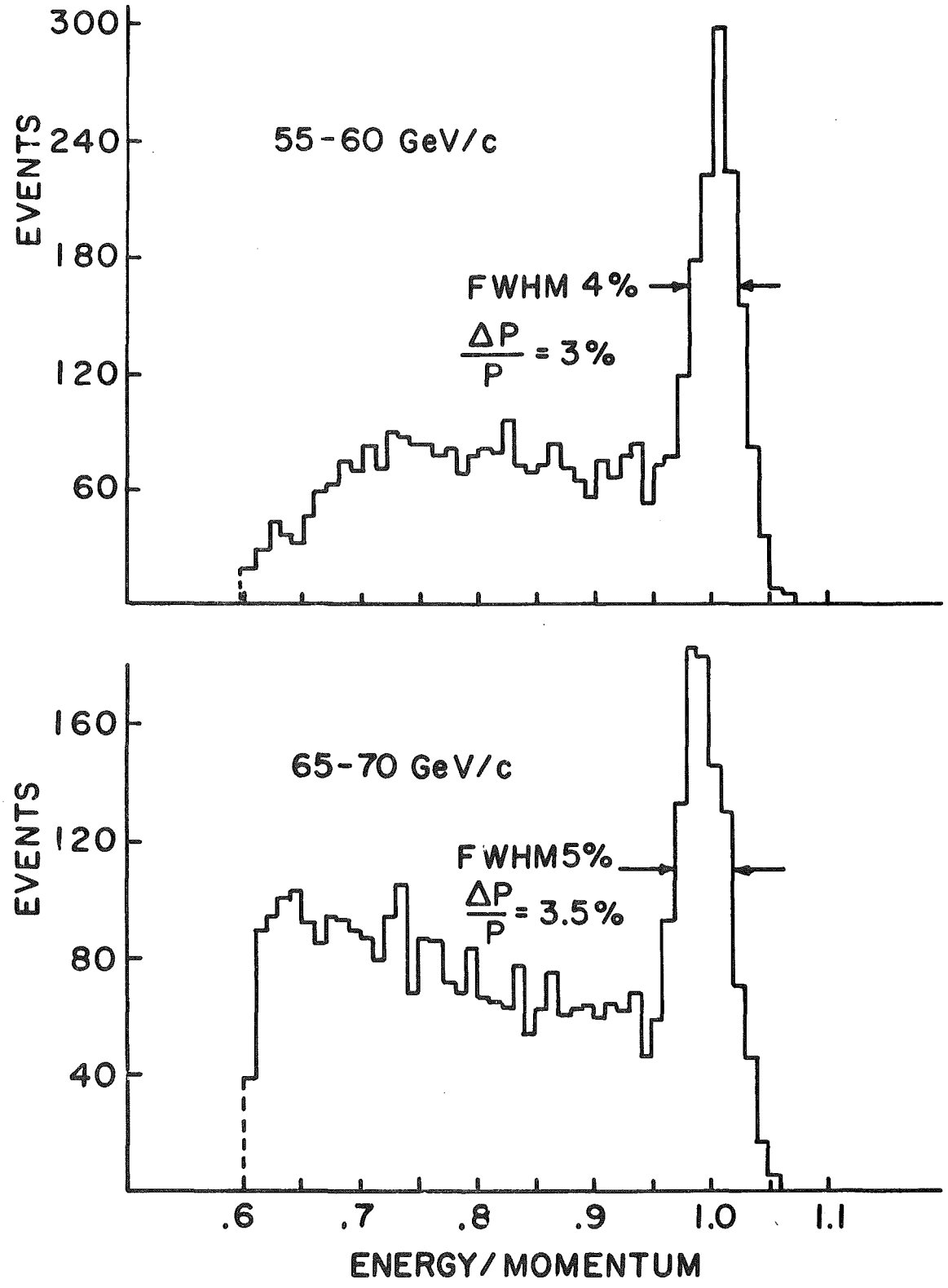
300
240
180
120
60
EVENTS
55-60 GeV/c
FWHM 4%
ΔP/P = 3%
160
120
80
40
EVENTS
65-70 GeV/c
FWHM5%
ΔP/P = 3.5%
.6
.7
.8
.9
1.0
1.1
ENERGY/MOMENTUM

FIG. 17

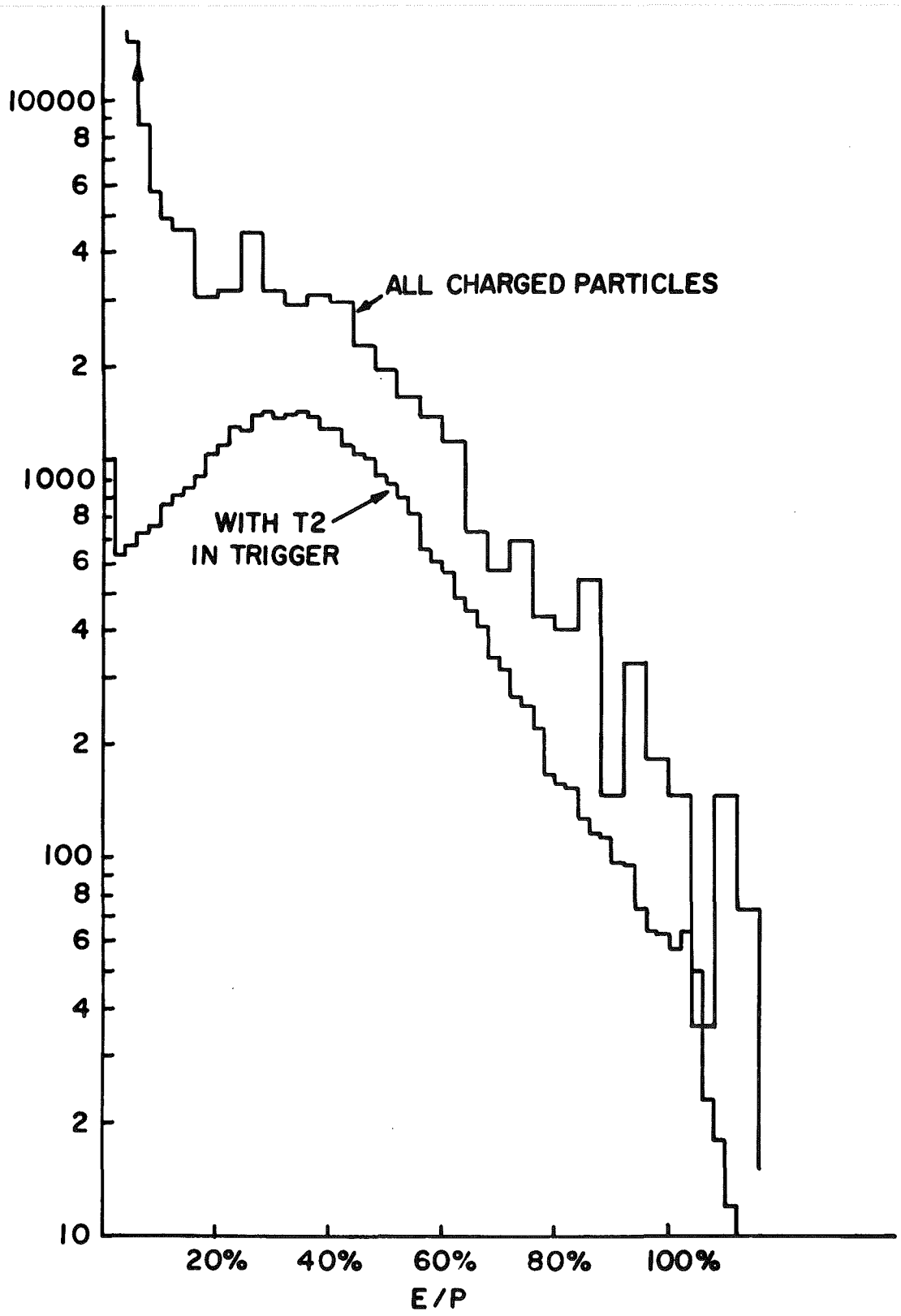
10000
8
6
4
2
1000
8
6
4
2
100
8
6
4
2
10
ALL CHARGED PARTICLES
WITH T2
IN TRIGGER
20%
40%
60%
80%
100%
E/P

FIG. 18

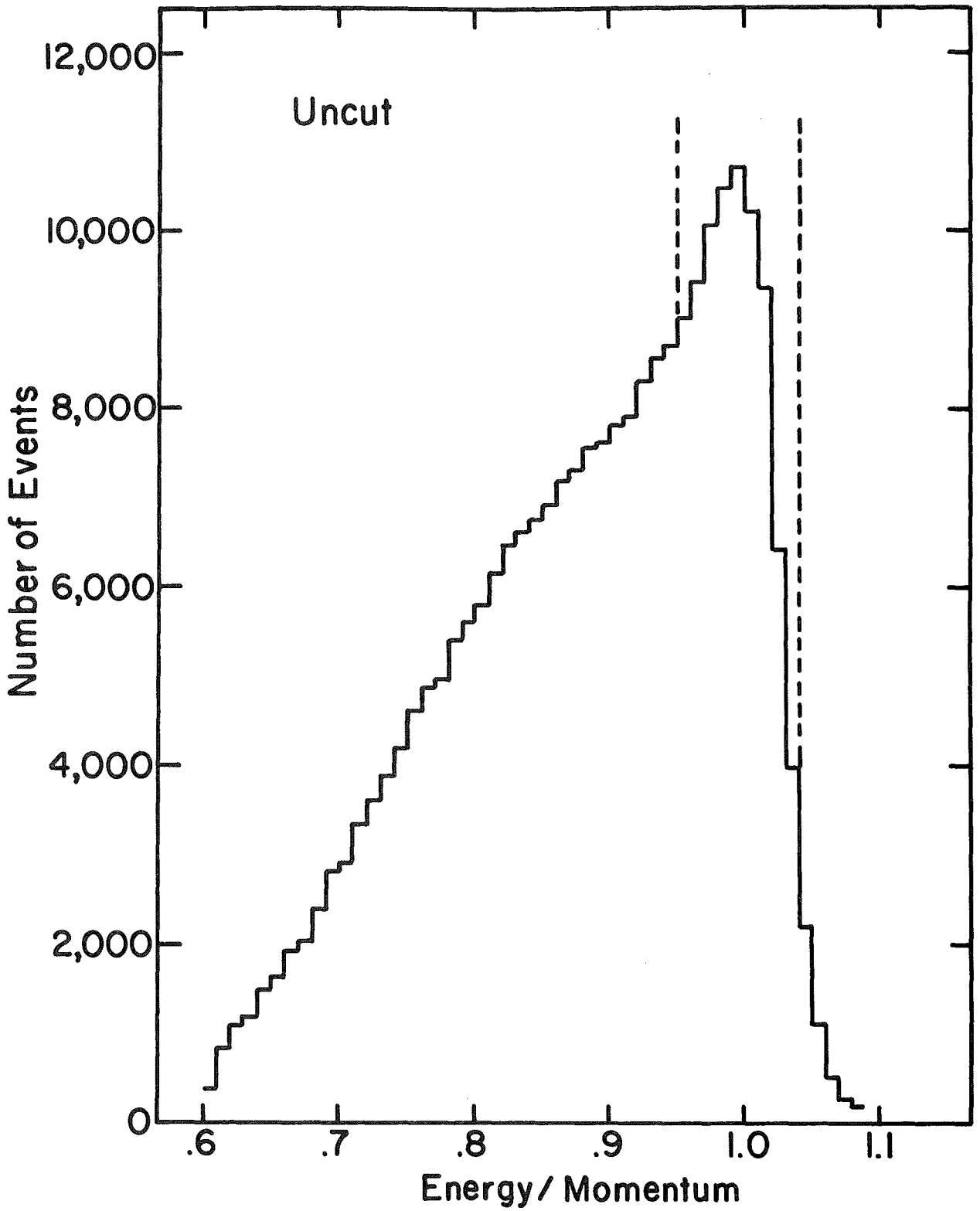
Uncut
12,000
10,000
8,000
6,000
4,000
2,000
0
Number of Events
.6
.7
.8
.9
1.0
1.1
Energy / Momentum

FIG. 19

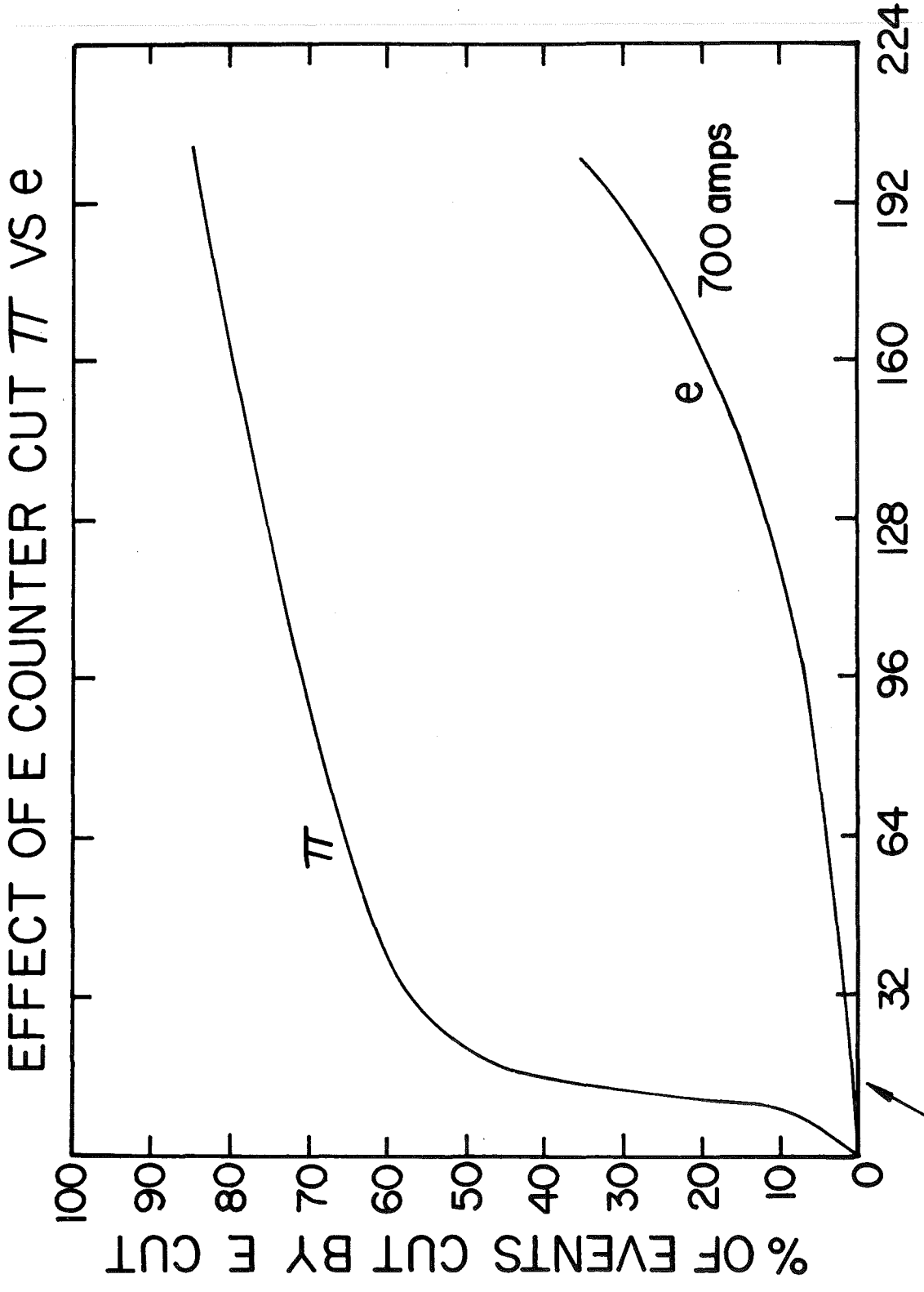
EFFECT OF E COUNTER CUT π VS e
% OF EVENTS CUT BY E CUT
100
90
80
70
60
50
40
30
20
10
0
π
e
700 amps
single ionizing peak
32
64
96
128
160
192
224
LEVEL OF E CUT

FIG. 20

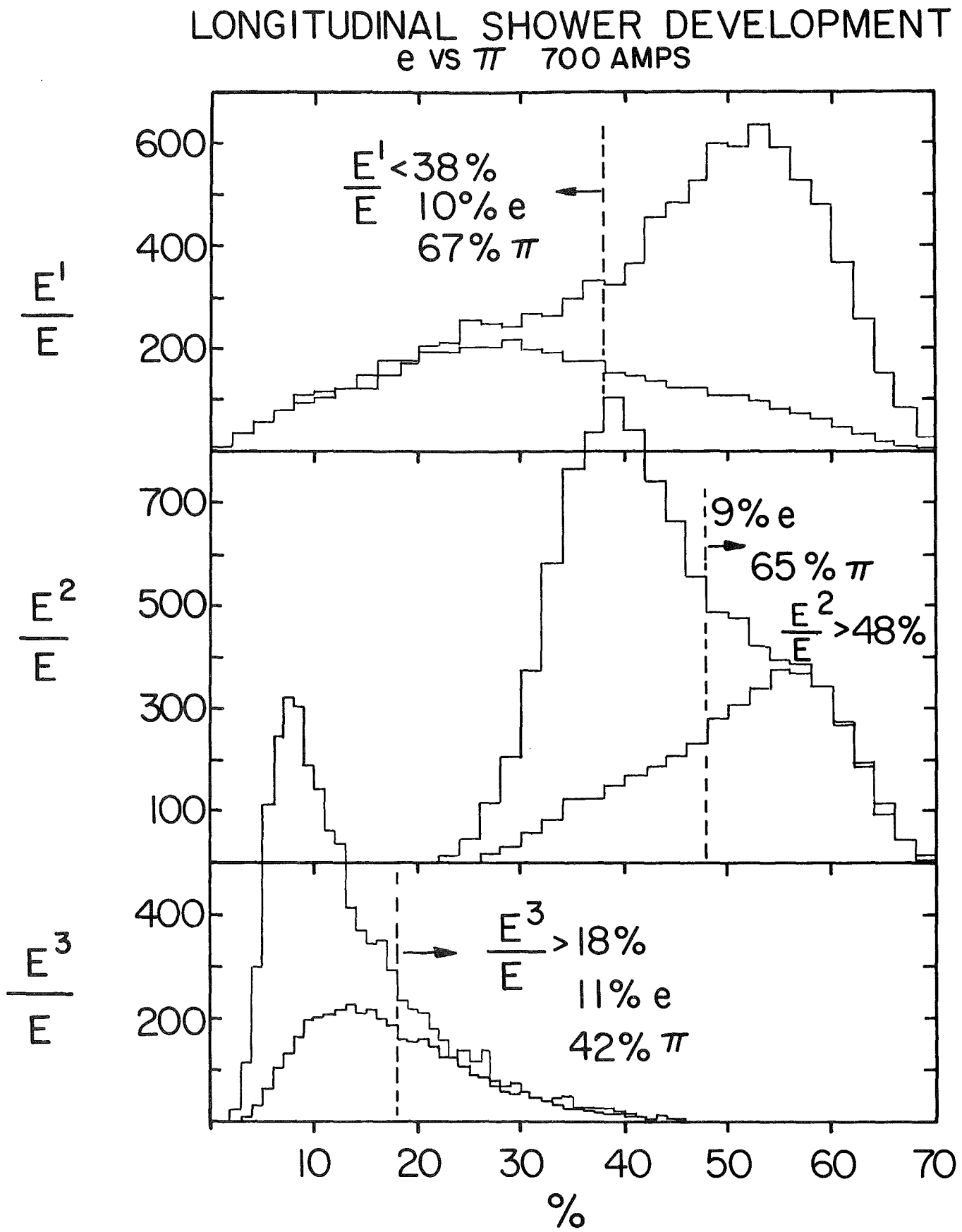
LONGITUDINAL SHOWER DEVELOPMENT
e vs π 700 AMPS
E'/E
E²/E
E³/E
E'/E < 38%
10% e
67% π
9% e
65% π
E²/E > 48%
E³/E > 18%
11% e
42% π
600
400
200
700
500
300
100
400
200
10
20
30
40
50
60
70
%

FIG. 21

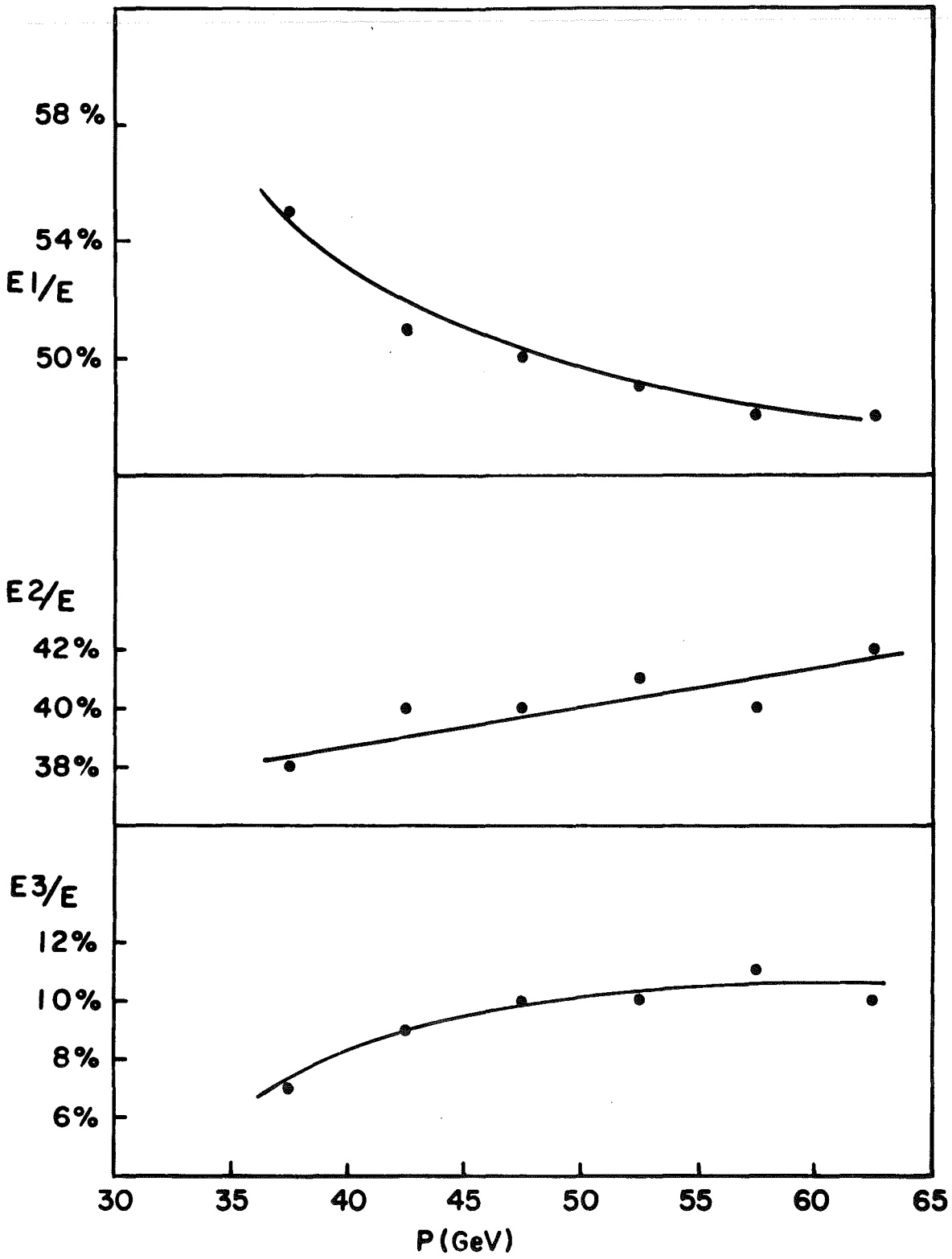

SHOWER DISTRIBUTION AS A FUNCTION OF MOMENTUM

FIG. 22

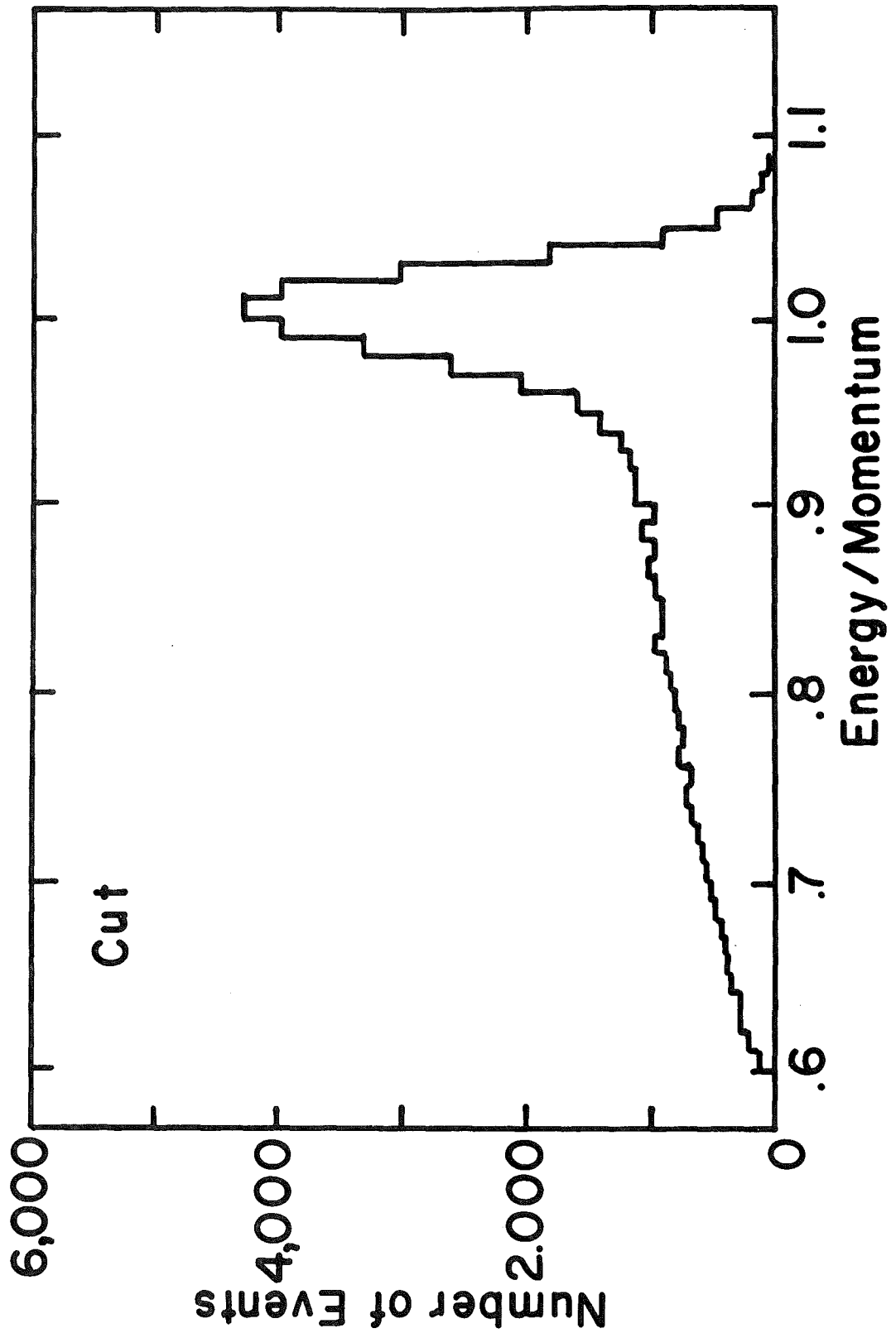
Number of Events
6,000
4,000
2,000
0
Cut
.6
.7
.8
.9
1.0
1.1
Energy/Momentum

FIG. 23

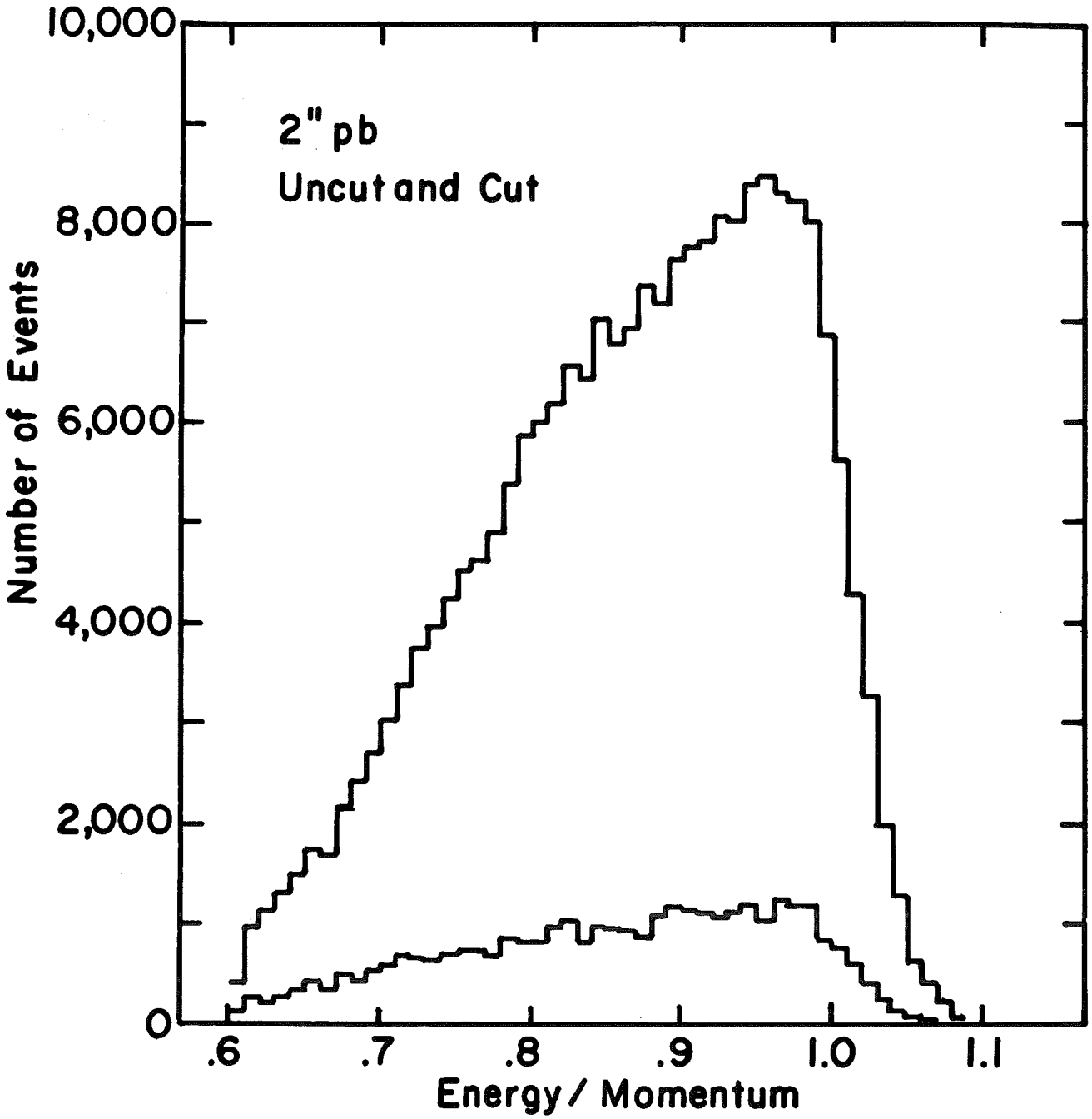
10,000
8,000
6,000
4,000
2,000
0
Number of Events
2" pb
Uncut and Cut
.6
.7
.8
.9
1.0
1.1
Energy / Momentum

FIG. 24

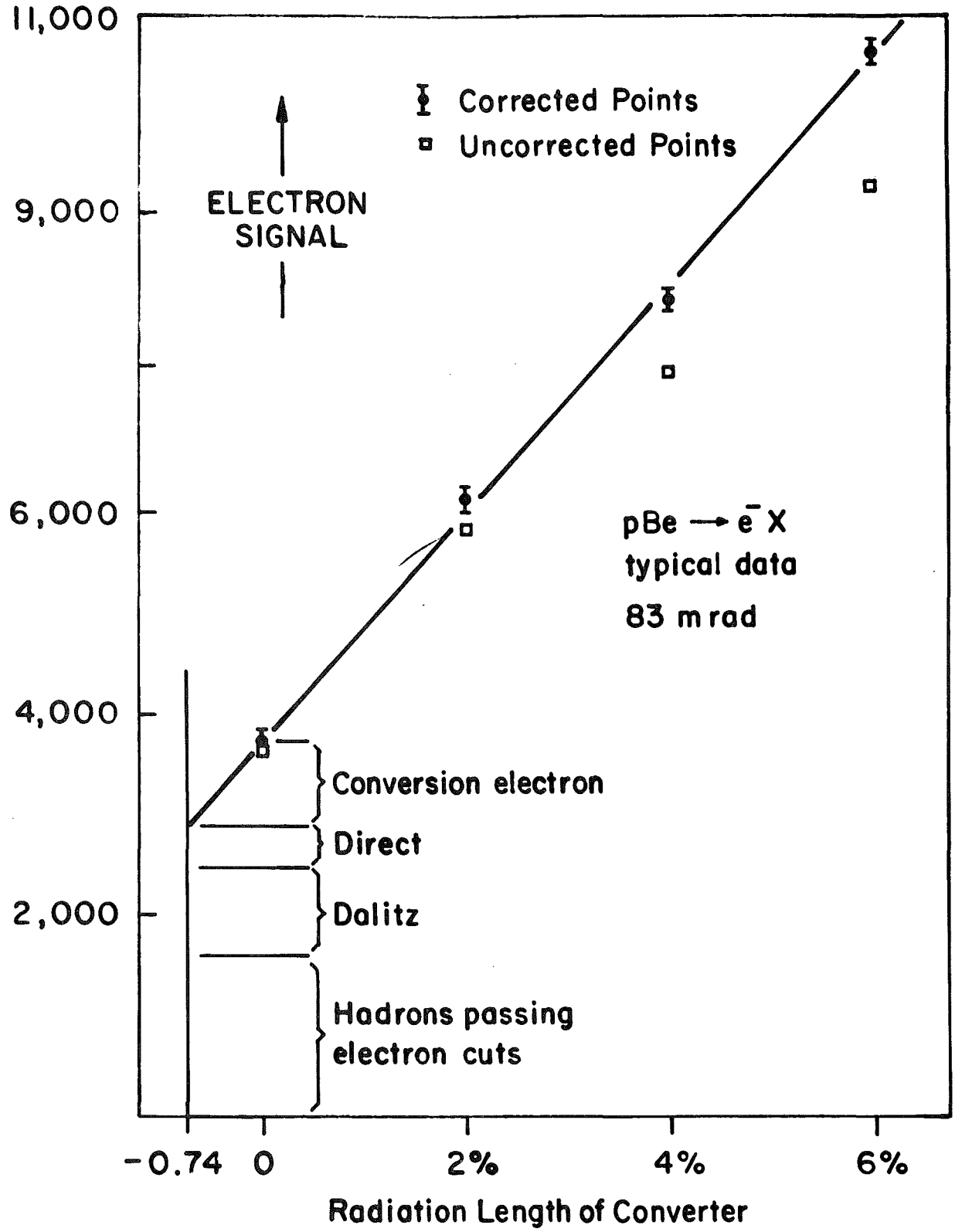
11,000
9,000
6,000
4,000
2,000
Corrected Points
Uncorrected Points
ELECTRON SIGNAL
pBe → e⁻X
typical data
83 m rad
Conversion electron
Direct
Dalitz
Hadrons passing electron cuts
-0.74
0
2%
4%
6%
Radiation Length of Converter

FIG. 25

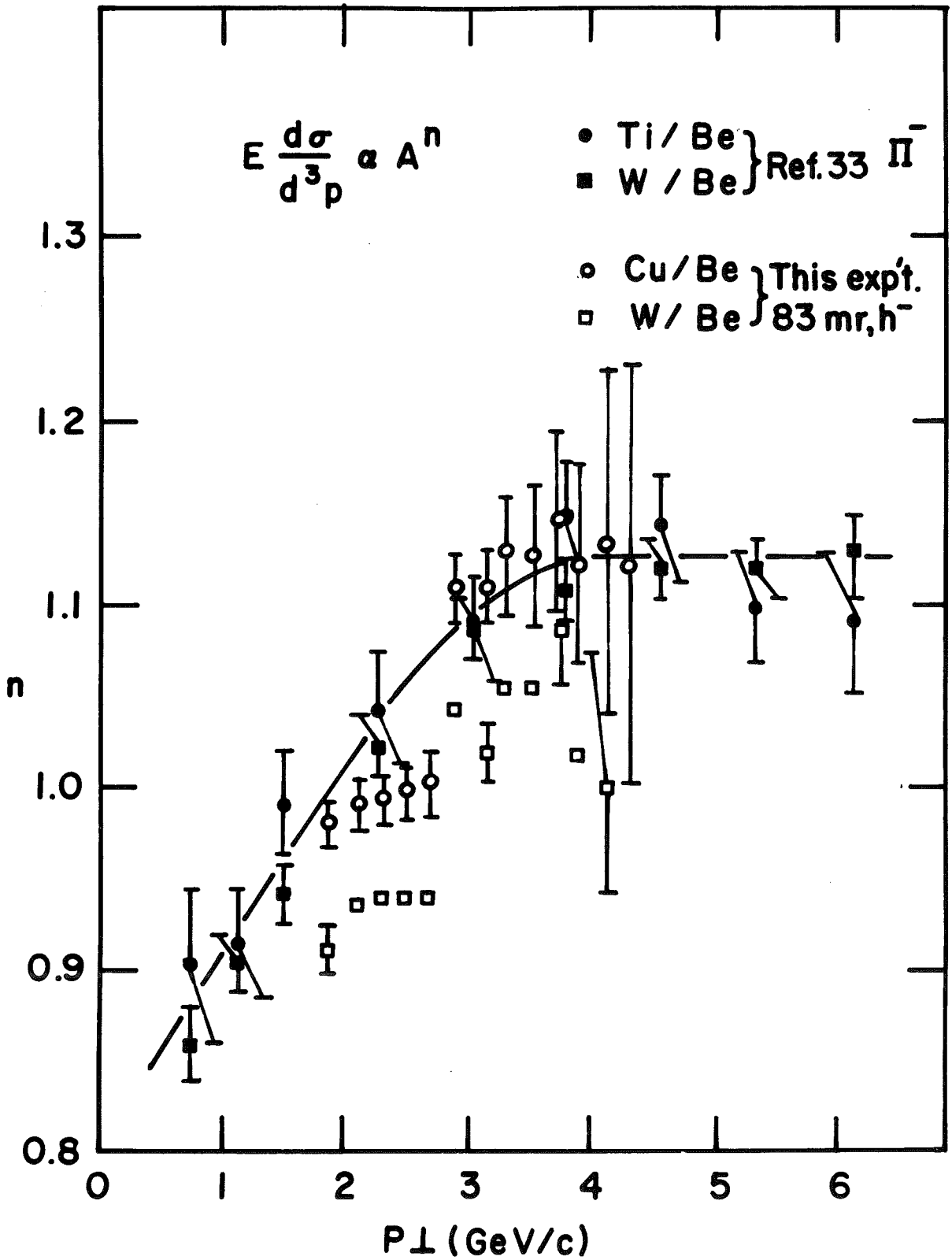
$E\frac{d\sigma}{d^3p} \propto A^n$
• Ti / Be
■ W / Be
Ref. 33 Π^-
o Cu / Be
□ W / Be
This expt.
83 mr, h^-
n
1.3
1.2
1.1
1.0
0.9
0.8
0
1
2
3
4
5
6
P⊥ (GeV/c)

FIG. 26

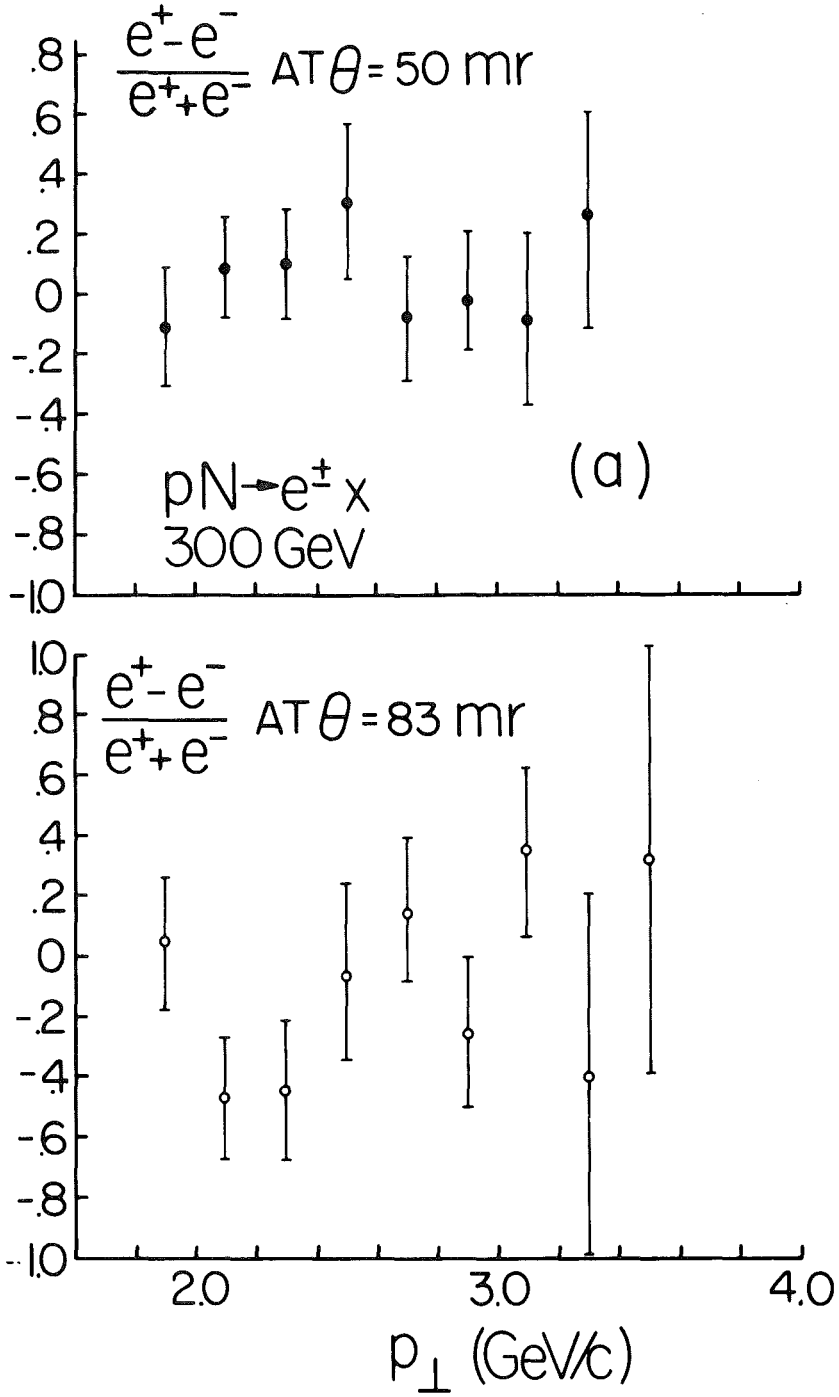
$\frac{e^+-e^-}{e^++e^-}$ AT θ = 50 mr
.8
.6
.4
.2
0
-.2
-.4
-.6
-.8
-1.0
pN→e± X
300 GeV
(a)
$\frac{e^+-e^-}{e^++e^-}$ AT θ = 83 mr
1.0
.8
.6
.4
.2
0
-.2
-.4
-.6
-.8
-1.0
2.0
3.0
4.0
$p_\perp$ (GeV/c)

FIG. 27

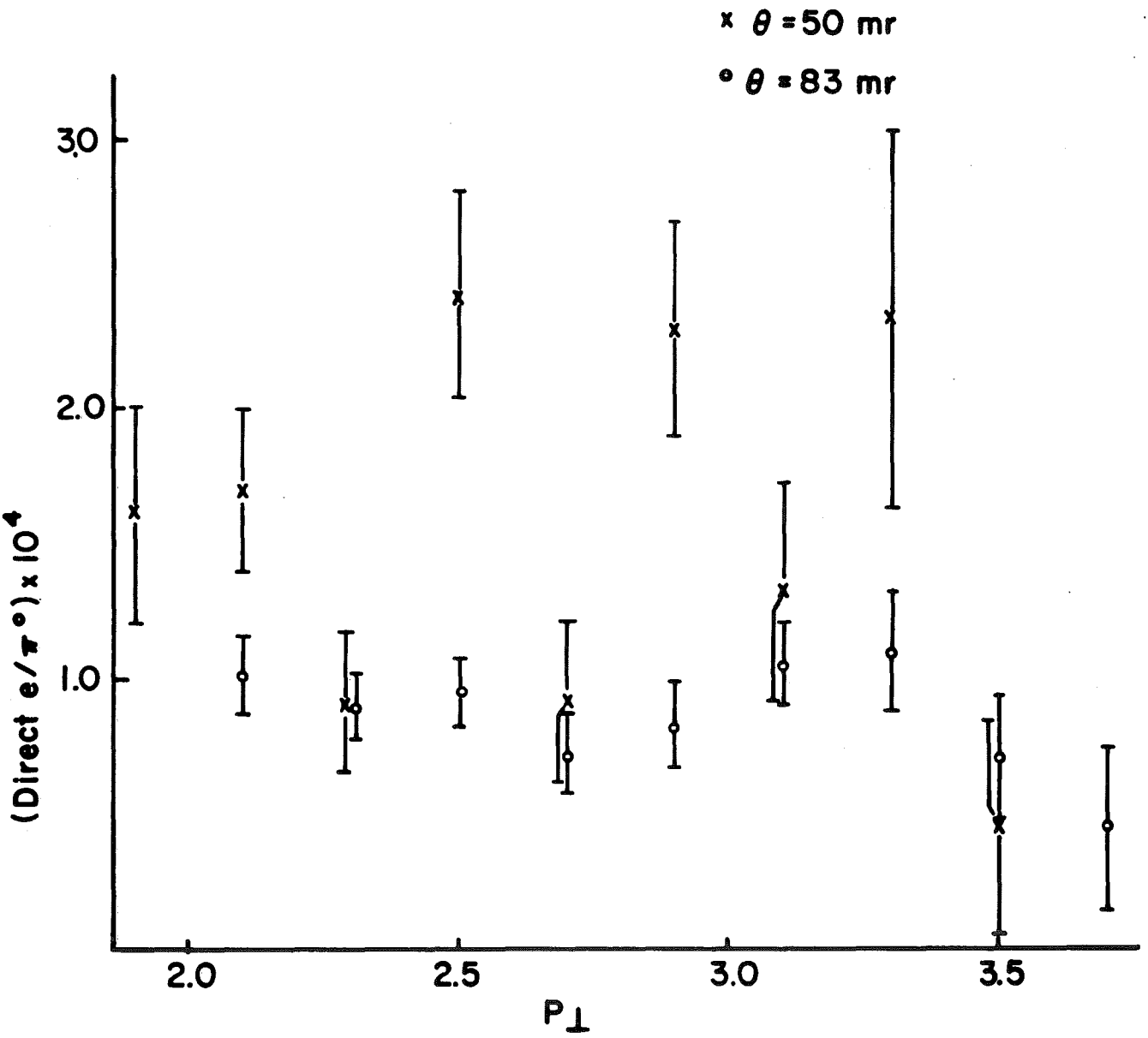

FIG. 28

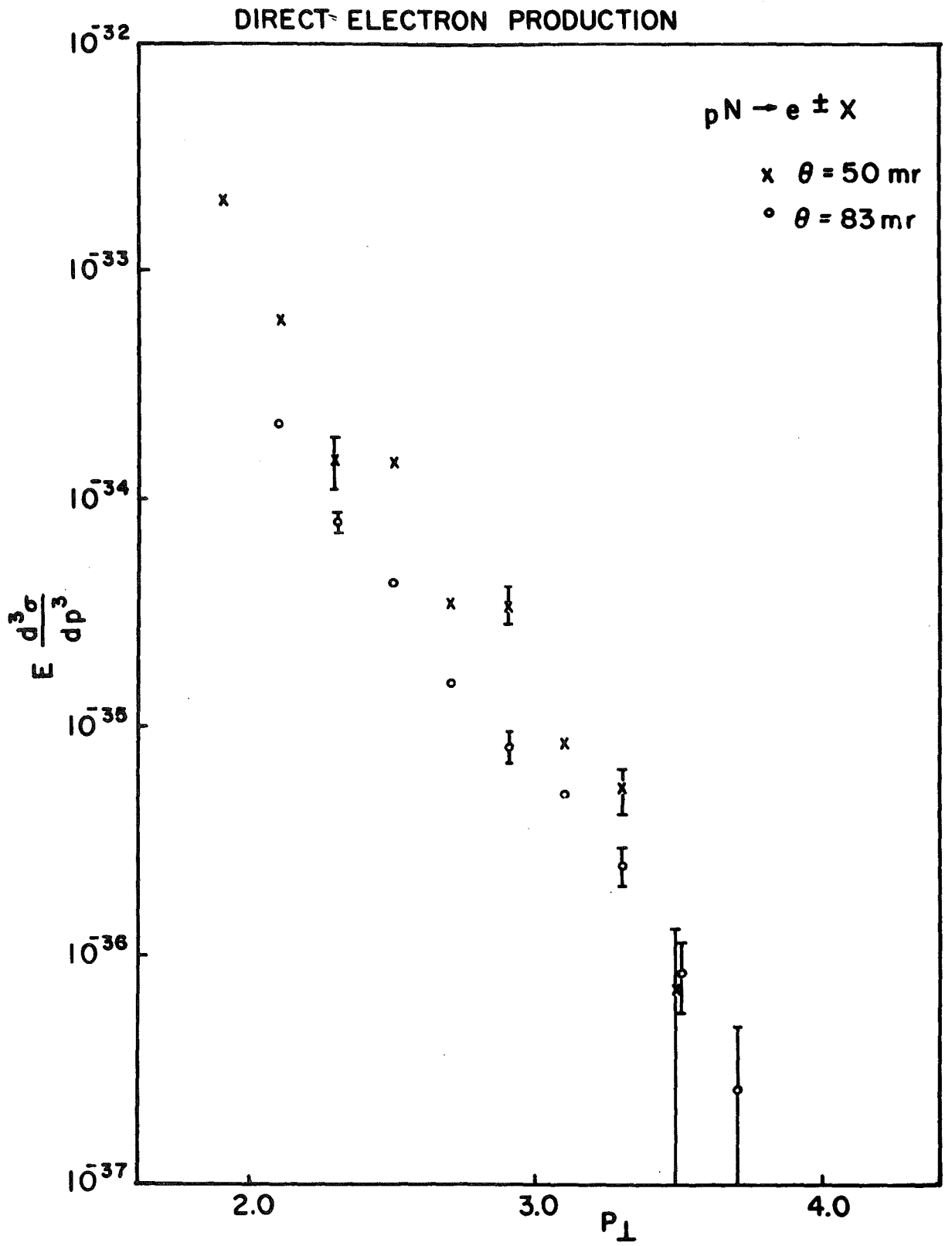
DIRECT ELECTRON PRODUCTION
pN → e ± X
x θ = 50 mr
° θ = 83 mr
10^{-32}
10^{-33}
10^{-34}
10^{-35}
10^{-36}
10^{-37}
$E\frac{d^3\sigma}{dp^3}$
2.0
3.0
4.0
$P_\perp$

FIG. 29

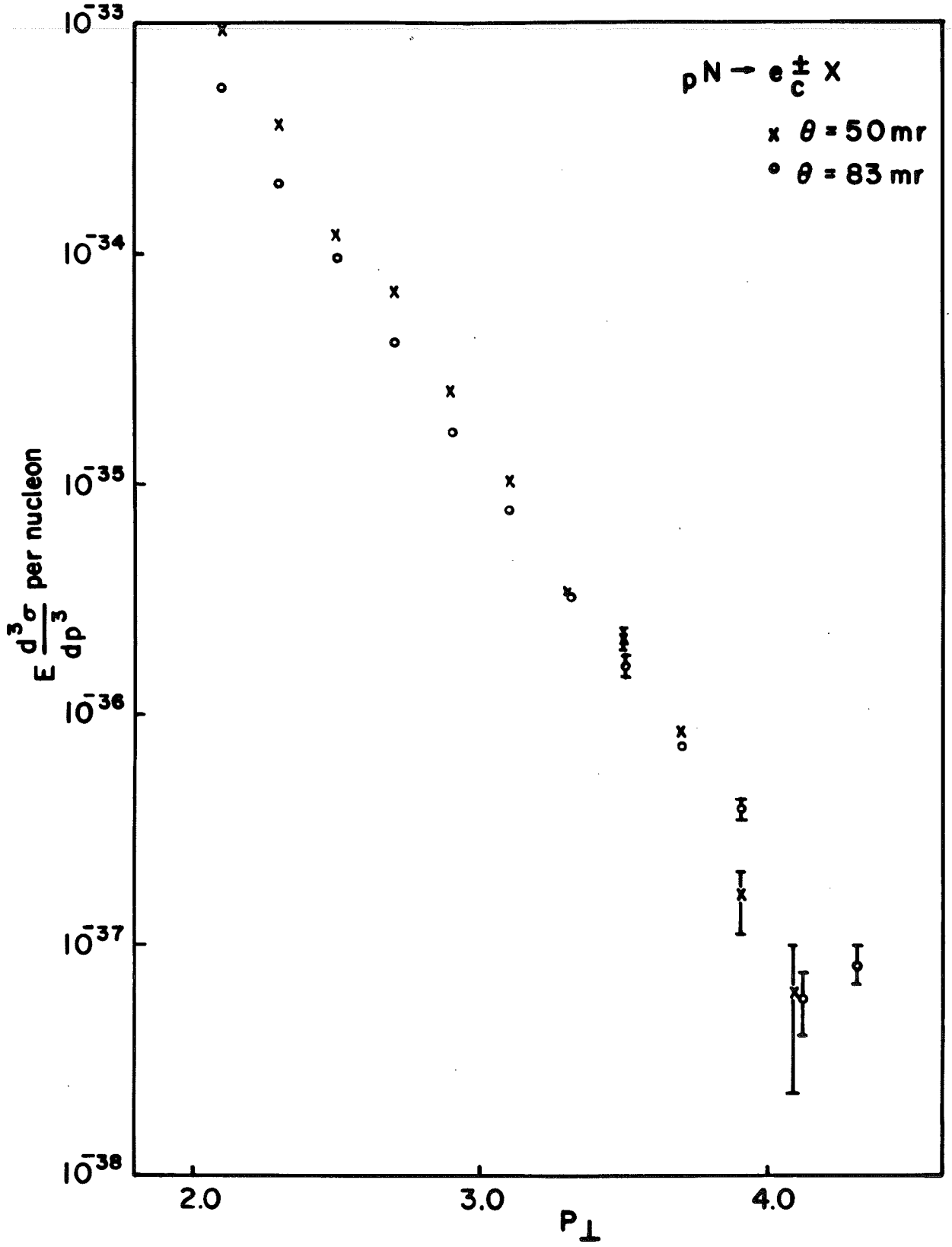
$pN \rightarrow e^{\pm}_{c} X$
x θ = 50 mr
o θ = 83 mr
$E\frac{d^3\sigma}{dp^3}$ per nucleon
10^{-33}
10^{-34}
10^{-35}
10^{-36}
10^{-37}
10^{-38}
2.0
3.0
4.0
$P_\perp$

FIG. 30

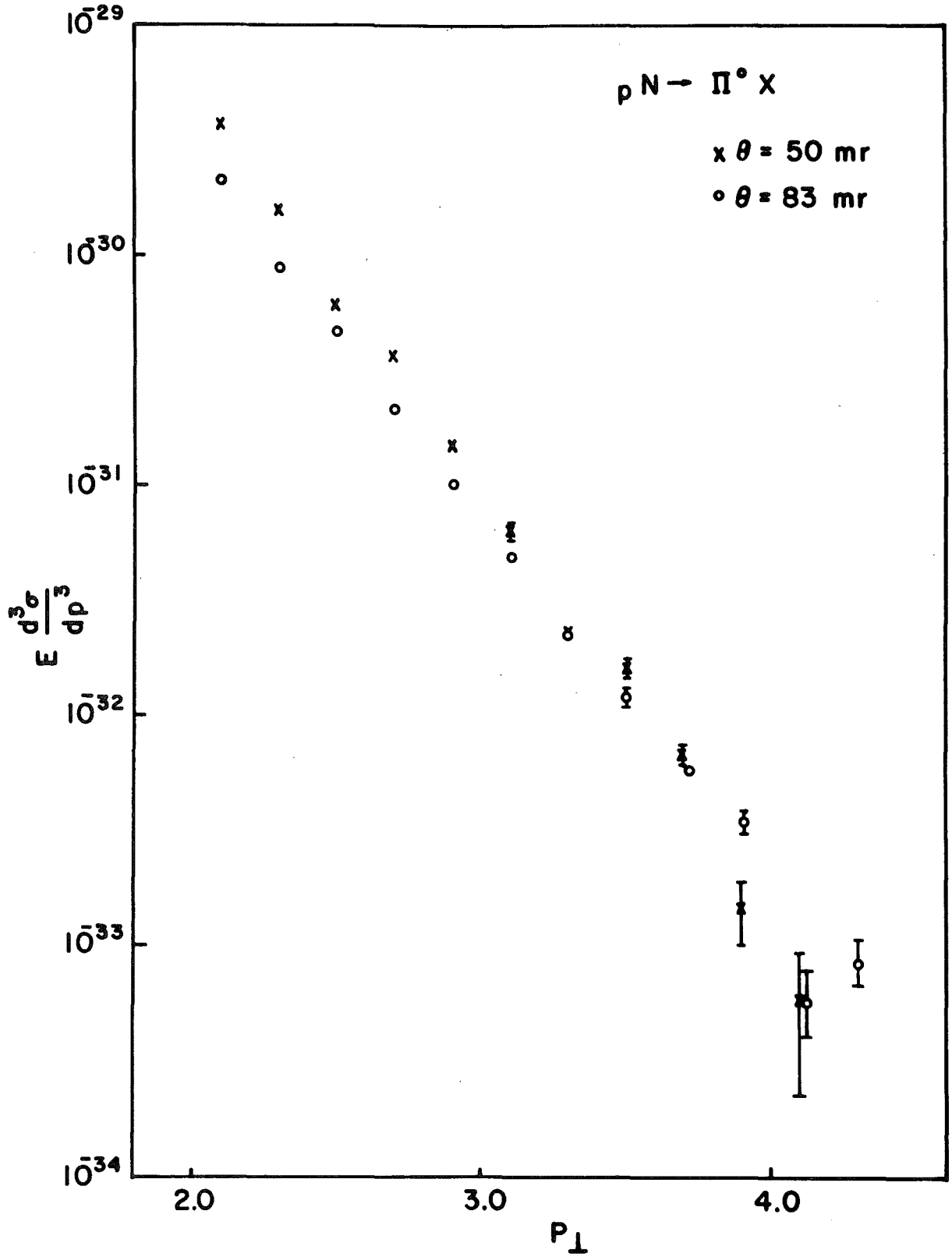
10^{-29}
10^{-30}
10^{-31}
10^{-32}
10^{-33}
10^{-34}
$E\frac{d^3\sigma}{dp^3}$
$p N \rightarrow \Pi^\circ X$
x θ = 50 mr
o θ = 83 mr
2.0
3.0
4.0
$P_\perp$

FIG. 31

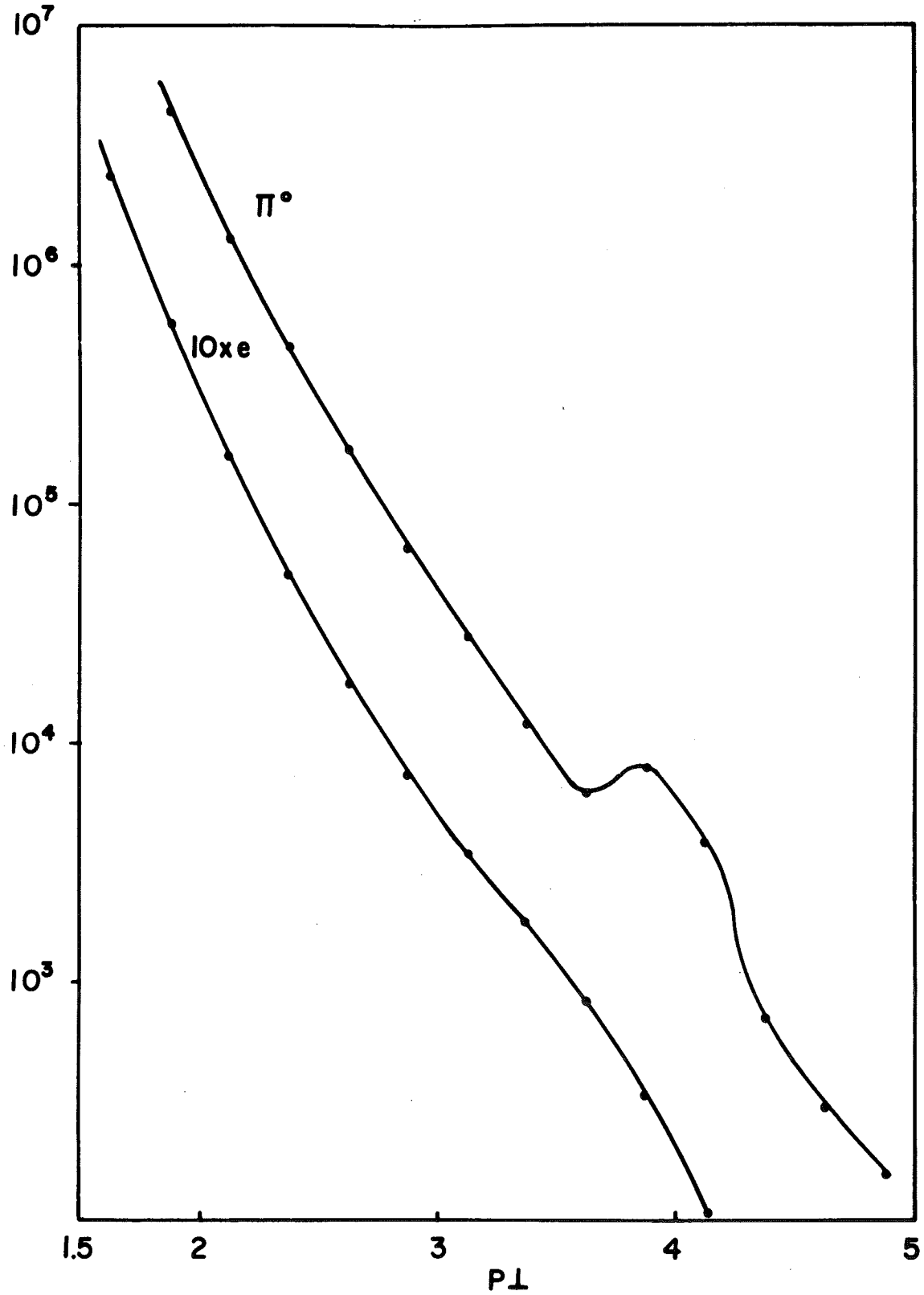

FIG. 32

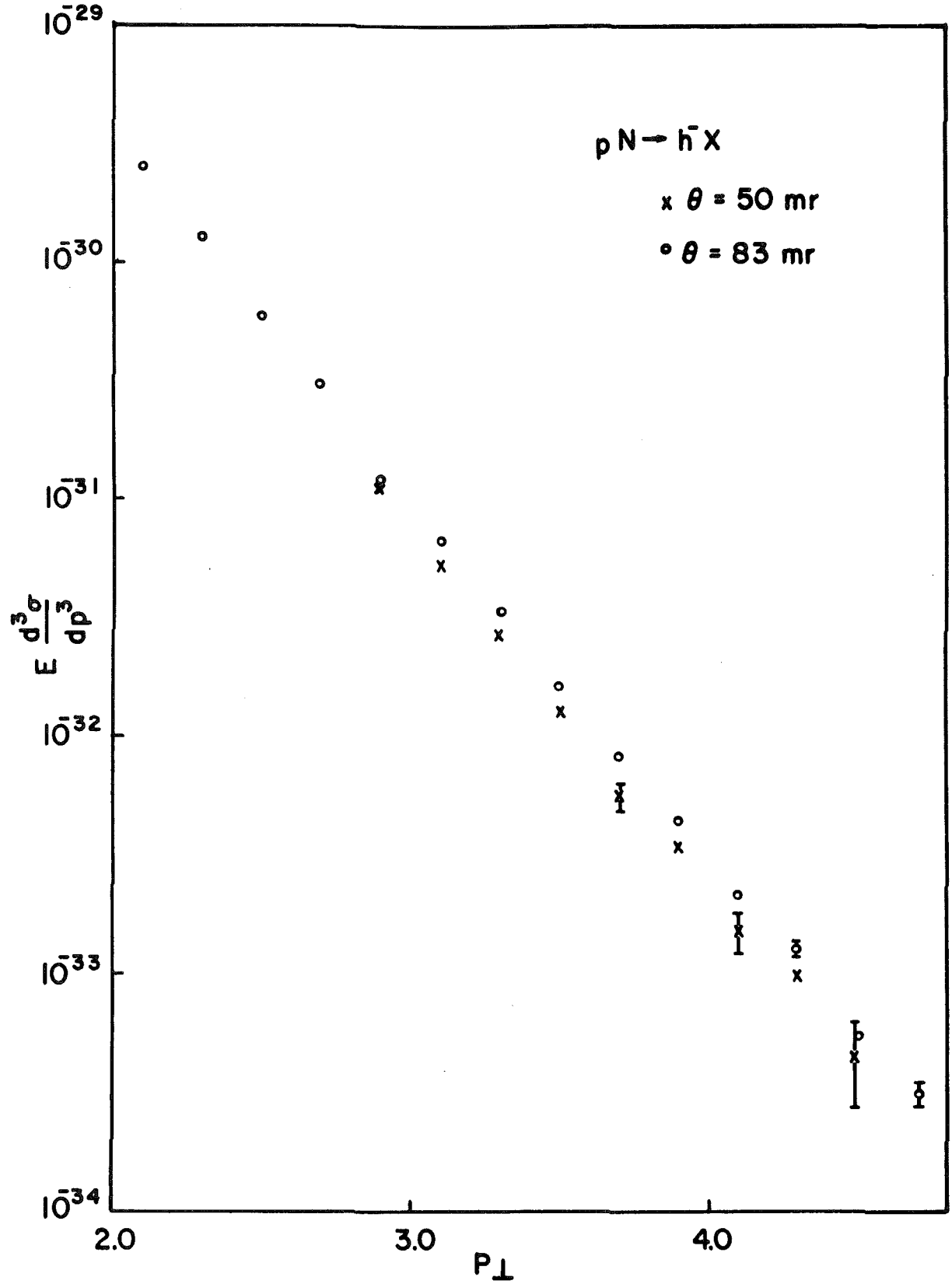
10^{-29}
10^{-30}
10^{-31}
10^{-32}
10^{-33}
10^{-34}
$E\frac{d^3\sigma}{dp^3}$
$p N \rightarrow h^- X$
x θ = 50 mr
o θ = 83 mr
2.0
3.0
4.0
$P_\perp$

FIG. 33

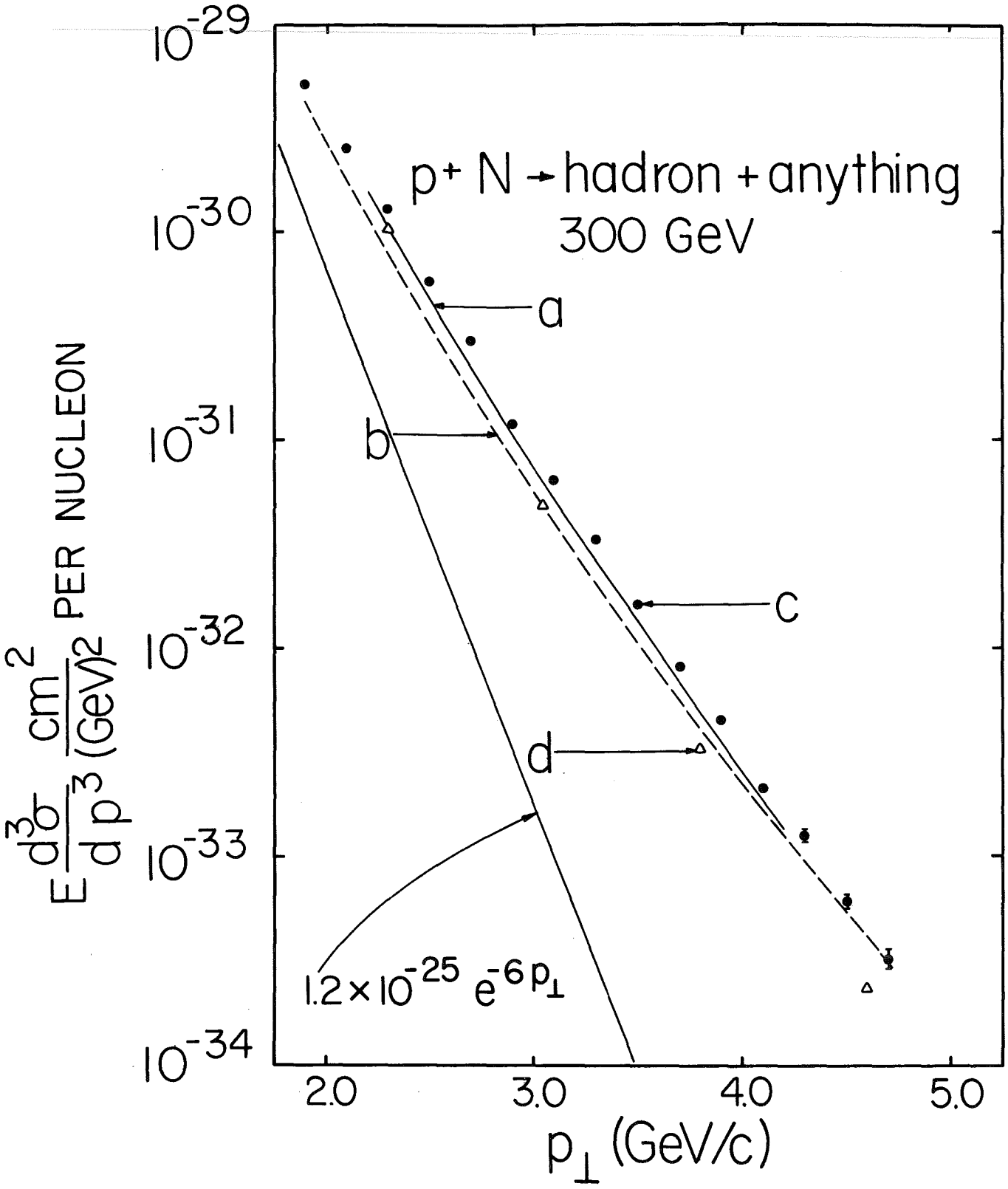
p+ N → hadron + anything
300 GeV
a
b
c
d
$1.2\times10^{-25}\ e^{-6p_\perp}$
$E\frac{d^3\sigma}{dp^3}\frac{cm^2}{(GeV)^2}$ PER NUCLEON
10^{-29}
10^{-30}
10^{-31}
10^{-32}
10^{-33}
10^{-34}
2.0
3.0
4.0
5.0
$p_\perp$ (GeV/c)

FIG. 34

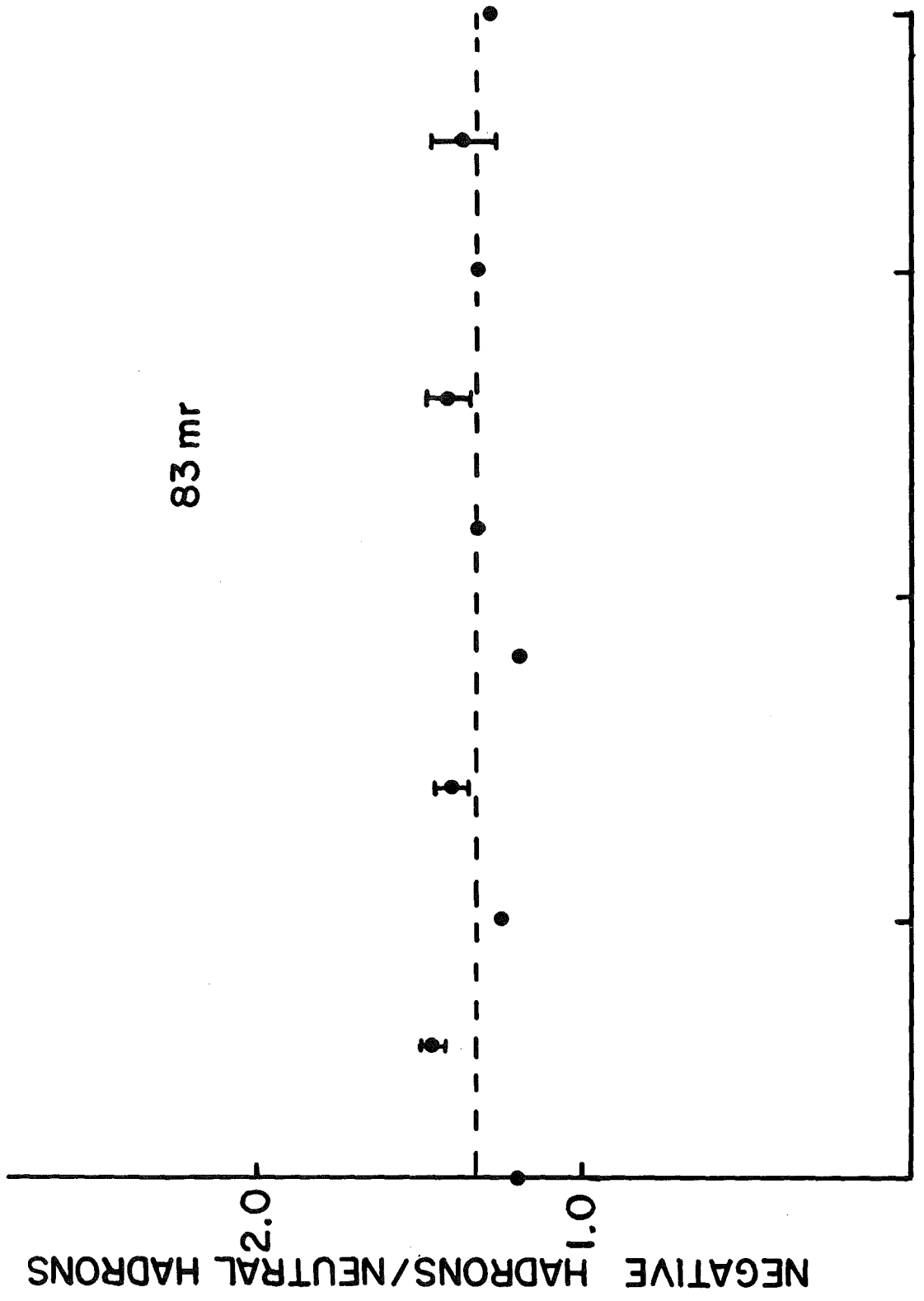

FIG. 35